Development of Triboelectric Devices for Self-powered Sensing And Energy Harvesting Applications

by

Chen Chen

A thesis
presented to the University of Waterloo
in fulfillment of the
thesis requirement for the degree of
Doctor of Philosophy
in
Systems Design Engineering

Waterloo, Ontario, Canada, 2019

Examining Committee Membership

The following served on the Examining Committee for this thesis. The decision of the Examining Committee is by majority vote.

External Examiner:	Robert B.A. Adamson Associate Professor, School of Biomedical Engineering Dalhousie University
Supervisor:	John T.W. Yeow Professor, Dept. of Systems Design Engineering University of Waterloo
Internal Member:	Jonathan Kofman Associate Professor, Dept. of Systems Design Engineering University of Waterloo
Internal Member:	Nima Maftoon Assistant Professor, Dept. of Systems Design Engineering University of Waterloo
Internal-external Member:	Peter Mark Levine Associate Professor, Dept. of Electrical and Computer Engineering University of Waterloo

Author's Declaration

This thesis consists of materials all of which I authored or co-authored: see Statement of Contributions included in the thesis. This is a true copy of the thesis, including any required final revisions, as accepted by my examiners.

I understand that my thesis may be made electronically available to the public.

Statement of Contributions

Below is a list of publications where I am the primary author. For this work, I am responsible for all of the design, fabrication, analysis and paper writing. Dr. Sun and Dr. Jian provided me the places and instruments for characterization. Additionally, Dr. Wen, Dr. Sun and Dr. Yeow assisted with the revision of the manuscripts. Other co-authors gave me insight and minor help in characterization, including experimental setups and data collection.

- **C. Chen, Z. Wen, A. Wei, X. Xie, N. Zhai, X. Wei, M. Peng, Y. Liu, X. Sun and J. T. Yeow, "Self-powered on-line ion concentration monitor in water transportation driven by triboelectric nanogenerator," Nano Energy, https://doi.org/10.1016/j.nanoen.2019.05.029. (This work is presented in chapter 3)**

- **C. Chen, Z. Wen, X. Jian, P. Li, X. Sun and J. T. Yeow, "A Novel Triboelectric Energy Harvester for Wireless Energy Transfer and Communication via Ultrasonic Link," ready to submit. (This work is presented in chapter 4 and 5)**

Abstract

Due to the bulky size and limited lifespan of batteries, remote charging and energy harvesting from the environment are becoming two trends to power miniaturized electronics. Triboelectric nanogenerator (TENG) is an emerging technology to convert mechanical energy to electricitical energy by the coupling of triboelectrification and electrostatic induction. It has been widely applied to self-powered sensing and energy generation by virtue of the simpler device configuration and broader material choices compared to conventional energy conversion technologies, such as electromagnetic and piezoelectric energy harvesters.

In this thesis, it is the first time to presented a self-powered on-line ion concentration monitoring system based on the impedance matching effect of TENG. Other than handcrafted TENGs, the rotary disc-shaped TENG (RD-TENG) was fabricated by the industrial printed circuit board (PCB) technology, which could realize sophisticated design and low-cost fabrication. Flowing water, as the energy source, in the pipeline was utilized to drive the RD-TENG and generate an open-circuit voltage (V_{OC}) of ~210 V_{P-P}. The impedance matching effect of TENG as the sensing mechanism was studied thoroughly. Based on the impedance matching effect, an alarm circuit was designed for the demonstration and the alarm LED can be successfully lit up by the change of NaCl concentration with only 1×10^{-5} mol/L, which showed a high sensitivity.

Compared to environmental monitoring, healthcare monitoring requires further miniaturized size and better compatibility with electronics. To satisfy the demands, a novel micro triboelectric energy harvester (μTEH) was developed. Based on the μTEH, a propotyped acoustic energy transfer system was built via an ultrasound link. For the very first time, TENG was fabricated by Micro-electro-mechanical systems (MEMS) technologies in batch process, giving better integrated circuit (IC) integration. More importantly, it is also the first time that the size of TENG is brought into microscale. We demonstrated a prototyped acoustic energy transfer system for implanted devices that could generate 50 nW power on load resistor under 1 MHz, 132 mW/cm^2 incident acoustic power. The μTEH also achieved a signal-to-ratio (SNR) of 20.54 dB and exhibited promising potential for wireless communication by modulating the incident ultrasound. Finally, detailed optimization methods were proposed to improve the output power of the μTEHs in the future.

Acknowlegements

Among too many people, I would firstly express my most thanks to my supervisor, Prof. John T.W. Yeow, for offering me the opportunity to work in this amazing lab since I was an undergraduate student. He gave me so much support and I could always get response whenever I encountered problems. When I was frustrated because things did not go as expected, his brilliant talent and passination in research can always inspire me, lead me out and rebuild my confidence. I would also thank Prof. Xuhui Sun, my supervisor during the two years in China. He is one of the kindest and the most patient person I have ever met. Thanks to my committee members – Prof. Jonathan Kofman, Prof. Nima Maftoon and Prof. Peter Levine. I also want to thank Prof. Zhen Wen for showing me a totally new area. Special thanks to Prof. Xiaohua Jian for kindly providing me the testing equipment in his lab.

Working with my outstanding colleagues is the the most valuable experience during my PhD. I thank every lab member: Champika, Zhenhao, Limin, Lawrence, Fred, Albert, Yibei, Yunhan, Siyuan, Nash, Joe, Yaning and Mingyu (sincere apologies to those I might have missed). Many thanks for their encouragement and help. I would also thank all of the people I met in Suzhou. I will treasure the memorable experience all my life.

Last but most importantly, I would thank my parents for their unwavering support. I cannot complete my PhD study without them.

Table of Contents

List of Figures

List of Tables

Chapter 1

Introduction

The rapid advances in the Internet of Things (IoT) are revealing the new requirements of the power source with the characteristics of smaller size, better sustainability and environment-friendliness. Numerous individual nodes are deployed for monitoring and data communication in the IoT network. However, the arrangement of the electrical wires and the maintenance of batteries are huge consumption of time, labor and money. The disposal of batteries is also a big issue that may be harmful to environment and hazardous to human health. To overcome these issues, new strategies of energy generation are in desperate need. Energy harvesters can convert energies of another form (e.g., solar energy, biological energy, thermal energy and mechanical energy) to electrical energy through various mechanisms.

Different from solar energy and thermal energy, mechanical energy is not limited by time, weather or location. It is one of the most abundant energy in our daily life, including wind, flowing water, vibrations and even motions of human body. A large amount of ”wasted” mechanical energy could be useful if we can capture it.

1.1 Current technologies of mechanical energy harvesting

Several different technologies have been applied to harvest mechanical energy and extend the life-span of devices, including electromagnetic induction, electrostatic induction and piezoelectric effect [1, 2].

- Electromagnetic induction

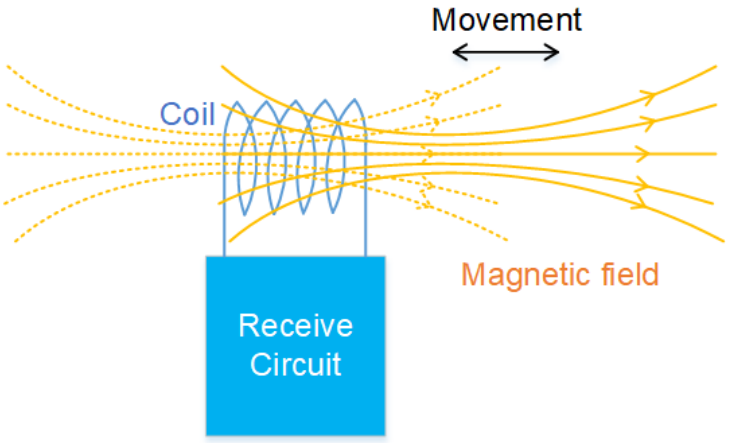

Figure 1.1: Graphic illustration of electromagnetic energy harvesting.

Electromagnetic induction was discovered by Michael Faraday in the 1800s. The process of the energy conversion via electromagnetic induction is the generation of alternating current in a metal coil, which is placed in a magnetic field (shown in Fig. 1.1). The electricity is generated by either the relative movement between the coil and the magnetic field or the variation of the magnetic field. The generated current intensity is highly dependent on the strength of the magnetic field, the diameter/turns of the coil and the velocity of the relative movement [3]. Although electromagnetic energy harvesting has been widely explored for decades with a decent efficiency to date [4–6], the complex system construction limits its miniaturization. Additionally, theoretical study has already proved that the efficiency of electromagnetic energy harvester has an obviously drop in the sub-millimeter scale [7].

- Electrostatic induction

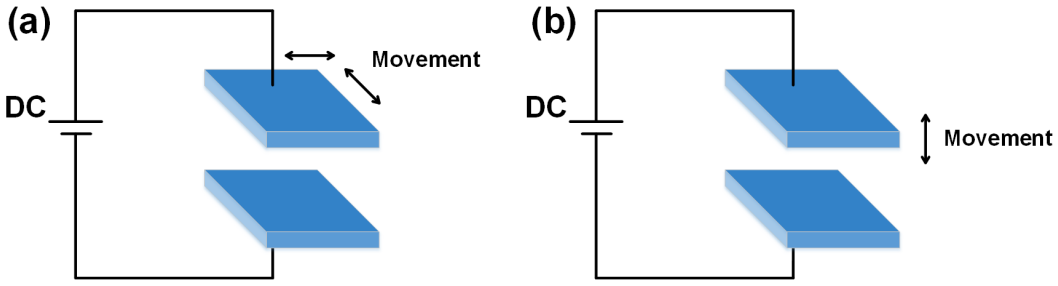

Figure 1.2: Graphic illustration of (a) in-plane and (b) out-of-plane electrostatic energy harvesting.

In principle, electrostatic induction is based on a capacitor consisting of two parallel plates. Under DC bias, an electrostatic field is initially built between the two plates. The relative movement between plates, induced by mechanical force, generates electrical energy (shown in Fig. 1.2). Typically, electrostatic energy harvester can be classified into two types, depending on the in-plane movement or the out-of-plane movement between plates [8–12]. To achieve high efficiency, a minuscule separation between two plates is desired. It results in a limited movement of plate, which further limits the output power [13]. It is also noteworthy that the applied DC bias can be as high as hundreds of Volts, which causes the safety concern.

- Piezoelectric effect

The piezoelectric effect is a well-known working mechanism where mechanical energy is converted to electrical energy through piezoelectric materials. Electricity is generated when stress is applied to the piezoelectric material. Fig. 1.3 illustrates the piezoelectric conversion mechanism.

The output power of the piezoelectric energy harvester is highly dependent on the inherent properties and the structure of piezoelectric materials. Currently, piezoelectric energy harvester can be divided into three categories. One is piezoelectric nanogenerator (PENG), where

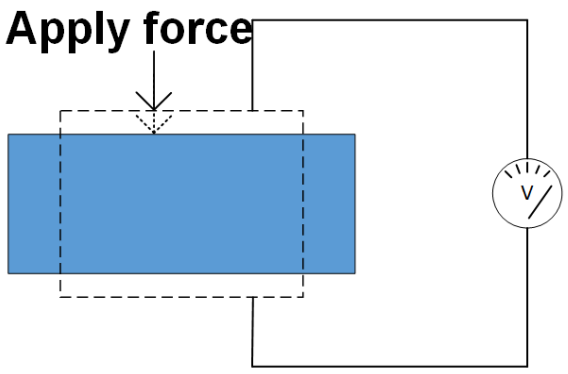

Figure 1.3: Graphic illustration of the piezoelectric effect.

piezoelectric materials are fabricated in nanostructures (nanorods, nanowires, nanobelts and *etc*.). Zinc oxide (ZnO) is the most commonly-used piezoelectric material for PENG because nanostructured ZnO can be easily fabricated by multiple methods [14–16]. Recent researches reported that nanostructured ZnO can be fabricated on the flexible substrate, such as polydimethylsiloxane (PDMS) and polyethylene terephthalate (PET). These flexible PENGs show the great potential for powering wearable and implanted devices. The second type of piezoelectric energy harvester is based on bulk PZT transducer. PZT is a piezoelectric ceramic material with the chemical formula of $Pb(Zr_xTi_{1-x})O_3$ ($0 \leq x \leq 1$) and has a high piezoelectric coefficient. Even though this kind of piezoelectric energy harvesters can generate the highest output power, the issues of the bulky size and poor integration with IC limit their applications. Bulk PZT transducers are often adopted for the acoustic energy transfer (AET) application to obtain maximum efficiency [17, 18]. In AET applications, an external acoustic energy source is provided so that the transmitted energy is much more stable (less affected by environmental variations) and the transmitted signal can even be modulated from the transmit end [19]. However, the toxicity of PZT also limits its applications. The third type of piezoelectric energy harvester is based on the piezoelectric thin film. Compared to the bulk counterpart, this thin-film-based piezoelectric energy harvester is more miniaturized, more flexible with device configuration

and more compatible with IC integration, resulting in wider applications [20–22]. However, the fabrication of high-quality piezoelectric thin film is currently a challenging work [23, 24]. An easy, low-cost and MEMS-compatible fabrication method is highly required to advance this technology.

Table 1.1: Challenges of current technologies for mechanical energy harvesting.

Technology	Current challenges
Electromagnetic induction	Complex system and low efficiency in small scale
Electrostatic induction	DC required and low output
Piezoelectric effect (bulk PZT)	Large device size, poor integration and toxicity
Piezoelectric effect (PZT thin film)	Complicated fabrication process

To date, challenges of current technologies (summarized in Table 1.1) still exist and new technology is needed to overcome them. Triboelectric nanogenerator (TENG) is an emerging and promising technology which was invented in 2012 [25]. Compared to other commonly-used energy harvesting technologies, TENG has the advantages of higher output, simpler device configuration/fabrication and broader material choices [26, 27]. It shows great potential to overcome the abovementioned challenges. Since invention, it has been widely applied for self-powered sensing and energy harvesting and has been attracting more attention.

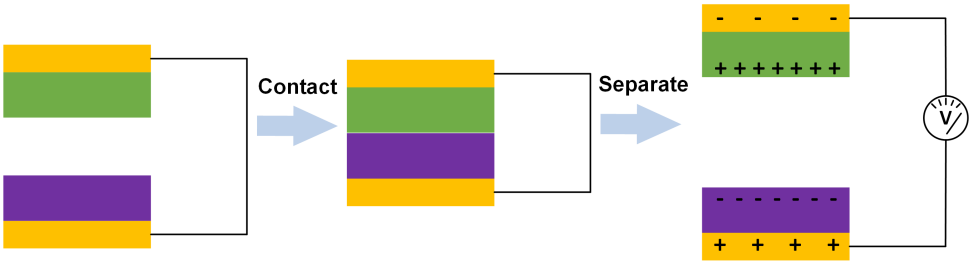

Figure 1.4: Graphic illustration of triboelectric effect.

The mechanism of the triboelectric energy harvester is actually the conjunction of the triboelectrification and electrostatic induction. Although the phenomenon of contact triboelec-

trification was discovered thousands of years ago and can be observed almost every day, the exact physical essence behind this phenomenon is still ambiguous [28, 29]. It is well accepted that the charges (mostly free electrons) can transfer between two materials driven by the surface potential difference when two materials are brought into contact. If the two contacting materials are insulators, the transferred charges will be trapped on the surfaces and an electric field will be built between two materials. Similar to electrostatic energy harvesting, electricity is generated by the relative movement between two materials, as shown in Fig. 1.4. In 2012, Wang group proposed this new type of energy harvester for the first time [25]. Compared to other energy harvesters, triboelectric nanogenerator has the advantages of high output, low cost, simple configuration and abundant material choices. It is attracting increasing attention in the fields of the power generation and self-powered sensing.

1.2 Objectives

Water quality is often regulated in many industries and the monitoring of water quality is a necessary process for the industrial production. An on-line and real-time monitoring system will effectively improve the reliability of the product in the long term. Furthermore, it will be a huge economization of energy if the monitoring systems can sustainably work without external power supply. However, the study of real-time water quality monitoring is still a blank area up to now. Hence, the first motivation of the thesis is to explore a novel strategy, based on TENG, to scavenge the mechanical energy of flowing water and power the sensor so that a self-powered sensing system can be constructed to monitor the water quality in real time.

Other than the environmental monitoring, healthcare monitoring is also seeking an efficient energy harvesting technology. Benefiting from the micro-/nano-electromechanical sys-

tem (MEMS) technologies, a lot of healthcare monitoring devices, such as implanted devices, are following the trends of miniaturization, low power consumption and easy integration with integrated circuit (IC). To power these devices, the power sources should also follow the above-mentioned trends. Therefore, another motivation of the thesis is to combine the TENG and MEMS technologies and to promote the miniaturization and integration of the TENG. As a result, the TENG can be more compatible with micro-/nano-electronic systems.

1.3 Thesis organization

This thesis is organized in six chapters. In Chapter 2 introduces the fundamental physics, basic working modes and major applications of triboelectric nanogenerators.

Chapter 3 presents a self-powered on-line ion concentration monitoring system based on TENG. It is an excellent example to harvest environmental energy by TENG. In this chapter, a disc-shaped TENG (RD-TENG) was designed and fabricated to harvest the mechanical energy from flowing water and convert to electrical energy. In the prototyped system, both the sensor and TENG were fabricated based on PCB technology. Lastly, a self-powered sensing system was exhibited for the demonstration.

Chapter 4 illustrates the development of a novel micro- triboelectric energy harvester (μTEH), from the working mechanism to fundamental characterizations. The TENG was firstly and successfully fabricated based on MEMS technologies.

In Chapter 5, two potential applications of the μTEH are proposed. In addition, optimization methodologies are also given to improve the output of the μTEH in the future.

Chapter 6 summarizes the work in this thesis and gives future plans.

Chapter 2

Review of triboelectric nanogenerators

Triboelectric effect is one of the most common phenomena in our daily life. A typical example is that confetti is attached to the glass by rubbing glass and silk (shown as Fig. 2.1).

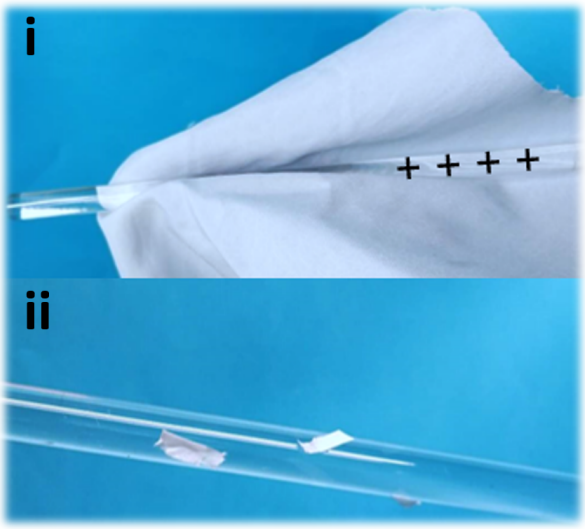

Figure 2.1: Triboelectrification between glass and silk.

For a very long time, people are trying to avoid the triboelectrification phenomena in the industry due to its negative effects, such as the high-voltage breakdown in IC. Until 2012, it was first proposed that triboelectricity is also a type of useful energy. Based on this idea, triboelectric nanogenerator (TENG) was proposed to scavenge mechanical energy and generate electrical energy, via the coupling of triboelectrification and electrostatic induction. Since invention, numerous studies have been conducted and TENGs have been applied in many different fields.

This chapter will give an introduction to the fundamental principles and the working behaviors of TENG. Up-to-date major applications are also reviewed at last.

2.1 Fundamental principles of triboelectric nanogenerator

2.1.1 Origin of nanogenerator

To pursue the origin and explain the working mechanism of TENG, we should go back to the Ampère's circuital law with Maxwell's addition [30, 31]

$$\nabla \times \boldsymbol{H} = \boldsymbol{J}_f + \frac{\partial \boldsymbol{D}}{\partial t} \tag{2.1}$$

where $\boldsymbol{H}$ is magnetizing field, $\boldsymbol{J}_f$ is the free electric current density and $\boldsymbol{D}$ is the displacement field.

$$\boldsymbol{D} = \varepsilon_0 \boldsymbol{E} + \boldsymbol{P} \tag{2.2}$$

where E is electric field, P is polarization field and ε_0 is the vacuum permittivity.

Substituting Eq. 2.2 into 2.1, we obtain the second term of Eq. 2.1

$$\boldsymbol{J}_D = \frac{\partial \boldsymbol{D}}{\partial t} = \varepsilon_0 \frac{\partial \boldsymbol{E}}{\partial t} + \frac{\partial \boldsymbol{P}}{\partial t} \tag{2.3}$$

which is so-called Maxwell's displacement current. The first component ($\varepsilon_0 \frac{\partial \boldsymbol{E}}{\partial t}$) is the current induced by the time-varying electric field, which is the origin of electromagnetic wave. The second component ($\frac{\partial \boldsymbol{P}}{\partial t}$) is the current contributed by the time-varying small motion of charges bound in atoms and dielectric polarization of materials, which can theoretically explain the

working principles of nanogenerator [32]. The output of both piezoelectric nanogenerator (PENG) and triboelectric nanogenerator (TENG) is the electron flow in the external circuit driven by the polarized charges and the induced time-varying electric field. The difference is that the induced electric field of PENG is inside the piezoelectric material while the induced electric field of TENG is between the triboelectric pair. The following part will give a brief discussion of the governing equations for both PENG and TENG.

- Piezoelectric nanogenerator

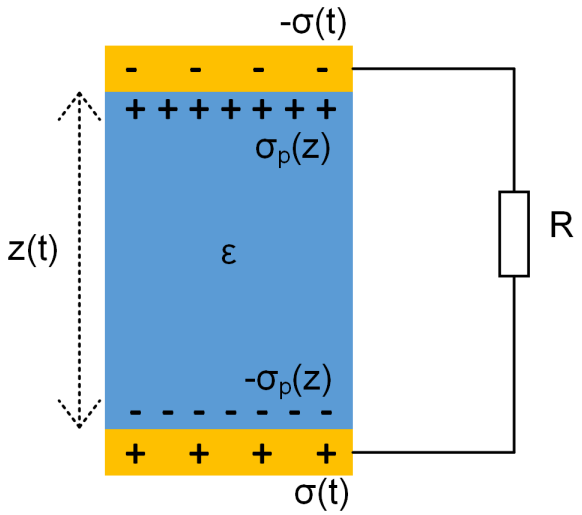

Figure 2.2: Working principle of piezoelectric nanogenerator.

The working principle of the PENG is illustrated in Fig. 2.2. For a piezoelectric material, the polarized charges are usually induced by the applied stress at two sides. Without external electric field, the displacement field is the polarization vector in the medium. If we take the z-axis as the polarization direction, we can obtain

$$D_z = P_z = \sigma_P(z) \tag{2.4}$$

where $\sigma_P(z)$ is the surface charge density contributed by the piezoelectric polarization. So, the displacement current (J_D) inside the piezoelectric material is given as

$$J_D = \frac{\partial P_z}{\partial t} = \frac{\partial \sigma_P(z)}{\partial t} \tag{2.5}$$

It can be observed that the displacement current of PENG is the change rate of the surface charge density by the piezoelectric polarization. The induced electric potential difference between two electrodes forces the electrons to flow in the external circuit. Assuming the piezoelectric material is an ideal insulator, the open-circuit voltage (V_{OC}) and the output current equation of the PENG are expressed as [32]

$$V_{OC} = \frac{z\sigma_P(z)}{\varepsilon} \tag{2.6}$$

$$RA\frac{d\sigma}{dt} = \frac{z[\sigma_P(z) - \sigma(t)]}{\varepsilon} \tag{2.7}$$

where R is the load resistance, A is the electrode area, $\sigma(t)$ is the charge density in electrode and z is the distance (a function of time t). According to Eq. 2.5 and 2.6, both the piezoelectric polarization and the change rate of the surface charge density contribute to the output of PENG.

- Triboelectric nanogenerator

For TENG, the polarized charges are contributed by the triboelectrification and trapped on the contacting surfaces. Then, the free electrons flow through the external circuit. The working principle is illustrated in Fig. 2.3. The electric field in the triboelectric materials (E_1, E_2) and the gap (E_g) are defined as [32]

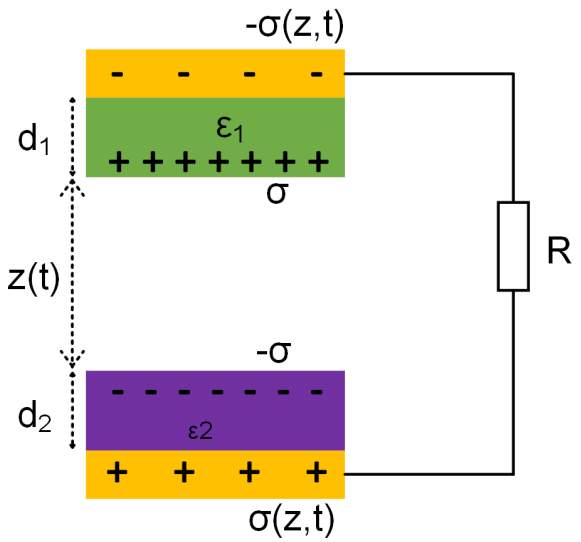

Figure 2.3: Working principle of triboelectric nanogenerator.

$$\begin{aligned} E_1 &= \sigma(z,t)/\varepsilon_1 \\ E_2 &= \sigma(z,t)/\varepsilon_2 \\ E_g &= [\sigma(z,t) - \sigma]/\varepsilon_0 \end{aligned} \tag{2.8}$$

where $\sigma(z,t)$ is the charge density in the electrode (a function of the separation $z(t)$), σ is the surface charge density on the triboelectric material, ε_1 and ε_2 are the relative dielectric constants. The electric potential drop between electrodes is

$$V = \sigma(z,t)[d_1/\varepsilon_1 + d_2/\varepsilon_2] + z[\sigma(z,t) - \sigma]/\varepsilon_0 \tag{2.9}$$

Under the short-circuit condition, $V = 0$. So, we obtain

$$\sigma(z,t) = \frac{z\sigma}{d_1\varepsilon_0/\varepsilon_1 + d_2\varepsilon_0/\varepsilon_2 + z} \tag{2.10}$$

Then, the displacement current inside the triboelelctric materials is expressed as

$$J_D = \frac{\partial D_z}{\partial t} = \frac{\partial \sigma(z,t)}{\partial t} = \sigma \frac{dz}{dt} \frac{d_1\varepsilon_0/\varepsilon_1 + d_2\varepsilon_0/\varepsilon_2}{[d_1\varepsilon_0/\varepsilon_1 + d_2\varepsilon_0/\varepsilon_2 + z]^2} + \frac{d\sigma}{dt} \frac{z}{d_1\varepsilon_0/\varepsilon_1 + d_2\varepsilon_0/\varepsilon_2 + z} \tag{2.11}$$

The second term in the Eq. 2.11 shows the relationship between the displacement current and the change rate of the surface charge density on triboelectric materials. After sufficient contact, the surface charges almost saturate on triboelectric materials, resulting in a constant surface charge density. Thus, the second term will be zero at steady state and Eq. 2.11 is only determined by the first term. Consequently, the displacement current of TENG is only related to the surface charge density on triboelectric materials and the velocity of the relative movement between the triboelectric pair.

In the external circuit, the output current equation of TENG is expressed as [32]

$$RA \frac{d\sigma(z,t)}{dt} = z\sigma/\varepsilon_0 - \sigma(z,t)[d_1/\varepsilon_1 + d_2/\varepsilon_2 + z/\varepsilon_0] \tag{2.12}$$

2.1.2 Triboelectric materials

Almost all of the known materials have the triboelectric properties, including metals, polymers, woods and *etc*. Fig. 2.4 illustrates a triboelectric series of some common materials [26]. In the series, materials close to the positive end tend to lose electrons (positively charged) while materials close to the negative end tend to gain electrons (negatively charged).

Other than the material itself, the surface properties of a material can also contribute to the triboelectric property. By physically creating nano-/micro- patterns on the surface [33–35] or chemically functionalizing the surface [36–38], materials will be easier to gain/lose electrons after contact. The mechanism behind this is that the surface modification, either physically or

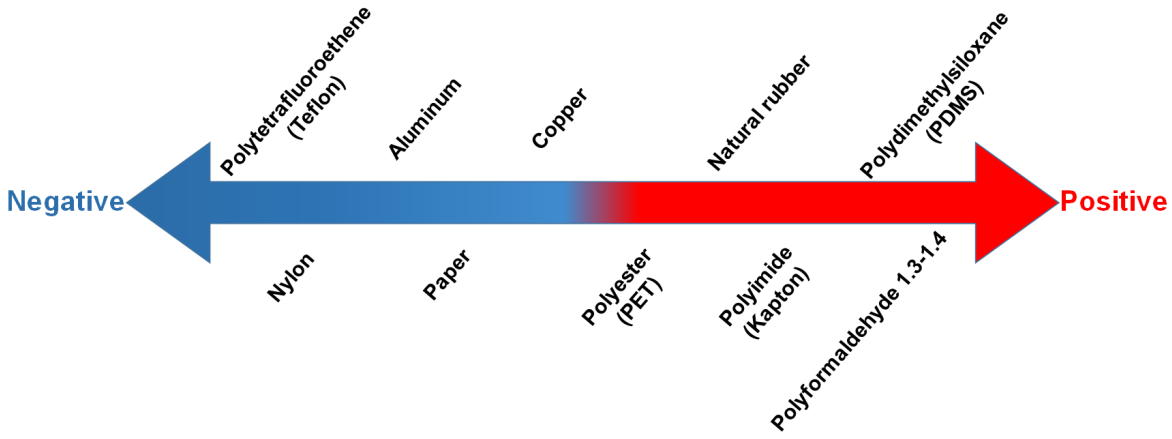

Figure 2.4: Triboelectric series of some common materials.

chemically, can significantly change the surface potential, resulting in a change of the capability of gaining/losing electrons. Typically, materials located further away on the triboelectric series are preferred to construct TENG because electrons are easier to transfer from one to the other.

2.1.3 Output characteristics of TENG

For all kinds of TENGs, the working mechanism is the coupling of contact triboelectrification and electrostatic induction. Essentially, a TENG contains a pair of electrodes, insulated with each other. The resistance between electrodes is assumed infinitely large to ensure that charges can only flow through external circuit. To theoretically analyze the working behaviors of a TENG, the TENG can be fundamentally modeled as a time-varying capacitor. If the transferred charges between electrodes are defined as Q, one electrode will have the positive charges Q and the other one has the negative charges $-Q$. For any TENG, two components contributes to the electric potential difference. One is from the polarized triboelectric charges and the other one is from the already transferred charge Q. Based on the electric potential superposition principle, the actual electric potential difference (V) between electrodes is given as [39]

$$V = -\frac{1}{C_{(x)}}Q + V_{OC}(x) \tag{2.13}$$

where $C(x)$ is the capacitance between two electrodes and $V_{OC}(x)$ is the electric potential drop induced by the polarized triboelectric charges with certain separation (x). Here, Eq. 2.13, so-called $V - Q - x$ relationship, is the governing equation of an arbitrary TENG.

Under the short-circuit condition, the transferred charges (Q_{SC}) will completely screen the electric potential difference induced by the polarized triboelectric charges. Therefore, the fundamental relationship among Q_{SC}, C and V_{OC} is $Q_{SC}(x) = C_(x)V_{OC}(x)$ [40].

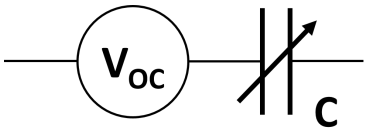

Figure 2.5: First-order lumped parameter equivalent circuit mode of an arbitrary TENG.

Based on the $V - Q - x$ relationship (Eq. 2.13), a first-order lumped parameter equivalent circuit model can be built to analyze the behaviors of TENG [41]. The two terms at the right side of Eq. 2.13 can represent a capacitance term and an open-circuit voltage term, respectively. In consequence, the lumped parameter equivalent circuit mode is exhibiting as a series of an ideal voltage source and a time-varying capacitor (shown as Fig. 2.5). For an arbitrary TENG, there is no resistance term in the equivalent circuit. Therefore, the inherent impedance of the TENG is only related to the capacitive term. On the basis of the lumped equivalent mode of TENG, two typical conditions will be discussed in the following section.

- Output of TENG with resistive load

Fig. 2.6a is the equivalent circuit model of a TENG with the load resistance. According to Kirchhoff's law, the governing equation is given as [42]

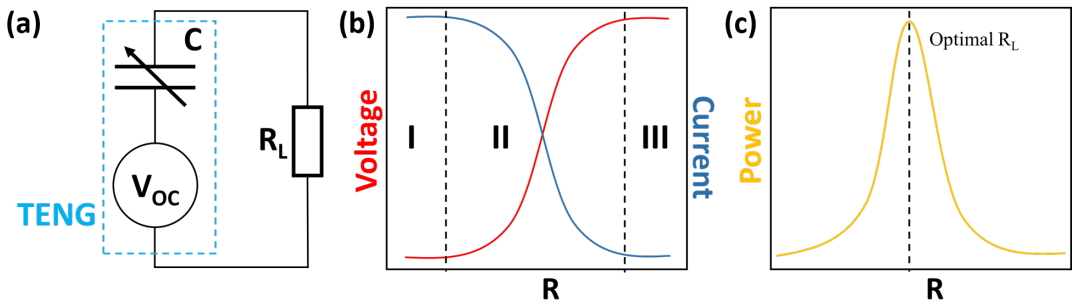

Figure 2.6: (a) The equivalent circuit mode of TENG with resistive load. (b) The output voltage and current dependence on the load resistance. (c) The output power dependence on the load resistance.

$$R\frac{dQ}{dt} = -\frac{1}{C}Q + V_{OC} \tag{2.14}$$

Fig. 2.6b gives the effect of the load resistance on the peak output voltage and current. It is obvious that three regions can be divided, marked as I, II and III. This characteristic can be explained by charge transfer velocity [42, 43]. Indeed, the output current of the TENG is an external expression of the charge transfer velocity in external circuit. The charge transfer velocity in external circuit has the maximum value in short-circuit condition and the existence of load resistance constrains the charge transfer velocity. In region I, the load resistance is small and has a negligible effect on the charge transfer velocity. The output current is almost equal to the short-circuit current. At the same time, the electric potential drop is nearly balanced by the transferred charges, generating a very small output voltage. In region II, as the load resistance continues to increase, the charge transfer velocity is significantly lowered and the output current decreases rapidly. The electric potential drop is less balanced due to the less transferred charges. As a result, the output voltage increases. When the load resistance is sufficiently large, the charge transfer in the external circuit is almost blocked, resulting in an extremely small output current. Since very few charges are transferred in the external circuit, the output voltage almost keeps consistent to the open-circuit voltage. This is the region III.

To mathematically express the output of the TENG, impedance matching between TENG and the load resistance is often adopted to analyze the output characteristics as well [44, 45]. Since the inherent capacitance of a TENG is not constant, the average inherent capacitance (C_{avg}) is used in the calculation. The corresponding average inherent impedance of the TENG is $1/(\omega C_{avg})$ (ω is the angular frequency of the mechanical movement). In region I, the load resistance is much smaller than the average inherent impedance of the TENG and circuit can be considered as a quasi-short-circuit condition. In region III, the load resistance is much larger than the average inherent impedance of the TENG and the circuit can be considered as a quasi-open-circuit condition. In both regions, the output power on the load resistance is small. In region II, both the output voltage and current are sensitive to the value of load resistance. The maximum output power can also be reached in this region, as illustrated in Fig. 2.6c. Niu *et al.* [43] gave the expression of the optimum load resistance (R_{opt}), corresponding to the maximum output power.

$$R_{opt} = \frac{d_0^2}{[H(\frac{x_{max}}{d_0})]^2 S v \varepsilon_0} \tag{2.15}$$

where d_0 is the effective thickness of the dielectric, x_{max} is the maximum displacement, S is the area of triboelectric material and v is the velocity of the mechanical movement. H is a function to describe the detailed relative movement.

The TENG with load resistance is the simplest case in the real application. These characteristics are often applied for the self-powered sensing application because most the sensing systems are based on the resistance-type sensors. When the working range of the sensors is located in region II, sensing results will be directly demonstrated by the output voltage of TENG.

- Output of TENG with capacitive load

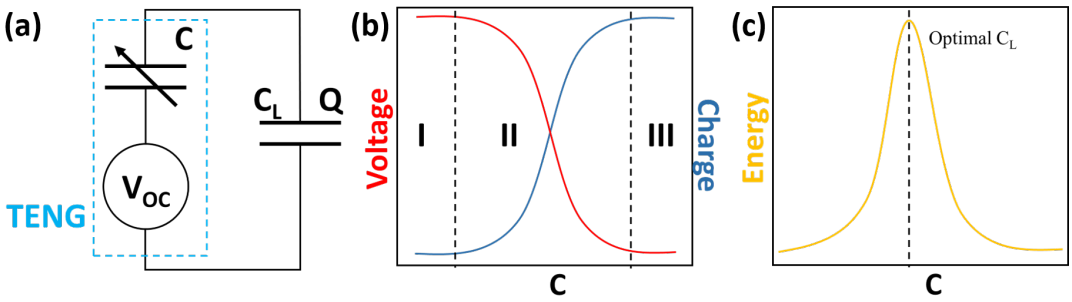

Figure 2.7: (a) The equivalent circuit mode of TENG with capacitive load. (b) The output voltage and transferred charges dependence on the load capacitance. (c) The stored energy dependence on the load capacitance.

Fig. 2.7a is the equivalent circuit model of a TENG with load capacitance. In this case, there is no external resistance term in the circuit and it is more meaningful to discuss the transferred charges and stored energy in load capacitor, instead of output current and power [41, 42]. Although the behavior of the TENG is time-varying, the distribution of charges is certain in the circuit at any moment. Typically, the open-circuit voltage (V_{OC}) of the TENG reaches the peak value at the maximum displacement (x_{max}). We take this peak V_{OC} for further discussion. At this point, the instantaneous voltage (V) and charges (Q_C) on the load capaitance are expressed as [42]

$$V = \frac{Q_{SC}(x = x_{max})}{C_L + C_T} \tag{2.16}$$

$$Q_C = \frac{C_L Q_{SC}(x = x_{max})}{C_L + C_T} \tag{2.17}$$

where $Q_{SC(x=max)}$ is the transferred charges of the TENG in short-circuit condition, C_L is the load capacitance and C_T is the instantaneous inherent capacitor of the TENG. Based on the Eq. 2.16 and 2.17, the total stored energy in load capacitance can be obtained as

$$E_C = \frac{1}{2}C_L V^2 = \frac{C_L[Q_{SC}(x = x_{max})]^2}{2(C_L + C_T)^2} \tag{2.18}$$

The three-working-region behavior can also be observed for the capacitive load characteristics, as shown in Fig. 2.7b. For a certain TENG and movement, the maximum transferred charges in short-circuit condition is a fixed value. It is easy to obtain the dependency of charges, voltage and stored energy on the load capacitance from Eq. 2.16, 2.17 and 2.18. Similar to the resistive load characteristics, there is also an optimum value (C_{opt}) of the load capacitor that makes the stored energy in the load capacitance maximized. Based on Eq. 2.18, maximum stored energy is reached when $C_L = C_{opt} = C_T$.

Currently, a supercapacitor is usually connected with the TENG to store the generated energy. Therefore, the characteristics of the TENG output with load capacitance are useful when designing the supercapacitor to maximize the stored energy. So far, few researches have been performed on the combination of TENG and capacitance-type sensors. In chapter 3, it is observed that operating frequency of the TENG has an effect on the output voltage with load resistance, but has no effect on that with load capacitance. These characteristics may promote the development of the frequency-independent self-powered sensing systems.

2.2 Basic working modes of triboelectric nanogenerators

Depending on the configurations, TENGs are working under four basic operating modes. This section will respectively introduce these four working modes.

2.2.1 Vertical contact-separation mode

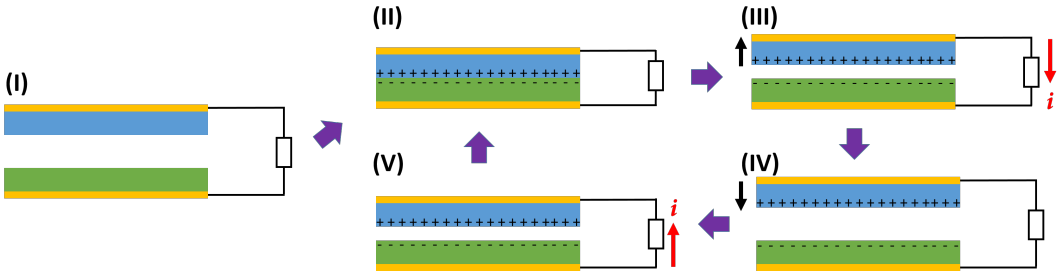

Figure 2.8: Working mechanism of vertical contact-separation mode TENG in single working cycle.

Vertical contact-separation mode is the simplest working mode of TENG, which can be divided into two categories: dielectric-to-dielectric and conductor-to-dielectric. Fig. 2.8 illustrates the working mechanism of the dielectric-to-dielectric case. Initially, two different triboelectric materials are brought into contact by external mechanical force. Opposite charges with same density are distributed on the surfaces of the two materials according to the electron affinity. When being separated from each other, there will be an electric potential difference between two electrodes attached to dielectric layers. The electric potential difference increases with the increase of separation and will reach the maximum with the maximum separation. Due to the electric potential difference, free electrons are transferred through external circuit. Then, electric potential difference decreases when two materials are forced into contact again. To balance the potential difference, electrons will flow back through the external circuit. Alternating current (AC) is generated when this process is repeated periodically. Based on the theoretical model proposed by Niu *et al.* [43], the open-circuit voltage (V_{OC}) and short-circuit current (I_{SC}) are defined as

$$V_{OC} = \frac{\sigma x(t)}{\varepsilon_0} \tag{2.19}$$

$$I_{SC} = \frac{S\sigma d_0 v(t)}{d_0 + x(t)^2} \tag{2.20}$$

where σ is the surface charge density of the triboelectric material, $x(t)$ is the separation between two triboelectric layers, S is the contact area and $v(t)$ is the relative velocity of the two triboelectric layers. d_0 is the effective thickness of dielectric layers between two electrodes, defined as

$$d_0 = \sum_{i=1}^{n} \frac{d_i}{\varepsilon_{ri}} \tag{2.21}$$

where the *ith* dielectric layer has the thickness of d_i and relative dielectric constant of ε_{ri}.

TENGs working under the vertical contact-separation mode have the advantages of simplest configuration, high output power and easier construction of multilayered structure. They have been widely applied for portable electronics and self-powered sensors [38, 46].

2.2.2 Lateral sliding mode

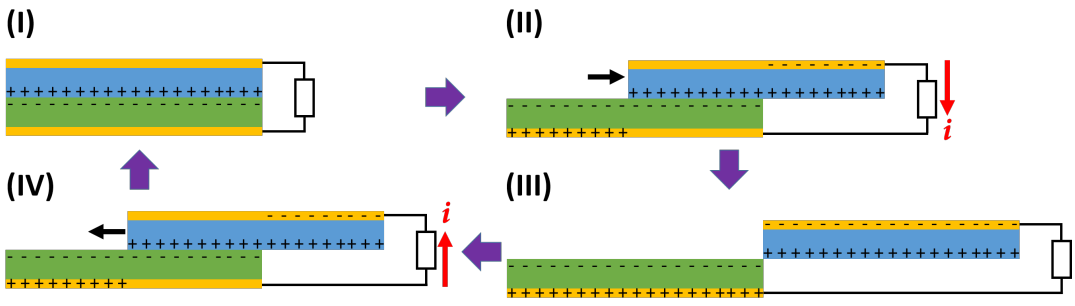

Figure 2.9: Working mechanism of lateral sliding mode TENG in single working cycle.

Lateral sliding mode TENG has the similar configuration as that of contact-separation mode TENG. The difference is that the relative motion direction between two triboelectric layers is in-plane for lateral sliding mode. This working mode is also classified into two types:

dielectric-to-dielectric and conductor-to-dielectric. Shown as Fig. 2.9, positive and negative charges are equally distributed on the surfaces of two triboelectric layers after sufficiently contacting. When one triboelectric layer slides out, electric potential difference is generated between two electrodes and the potential difference increases with further relative motion. A current is induced in the external circuit under the potential drop. Similarly, current flows back when the triboelectric layer slides in. Based on the theoretical mode [39], the open-circuit voltage (V_{OC}) and short-circuit current (I_{SC}) are given as

$$V_{OC} = \frac{\sigma x(t) d_0}{\varepsilon_0 (l - x(t))} \tag{2.22}$$

$$I_{SC} = \sigma w v(t) \tag{2.23}$$

where $x(t)$ is the relative lateral separation between two triboelectric layers, l is the length of triboelectric layer in motion direction, w is the width of the triboelectric layer perpendicular to the page in Fig. 2.9 and $v(x)$ is the relative velocity between two triboelectric layers.

Compared to vertical contact-separation mode TENG, lateral sliding mode TENG is more compatible for packaging because there is no gap required in the structure.

2.2.3 Single electrode mode

For single electrode mode TENG, only one electrode is fabricated, which is referred as the primary electrode. As shown in Fig. 2.10, ground is taken as the reference electrode in most cases. Still, TENGs working under single electrode mode can be divided into dielectric-to-dielectric and conductor-to-dielectric. Since the relative motion between two triboelectric layers can be horizontal or vertical, the theoretical mode should be discussed separately [40].

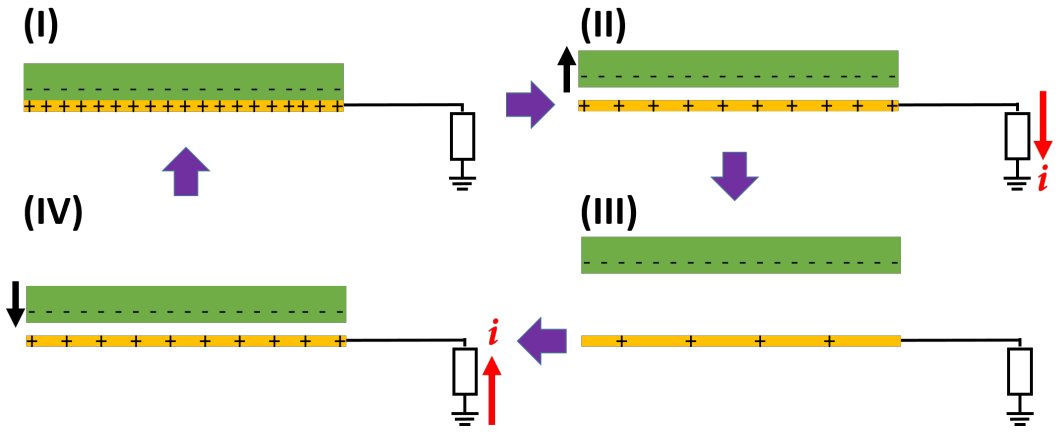

Figure 2.10: Working mechanism of single electrode mode TENG in single working cycle.

Here, we only talk about the vertical relative motion for illustration, depicted in Fig. 2.10. After enough contacting, opposite charges are distributed on the surfaces of dielectric layer and primary electrode equally. Once separated, an electric potential drop is built between the primary and the reference electrodes. A current is generated in the external circuit accordingly. When the dielectric layer moves back to primary electrode, the potential drop decreases and the induced current flows back. The theoretical mode gives the expressions of open-circuit voltage (V_{OC}) and short-circuit transferred charges (Q_{SC}) [40]

$$V_{OC} = \frac{\sigma w l C_2}{C_1 C_2 + C_2 C_3 + C_3 C_1} \tag{2.24}$$

$$Q_{SC} = \frac{\sigma w l}{1 - \frac{C_1(x)}{C_2(x)}} \tag{2.25}$$

where C_1, C_2 and C_3 are the capacitances of the dielectric layer to the primary electrode, the dielectric layer to the reference electrode and the primary electrode to the reference electrode, respectively.

For vertical contact-separation mode TENG and sliding mode TENG, two electrodes (attached to triboelectric layers) need to be fabricated for a closed circuit, which may cause some

practical problems in real applications. On the contrary, only one electrode is required in single electrode mode TENG and the triboelectric layer can move freely. Although the output power is halved compared to the two abovementioned types of TENGs (due to the screening effect of the primary electrode), single electrode mode TENG has more practical applications.

2.2.4 Freestanding triboelectric-layer mode

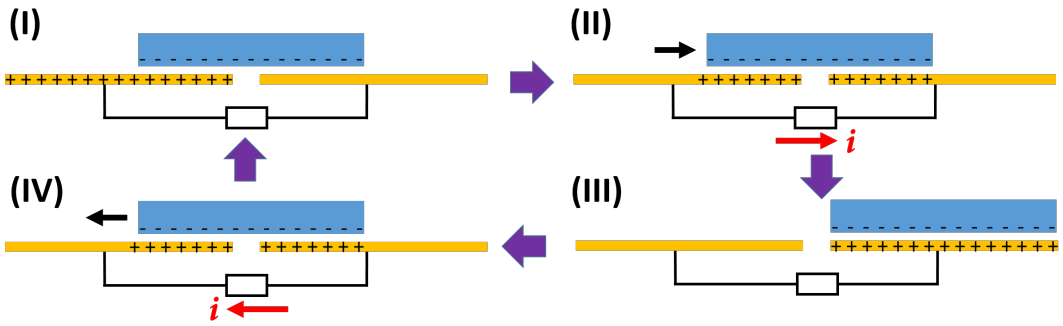

Figure 2.11: Working mechanism of freestanding triboelectric-layer mode TENG (sliding) in single working cycle.

For freestanding triboelectric-layer mode, the configuration is a bit complicated compared to other three modes. The triboelectric layer can vertically move between two parallel electrodes or laterally move on the same thin film. Similarly, freestanding triboelectric-layer mode includes dielectric-to-dielectric and conductor-to-dielectric. Fig. 2.11 illustrates the working mechanism of the freestanding triboelectric-layer TENG in sliding mode. In one working cycle, sufficiently charged triboelectric layer moves laterally, so that two electrodes underneath are oppositely charged. Depending on the overlapping areas, electric potential difference is induced between two electrodes and current is generated in the external circuit. Since the capacitance between two completely misaligned electrodes is dominated by the fringing effect, it is difficult to find a proper equation to calculate the total capacitance of TENG. Hence, the exact expressions of open-circuit voltage and short-circuit current are quite complicated. Com-

prehensive theoretical discussions of freestanding triboelectric-layer mode TENG can be found in reference [47].

Freestanding triboelectric-layer mode TENG also has the advantage that triboelectric layer can move freely. However, a significant superiority to single electrode mode TENG is higher energy conversion efficiency because there is no screening effect.

2.3 Major applications of triboelectric nanogenerators

Over the last five years, a great number of researches concentrated on the diverse applications of TENG. Among them, three major categories can be summarized: self-powered sensing, power source and human-machine interfacing (HMI). This section will briefly review the recent progress.

2.3.1 Self-powered sensing

By integrating with TENG, sensing systems can work without external power source. Most current TENG-based self-powered sensing systems are working under the mechanism of impedance matching effect. Essentially, the change of the environment will cause the change of load impedance, further inducing the change of the output of the TENG. Numerous reported publications have exhibited TENG-based self-powered sensing systems in various scenarios.

Applying one polytetrafluoroethylene (PTFE) layer functioning as both triboelectric layer and sensing layer, Jie *et al.* [48] designed a vertical contact-separation mode TENG for dopamine detection. This self-powered sensing system can detect the dopamine with the limit of 0.5 μM in alkaline condition. By the coupling of triboelectric effect and chemresistive effect, Shen *et al.* [44] designed a self-powered NO_2 gas sensing system for vehicle emission testing. The

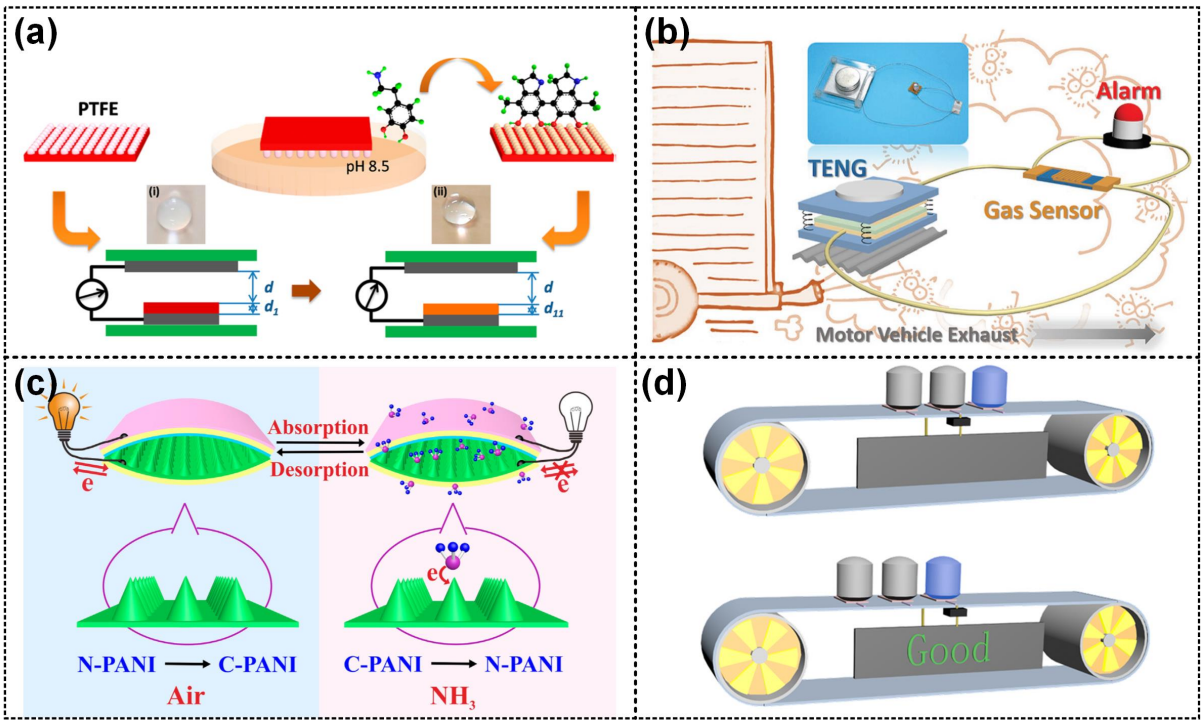

Figure 2.12: Self-powered sensing systems based on TENG. (Reprinted with permissions) (a) A self-powered sensing system for dopamine detection in alkaline solution [48]. (b) A self-powered vehicle emission testing system for NO_2 detection [44]. (c) A self-powered NH_3 sensing system based on PANI-TENG [49]. (d) A self-powered weighing system to monitor the qualified/unqualified weight product [45].

contact-separation mode TENG, seriesly connected with a WO_3-based gas sensor, was fixed on the automobile engine to harvest the vibration energy. Cui *et al.* [49] constructed a contact-separation mode TENG for ammonia sensing in the environment. In their system, the conducting polyaniline (PANI) nanofibers act as both triboelectric layer and electrode. The output of the TENG varies with the ammonia concentration and the detection limit can reach ~500 ppm at room temperature. Similar work is also reported for CO_2 sensing [50].

A variety of self-powered pressure/force senors were also proposed. Guo *et al.* [51] proposed a single-electrode mode TENG for pressure sensing. Graphene oxide (GO) was used for triboelectric material to enhance the output, where the sensitivity can achieve up to 388 μA/Mpa. Xie *et al.* [45] reported a carbon nanotude (CNT) based piezoresistive pressure sensor, integrated with a disc-shaped TENG working under the freestanding triboelectric-layer

mode. The variation of the detected pressure can be directly reflected by the output of the TENG.

2.3.2 Power source

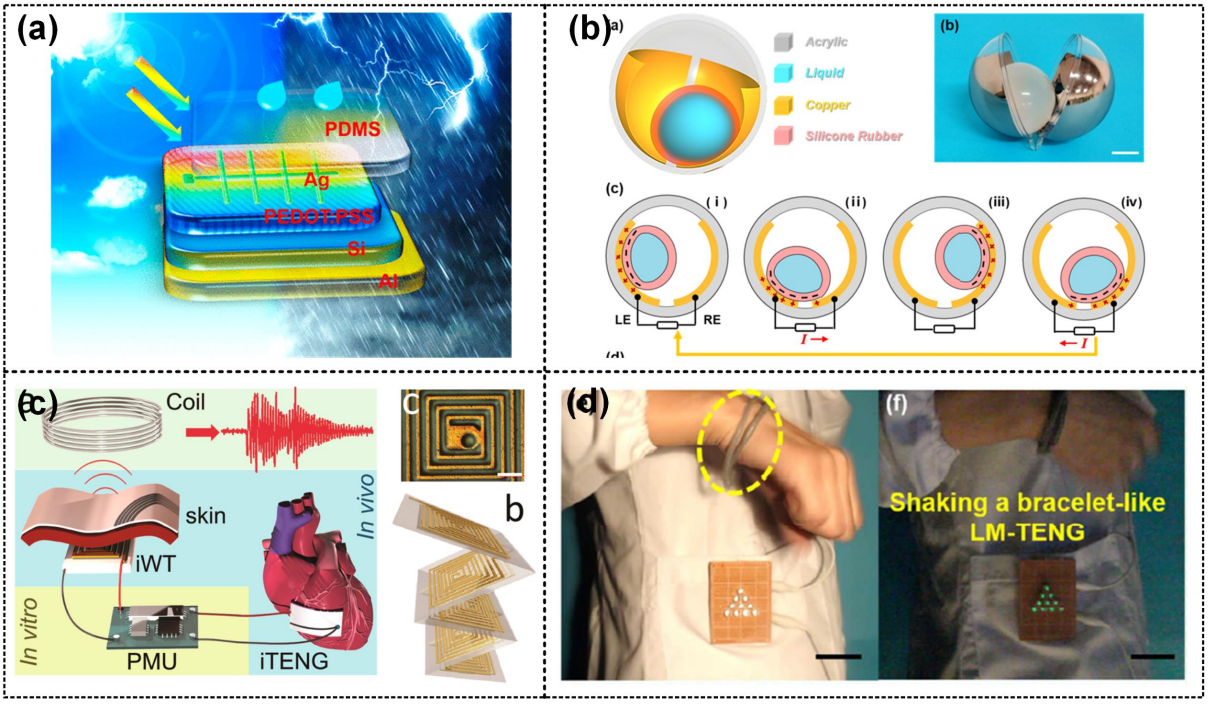

Figure 2.13: Power sources based on TENG. (Reprinted with permissions) (a) A hybrid energy harvesting system to collect the solar energy and the kinetic energy of raindrops [52]. (b) Soft-contact-mode spherical TENG to harvest the low frequency wave energy on ocean [53]. (c) A wireless heart rate monitoring system based on the TENG [54]. (d) Liquid-metal-based TENG for harvesting mechanical energy from arm shaking [55].

According to the different energy source (environmental mechanical source and bio-mechanical source), the TENGs are generally developed toward two directions.

TENGs with various configurations have been designed to harvest the wind energy. Zhao *et al.* [56] and zhang *et al.* [57] designed flag-structured and lawn-structured TENG respectively, which can scavenge wind energy from arbitrary direction. Cheng *et al.* [58] proposed a wind energy harvesting system with two different configurations. In their system, one is flutter-driven TENG for low-speed airflow and the other one is a disc-shaped TENG for strong airflow,

so that it can maximize the harvested energy for both low-speed and high-speed airflow. Another environmental mechanical energy is the low-frequency water wave energy in the ocean. Cheng *et al.* [53] fabricated a soft liquid/silicone and sealed it inside an acrylic hollow sphere. This sphere-structured TENG works under the combination of freestanding triboelectric-layer mode and contact-separation mode and can output 45 mW power. By building the sphere-structured TENG network in the ocean, large-scale blue energy harvesting may be realized to alleviate energy crisis. Liang *et al.* [59] proposed a multilayered structure (glass-FTO-PTFE) to harvest the electrostatic energy from the flowing water on the top surface. Then, Liu *et al.* [52] put forward a hybrid system, where polydimethylsiloxane (PDMS) as triboelectric layer combined with PEDOT:PSS layer as electrode was stacked on the silicon solar cell. This hybrid system can harvest energy from environment in different weather conditions.

Additionally, a lot of TENGs targeting harvesting bio-mechanical energy are designed to power wearable devices. Flexible materials are preferred to fit the wearable devices. They can harness the human motions, such as bending of elbow and flexion of fingers, and charge supercapacitors as power source. Yang *et al.* [55] fabricated a flexible TENG based on liquid metal (Galinstan) to harvest the energy from human walking and arm shaking. In their design, liquid metal acts as electrode and silicone rubber acts as triboelectric layer to make the whole system system flexible. Sun *et al.* [60] designed an ultralight energy harvesting system, where both the TENG and the supercapacitor were fabricated by electrospun paper. Among the TENGs scavenging bio-mechanical energy, a particular type of TENG was designed for implanted device. Zheng *et al.* [54, 61, 62] used micro-/nano- patterned polymer (PDMS, PTFE) as triboelectric materials to fabricated flexible TENGs. Attaching to the organs (such as heart), these contact-separation mode TENGs can harvest the bio-mechanical energy inside human body and power implanted devices.

2.3.3 Human-machine interfacing

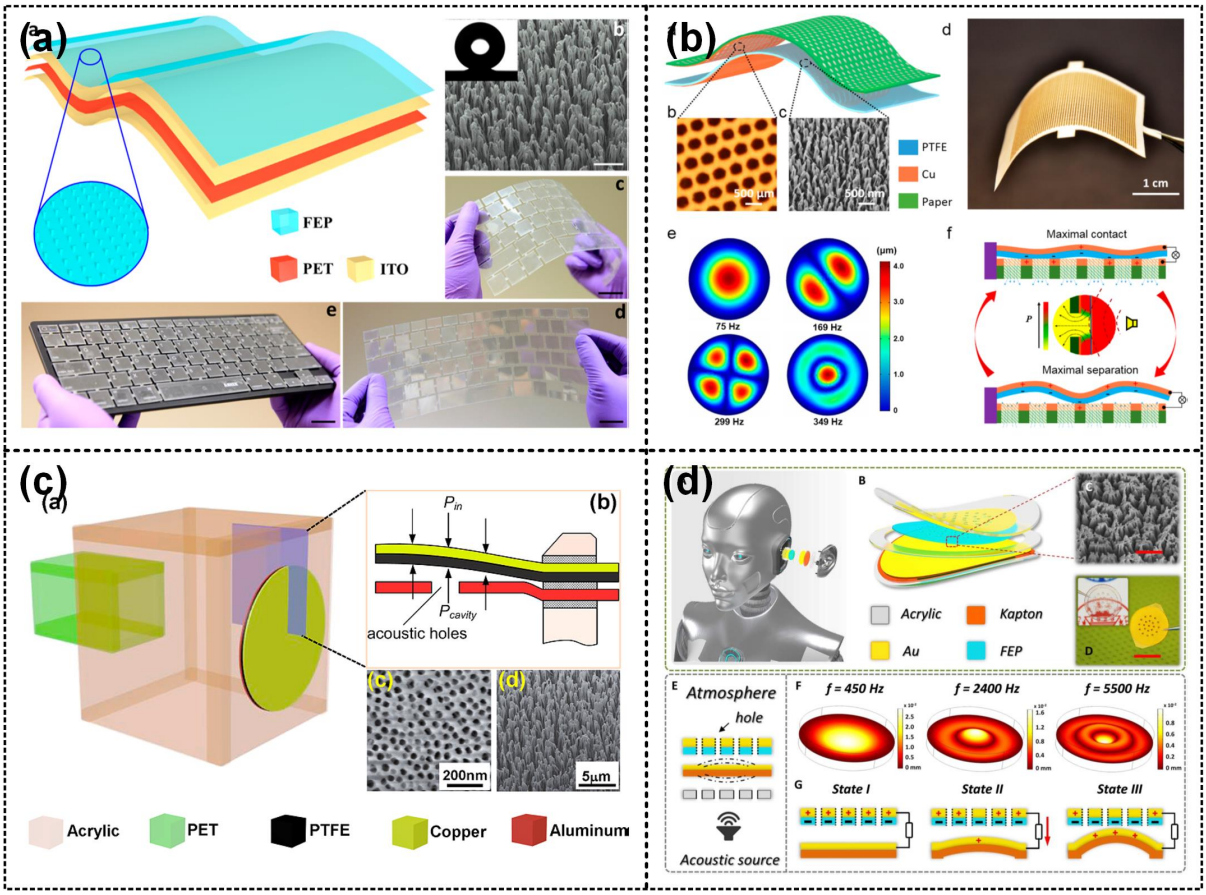

Figure 2.14: HMI applications based on TENG. (Reprinted with permissions) (a) A self-powered intelligent keyboard based on the single electrode mode TENG [63]. (b) A paper-based TENG for acoustic energy harvesting and self-powered sound recording [64]. (c) An organic thin-film-based TENG for active acoustic sensing [65]. (d) An ultrasensitive auditory sensor based on TENG [66].

The human-machine interfacing (HMI) application is beneficial from the high output voltage of the TENG. Usually, TENGs function as sensing component and should be integrated with a post signal processing component.

One typical example of HMI is record of keystroke dynamics for identification [63, 67, 68]. In this application, fluorinated ethylene propylene (FEP) is coated onto the ITO surface as an

triboelectric layer and the TENG works under the single-electrode mode. By the construction of an array, a keyboard cover can be fabricated and be used to record keystroke dynamics. Jie *et al.* [69] designed a TENG, in which nitrocelluse membrane was used as triboelectric layer. This freestanding triboelectric-layer mode TENG can work for a self-triggered alarm system by fingerprint. Pu *et al.* [70] fabricated a flexible TENG working under contact-separation mode and attached it to the glass. The micromotion of the skin around the corner of eyes can be detected and taken as a trigger signal source. Ultrahigh sensitivity can be achieved because of the high output voltage of TENG.

Yang *et al.* [65] and Fan *et al.* [64] firstly designed flexible TENG based on PTFE film for acoustic sensing applications. Multilayered structures were constructed and the acoustic-induced vibrations of PTFE generate electrical signals. Guo *et al.* [66] fabricated a TENG-based auditory sensor for cochlea device. They used FEP and kaption as triboelectric pair and the shape of membrane was comprehensively studied. In consequence, a broad bandwidth was achieved (100 to 5000 Hz) and the output voltage can reach 1.2 V under 100 dB sound pressure level.

Chapter 3

Self-powered on-line ion concentration monitor in water transportation driven by triboelectric nanogenerator

Water is one of the most indispensable substances not only in daily life but also in industrial production. According to the various industrial usage, such as preparation of purified reagent, manufacture of battery-related production and cleaning of electronics, different regulations of water quality should be met [71, 72]. Excess ions, particles and bacteria may lead to severe problem in industrial production. Although numerous water purification methods have been applied into practice and extremely pure water can be realized [73–76], contamination can still be introduced in the transportation of water. It is vitally meaningful to monitor the water quality on-line and in real time during the transportation. In the multitudinous factors for evaluating water quality, ion concentration is a symbolic element. Currently, many advanced ion concentration sensors are able to detect ions in water physically [77–79], chemically [80–82] and biologically [83–85]. Despite high sensitivity, most existing sensors suffer from complex sensing process and difficulty in real-time monitoring. Another prominent problem in common is power consumption. External energy source is usually required to drive the ionic sensor for an alarm system. When a large number of sensors implemented along the transportation pipeline, it is an enormous engineering effort to provide external electricity.

Among the external electric powers, battery is the most commonly-used way to power sensors. However, the lifespan of battery limits the long-term usage of the sensing system [86–88]. If the mechanical energy of water flow can be collected and utilized to drive sensors and alarms, it will be a perfect solution. Nowadays, the emerging TENG has addressed an approach to actuate multifarious electronic devices by harvesting energies from ambient [25, 32, 89]. Several efforts to achieve TENG-triggered self-powered sensing system have been made [27, 66, 70, 90, 91]. Among them, the most striking strategy is to develop appropriate TENGs which can drive the existing sensors directly based on the impedance matching effect between the TENG and sensor [44, 45, 92–94]. In a typical process, the specific output characteristics of the TENG are tuned by the load of the sensor that is responded to the external stimuli. The output voltage of TENG varies with the different working states of the sensor and can then directly reflect on the on/off status of the alarm unit such as LEDs.

In this work, a TENG driven self-powered on-line monitoring system in the pipeline transportation of water was proposed, introducing a new monitoring strategy. A turbo fan driven disc-shaped TENG (RD-TENG) was proposed to convert the mechanical energy of the flowing water in the pipeline to electrical energy. Both the RD-TENG and the ion concentration sensor were designed and fabricated based on the standard printed circuit board (PCB) technology. The sensor and the TENG were connected in series and connected a commercial LED with the fixed resistor in parallel as alarm. This work will be a good example of the TENG harvesting environmental energy.

3.1 Fabrication of TENG and sensor

3.1.1 Fabrication of RD-TENG

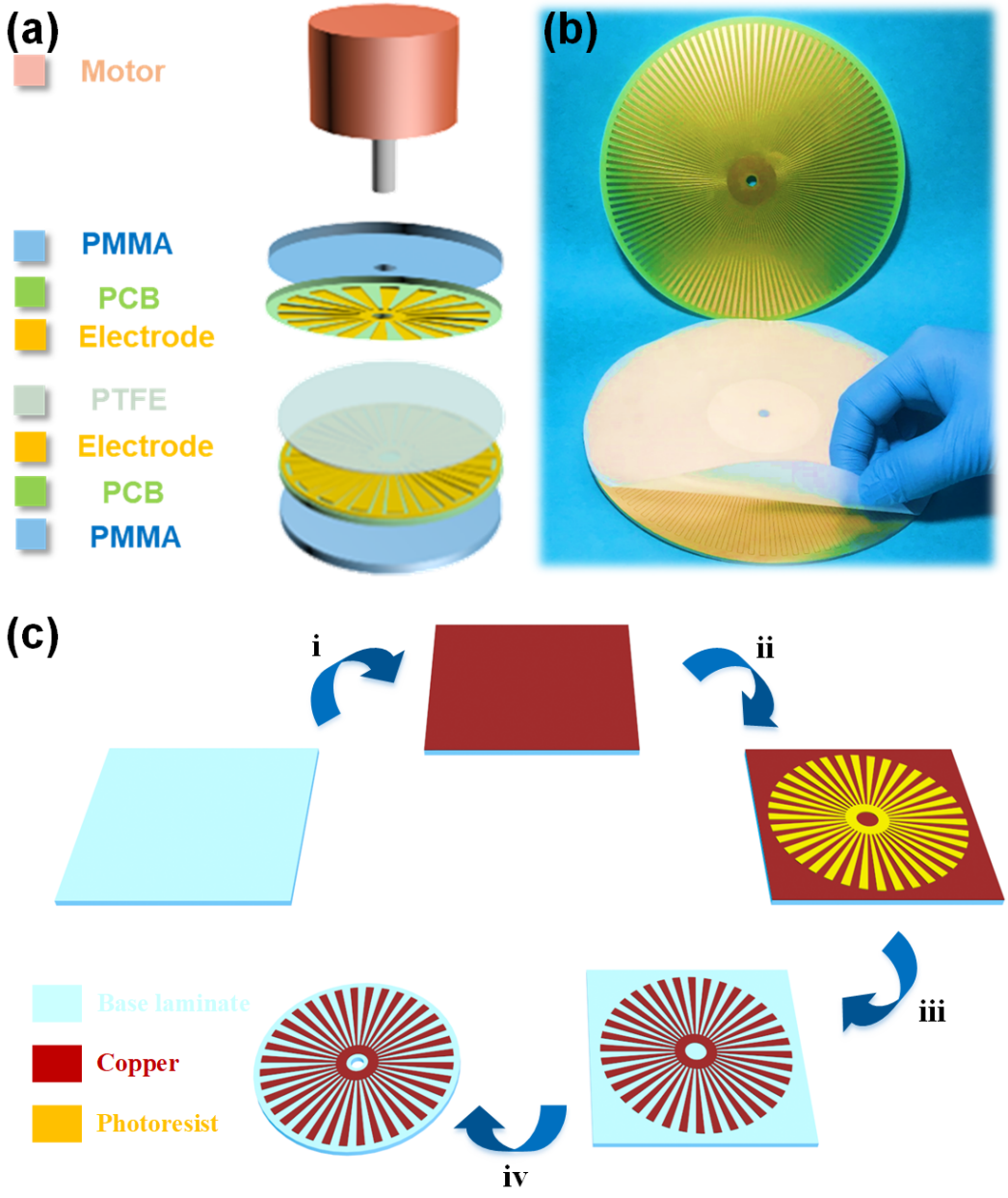

Figure 3.1: (a) The exploded view and (b) the photograph of a typical RD-TENG. (c) Fabrication process of the RD-TENG.

With a multilayered structure, the RD-TENG mainly contains a disk-shaped stator and a countered rotator, as shown in Fig. 3.1a and b. The fabrication of the RD-TENG is based on the mature industrial PCB manufacturing technology, shown as Fig. 3.1c. Different from handcrafted TENGs, TENG fabricated by PCB technology is more precise, more repeatable and more reliable. The fabrication started from the base laminate made from epoxy resin and glass fibers. (i) Then, copper sheet was coated on the surface of the base laminate. (ii~iii) To pattern the electrode, a photolithography and copper etching process were conducted. For the rotator, radial copper segments (70 μm thick) with a central angle of 1.5° were patterned on the PCB. The diameter of the radial copper segments is 176 mm. For the stator, two copper segments with interdigitated structure were patterned on the PCB. Detailed electrode structures of stator and rotator can be found in Appendix A and B. (iv) Lastly, the PCB was cut into pieces with the desired shape (circle with diameter of 184 mm).

A PTFE thin film, treated by plasma reaction ion etching (RIE) process for enhancing the surface charge density, was coated on the upper surface of stator (with copper electrodes). For both stator and rotator, PCB was adhered to a stack of acrylic (Polymeric Methyl Methacrylate) sheets to strengthen the structure. The acrylic sheets were cut by the laser cutter (Huitian Laser 4060).

3.1.2 Fabrication of ion concentration sensor

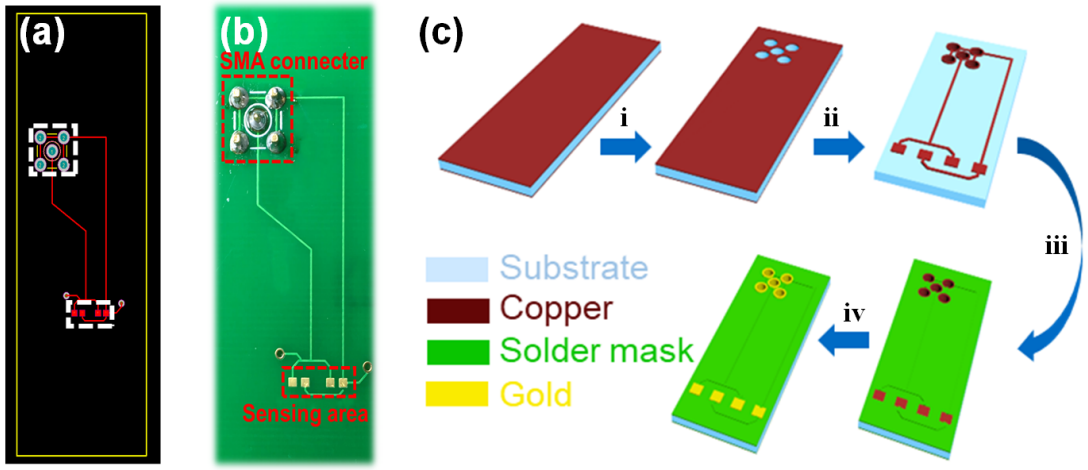

Figure 3.2: (a) The PCB layout and (b) the photography of the ion concentration sensor. (c) The scheme of the fabrication process for a typical sensor.

The self-powered sensing system is based on the concept of impedance matching effect of TENG and a capacitance-type ion concentration sensor is fabricated for demonstration. The design of the sensor is depicted as Fig. 3.2a. The fabrication, which was also based on the PCB technology, started from a circuit board substrate cladded by copper. (i) The next step was the drilling of holes in the substrate for Sub-Miniature-A (SMA) connector. (ii) Then, the entire surface, including the inside of the holes, of the circuit board was metalized. Proper photolithography process was carried out to pattern the circuit board. The conducting lines and sensing pads were formed. (iii) Afterwards, the surface of the circuit board was covered by solder mask lacquer for insulation. Only holes and sensing areas were exposed. (iv) The last step was gold immersion to deposit a gold thin film on the surface of sensing pads. The simplified fabrication flow is illustrated as Fig. 3.2c.

3.2 Mechanism

3.2.1 Working mechanism of RD-TENG

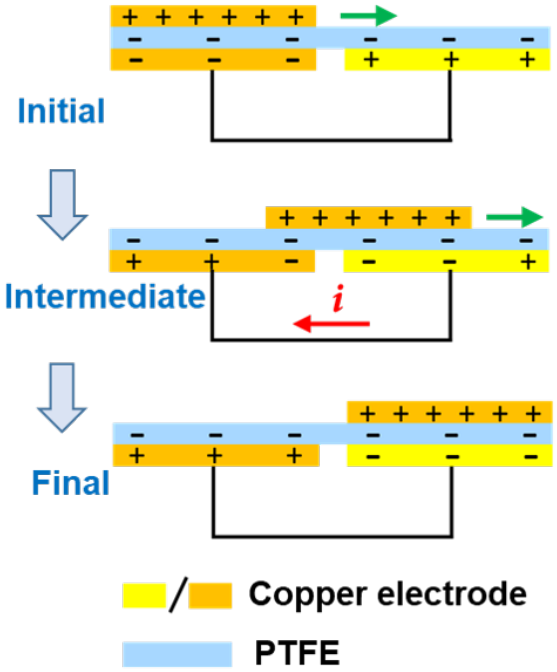

Figure 3.3: Illustration of working mechanism of the RD-TENG. One section of the disc is selected to display the charge distribution during the spinning of the rotator.

A typical RD-TENG is usually employed as a high-efficiency energy harvester to collect continuous flow or wind energy. The operation of the RD-TENG is based on the conjugation of triboelectrification and electrostatic induction [95–97]. During the operation, the rotator and stator are aligned coaxially to ensure the sufficient contacting. After sufficient triboelectrification between the top electrode and the PTFE film, the top electrode is positively charged while the PTFE is negatively charged due to the different capability of gaining/losing electrons. In the initial state, the positively charged top electrode is coaxially lined up with the bottom left electrode and induces the accumulation of electrons in the bottom left electrode. Since the law of charge conversation, the bottom right electrode is positively charged (equal to the left one).

Because of the unequal contact areas of top and bottom electrodes, the surface charge density of the rotator is twice as that of the stator. As the rotation, top electrode slides from left to right. In the intermediate state, the electrons on bottom electrodes redistribute with the top electrode, leading to a current flow from bottom right to bottom left. In the final state, the top electrode is aligned with the bottom right electrode and the electron distribution of bottom electrodes is opposite to the initial state. In next working cycle, another current flow is generated in inverse direction due to the interdigitated structure of bottom electrodes.

Fig. 3.3 demonstrates the charge distribution of the RD-TENG in short-circuit condition for one section in a half cycle. Under continuous rotation, the current and the inverse current are generated successively and periodically. Consequently, an AC power is generated, which has a frequency (f) as

$$f = \frac{3\gamma}{\delta_0} \tag{3.1}$$

where γ is the rotation speed (rpm) of the disc and δ_0 is the center angle (°) of a single rotator section. Herein, δ_0 for the RD-TENG is 1.5°.

3.2.2 Sensing mechanism

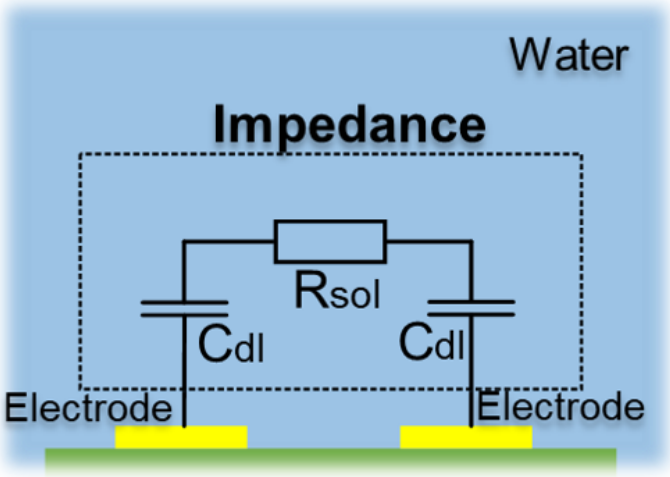

Figure 3.4: Working mechanism of the sensor in water.

The sensing mechanism of the ion concentration sensor can be explained by the impedance variation in the water between electrodes under different ion concentration. Since the real situation is very complicated, a simplified equivalent circuit (shown in fig. 3.4) is built to demonstrate the working mechanism. When the sensor is connected with an external source and immersed into the water, an electrical double-layer capacitor is formed near the surface of the electrode. Therefore, the total impedance (Z_{tot}) between electrodes can be approximately defined as:

$$Z_{tot} = R_{sol} + 2X_{cdl} \tag{3.2}$$

where R_{sol} is the bulk resistance of the water and X_{cdl} is the capacitive reactance contributed by the electrical double-layer capacitance near the electrode surface. Here, each electrode has two sensing pads connected in parallel for increasing the sensing area (Fig. 3.2b). Both R_{sol} and X_{cdl} are dependent on the ion concentration in the water. When the ion concentration changes

in the water, the impedance of the sensor will change accordingly.

3.3 Results and discussions

3.3.1 Electrical characterizations of RD-TENG

- Open-circuit voltage (V_{OC}) and short-circuit current (I_{SC})

The electrical output of the RD-TENG, driven by a programmable motor, was measured by a source meter (Keithley 6514). The source meter was connected to a laptop through a data acquisition card (National Instruments, BNC-2110) and a customized data acquisition system based on Labview platform was used to collect the voltage and current signals.

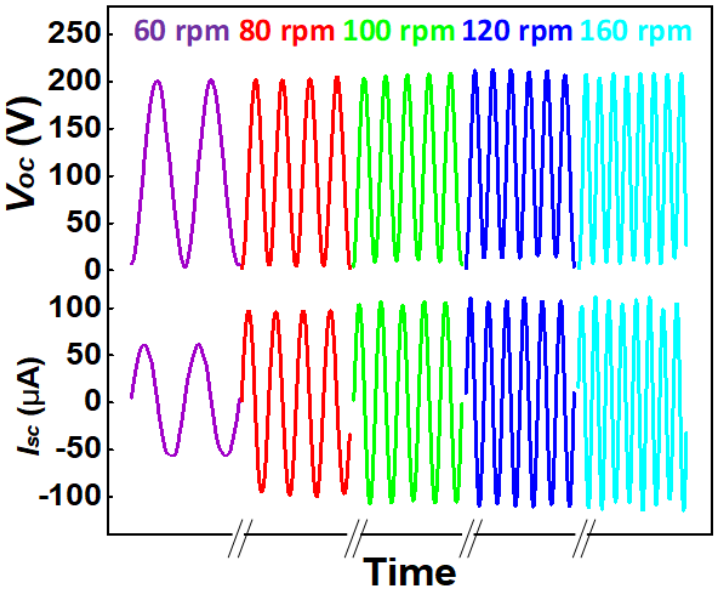

Figure 3.5: Open-circuit voltage (V_{OC}) and short-circuit current (I_{SC}) of the RD-TENG at different rotation speeds.

Fig. 3.5 shows the rotation speed dependence of the electrical output performance. Under the rotation speeds of 60, 80, 100, 120 and 160 rpm, the open-circuit voltage (V_{OC}) of the

RD-TENG almost keeps consistently same and the peak-to-peak value is ~210 V. However, the short-circuit current (I_{SC}) shows a direct proportional dependence on the rotation speed. At the rotation speed of 60 rpm, the I_{SC} is ~62 μA. The value approaches the maximum (~112 μA) at the rotation speed of 120 rpm and almost keeps constant even the rotation speed further increases. This rotation speed dependence can be theoretically explained according to the previous study [95, 98]. The peak V_{OC} can be defined as

$$V_{OC} = \frac{4d \cdot \sigma_0}{\varepsilon_0 \varepsilon_r} \tag{3.3}$$

where d is the thickness of the PTFE thin film, σ_0 is the surface charge density of PTFE, and ε_r is the relative dielectric constant of PTFE.

The peak I_{SC} is defined as

$$I_{SC} = \omega N \sigma_0 (r_2^2 - r_1^2) \tag{3.4}$$

where ω is the angular frequency of the rotator, N is the number of the sections, r_1 and r_2 are the inner and outer radii of the RD-TENG. Obviously, the angular frequency is related to the rotation speed. However, it is noticed that the peak I_{SC} is not linear with the rotation speed and almost saturates when the rotation speed larger than 100 rpm in Fig. 3.5. It is because we assume the rotator and the stator always keep contacted tightly and perfectly for Eq. 3.4. In reality, the flatness of the contact surfaces has a significant effect on the output current. Further, the rotator starts to jitter and tends to separate at high rotation speed because the experimental platform is not perfectly parallel to the ground. As a result, the I_{SC} does not follow the Eq. 3.4 and tends to saturate at high speed.

- Output of the RD-TENG with load resistance and capacitance

A load resistor and a load capacitor were connected with RD-TENG in series, respectively. The output voltage of the RD-TENG with different load resistance and capacitance was measured by the source meter.

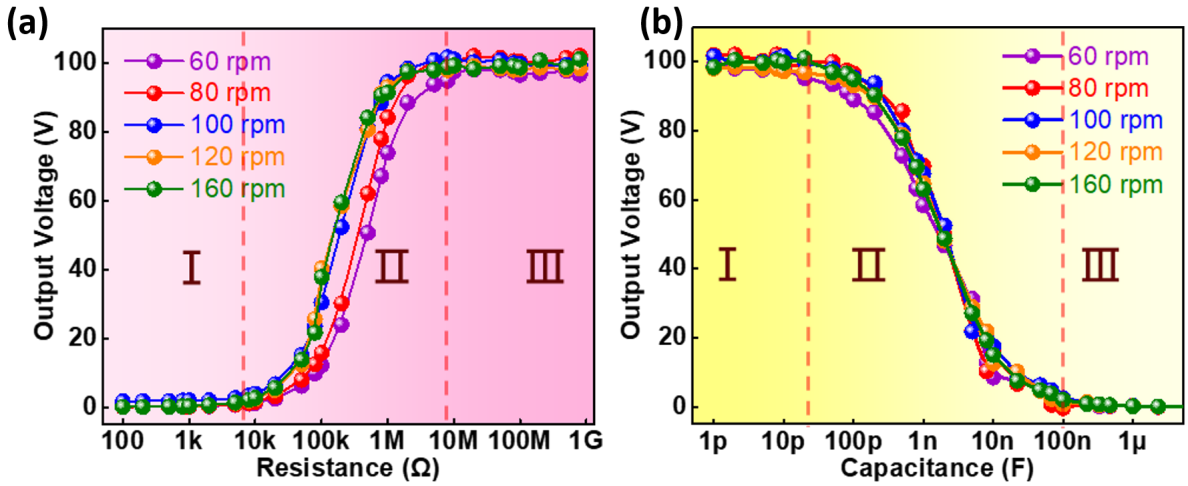

Figure 3.6: Relationship between the output voltage and (a) load resistance or (b) load capacitance at different rotation speeds.Three working regions can be defined and marked as Zone I, II and III, respectively.

From Fig. 3.6, it is clearly seen that three typical working regions can be divided for both figures, which can be marked as Zone I, II and III, respectively. As shown in Fig. 3.6a, when the load resistance is less than 10 kΩ, the voltage loaded on the external resistor approaches zero and a quasi-short-circuit condition is considered (Zone I). When the load resistance is larger than 10 MΩ, most open-circuit voltage is loaded on the external resistor and a quasi-open-circuit condition is considered (Zone III). Within the range of 10 kΩ~10 MΩ, the output voltage increases from minimum to maximum value rapidly (Zone II). Similarly, the output voltage dependence on external capacitance can also be explained by this limit approximation method, as shown in Fig. 3.6b. It drops dramatically when the load capacitance increases from 20 pF to 100 nF. Therefore, the sensing range typically locates in the Zone II for better

sensitivity. Furthermore, it can also be observed that the output voltage of the RD-TENG with load resistance is dependent on the rotation speed, where higher rotation speed gives a faster increase of output voltage. On the contrary, the output voltage of the RD-TENG with load capacitance is almost independent on the rotation speed. This can be explained by the Ohm's law and the impedance matching effect. In theory, the RD-TENG can be considered as a serial connection of a time-varying capacitor and an ideal voltage source (V_{OC}) [41]. With the peak output voltage, the instantaneous inherent impedance (Z_{in}) of the RD-TENG can be expressed as

$$Z_{in} = \frac{1}{2\pi f C_T} \tag{3.5}$$

where f is the frequency of the AC signal (corresponding to rotation speed) and C_T is the instantaneous capacitance of the RD-TENG when the output voltage has the peak value. When there is only load resistance (R) in the external circuit, the load impedance (Z_R) is

$$Z_R = R \tag{3.6}$$

On the contrary, there is no resistance term in the circuit when only load capacitance (C_L) is connected with the RD-TENG. The load impedance (Z_C) is defined as

$$Z_C = \frac{1}{2\pi f C_L} \tag{3.7}$$

Combining Eq. 3.5, 3.6 and 3.7, we can obtain the peak output voltage of the RD-TENG with load resistance and load capacitance:

$$V_R = \frac{Z_R}{Z_{in} + Z_R} \cdot V_{OC} = \frac{R}{\frac{1}{2\pi f C_T} + R} \cdot V_{OC} \tag{3.8}$$

$$V_C = \frac{Z_C}{Z_{in} + Z_C} \cdot V_{OC} = \frac{\frac{1}{C_L}}{\frac{1}{C_T} + \frac{1}{C_L}} \cdot V_{OC} \tag{3.9}$$

Based on these two expressions, it is apparent that the peak output voltage of the RD-TENG with load resistance is dependent on the frequency, or rotation speed. Higher frequency results in a higher peak output voltage. However, the peak output voltage of the RD-TENG with load capacitance is independent on the frequency.

3.3.2 Electrical characterizations of the sensor

The sensing mechanism of the ion concentration is based on the impedance matching between the sensor and TENG. To characterize the sensing performance, the sensor was immersed into the aqueous solution with different ion concentrations and the impedance of the sensor was measured by the impedance analyzer (WK, 6500B).

0.1 mol/L NaCl, Na_2SO_4, $CaCl_2$, $CuCl_2$ and $FeCl_3$ solutions were prepared in advance. Initially, the sensor was connected with the impedance analyzer with a coaxial cable. A beaker filled with ultra-pure water (150 mL) was positioned on a magnetic stirrer for accelerating the mixing and the sensing area of the sensor was immersed into the ultra-pure water. The prepared ion solution was added into the ultra-pure water drop by drop (15 μL). A low-level AC driving signal was applied to the sensor, resistance, capacitance and impedance were directly read from the impedance analyzer in real time.

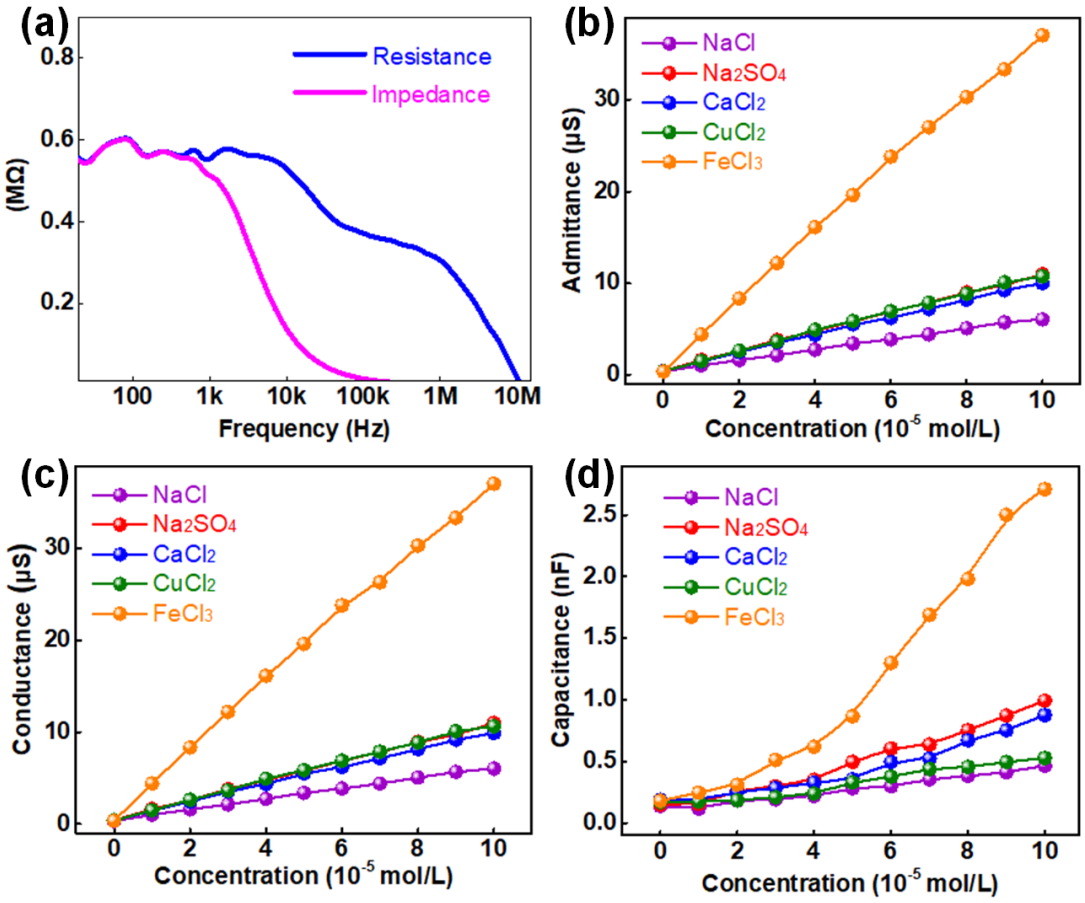

Figure 3.7: (a) Frequency sweep of resistance and impedance for the sensor in the NaCl solution with 2×10^{-5} mol/L concentration. Ion concentration dependence of (b) the admittance, (c) the conductance and (d) the capacitance under 200 Hz AC signal drive.

After adding two droplets of prepared NaCl solution in the ultra-pure water, correspondingly 2×10^{-5} mol/L, frequency sweep of resistance and impedance were performed from 20 Hz to 10 MHz, as depicted in Fig. 3.7a. The values of impedance and resistance are almost consistent until the frequency reaches 500 Hz, corresponding rotation speed of 250 rpm for the RD-TENG. Ideally, the impedance amplitude should approach infinitely large for f→0. However, both the impedance and the resistance tend to be constant for low frequency in Fig. 3.7a. This may attribute to the experimental setup. Both the impedance and the resistance of the sensor are highly dependent on the movement of the mobile ions (or charges) in the water

[99, 100]. To simulate the real situation, a magnetic stirrer was used to keep the water stirred. Therefore, the mobile ions in the water were initially moving between electrodes. At high frequency, this effect on the impedance is insignificant. But, at low frequency, the measured impedance is much lower than the ideal value due to the initial movement of ions. It is also observed that the value of the impedance falls rapidly while the value of the resistance falls much more slowly, because the capacitive reactance contributes very little to the impedance at low frequency (lower than 500 Hz). Numerically, the impedance of the sensor is approximately equal to the resistance. Additionally, the relatively flat impedance curve in this frequency range also indicates the purely resistive property of the sensor. When the frequency is higher than 500 Hz but lower than 10 MHz, the capacitive reactance cannot be ignored and the impedance and the resistance divaricate. When the frequency is higher than 10 MHz, the impedance nearly approaches zero because the capacitive reactance dominates the impedance. In the case of this RD-TENG, the generated AC power always has a frequency below 500 Hz. In consequence, we can ignore the concept of impedance and use only resistance instead in the following discussions for simplification even though there are reactance components in the circuit.

For further verification, the admittance, conductance and capacitance of the sensor, immersed in the water, were measured under the frequency of 200 Hz as the ion concentration increases (depicted in Fig. 3.7b, c and d, respectively). It is noticed that the admittance curves are highly consistent to the conductance curves. The comparisons between the admittance and the conductance under 200 Hz AC signal for NaCl, Na_2SO_4, $CaCl_2$, $CuCl_2$ and $FeCl_3$ are shown in Fig. 3.8b and c. Among these, the curves of admittance and conductance almost overlapped. Linearity of the curves is also shown in Fig. 3.7b and c. This can be explained by the concentration dependence of the compound's conductivity in dilute solution. The conductance of the water is determined by the total mobile ion (positive plus negative) concentration and valence.

(It is assumed that all compounds completely dissolve in the water at these low concentrations.) According to Kohlrausch's law [101], the conductivity of the highly dilute solution can be simply calculated as the compound's molar conductivity multiply the concentration of the compound. Table 3.1 gives the theoretical molar conductivity of different compounds in infinitely dilute solution.

Table 3.1: Theoretical molar conductivity of different compounds in dilute solutions.

Compound	Molar conductivity ($S \cdot cm^2 \cdot mol^{-1}$)
NaCl	126.45
Na_2SO_4	260.26
$CaCl_2$	271.68
$CuCl_2$	259.88
$FeCl_3$	433.02

In our experiments, the measured value is the conductance of the sensor. So, the slope of the conductance curve shows the relationship between the conductance of the sensor (not the electrolyte solution) and the concentration of different compounds. Not only the solution, but also the sensor itself contributes to the measured conductance. We cannot calculate the molar conductivity of the compound in solution and cannot directly compare the molar conductivity from Table 3.1 and the slopes of the curves in Fig. 3.7c either. However, the measured slopes of different curves perfectly reflect the similar variation trend as the theoretical molar conductivity for different compounds. Therefore, our measurements sufficiently prove the hypothesis that we can only consider resistance when constructing alarming system in the following section.

The capacitance generally increases with the compound concentration. It is because the dielectric constant of the water increases with the ion concentration [102]. Relative capacitances for different compounds attribute to the different total mobile charge concentration. The

higher the charge concentration is, the higher the dielectric constant will be, further resulting in a higher capacitance.

Moreover, the resistance of the sensor in ultra-pure water is ~3 MΩ, so that the dynamic sensing range of the ion sensor can be roughly considered as ~3 MΩ. Apparently, it can be fully overlapped by the Zone II of the RD-TENG (~10 MΩ). By properly designing the structure of TENG, the dynamic sensing range of the sensor can always be located in the Zone II (Fig. 3.6a). With tiny change of resistance, the output voltage of the RD-TENG will dramatically change, inducing an extremely high sensitivity.

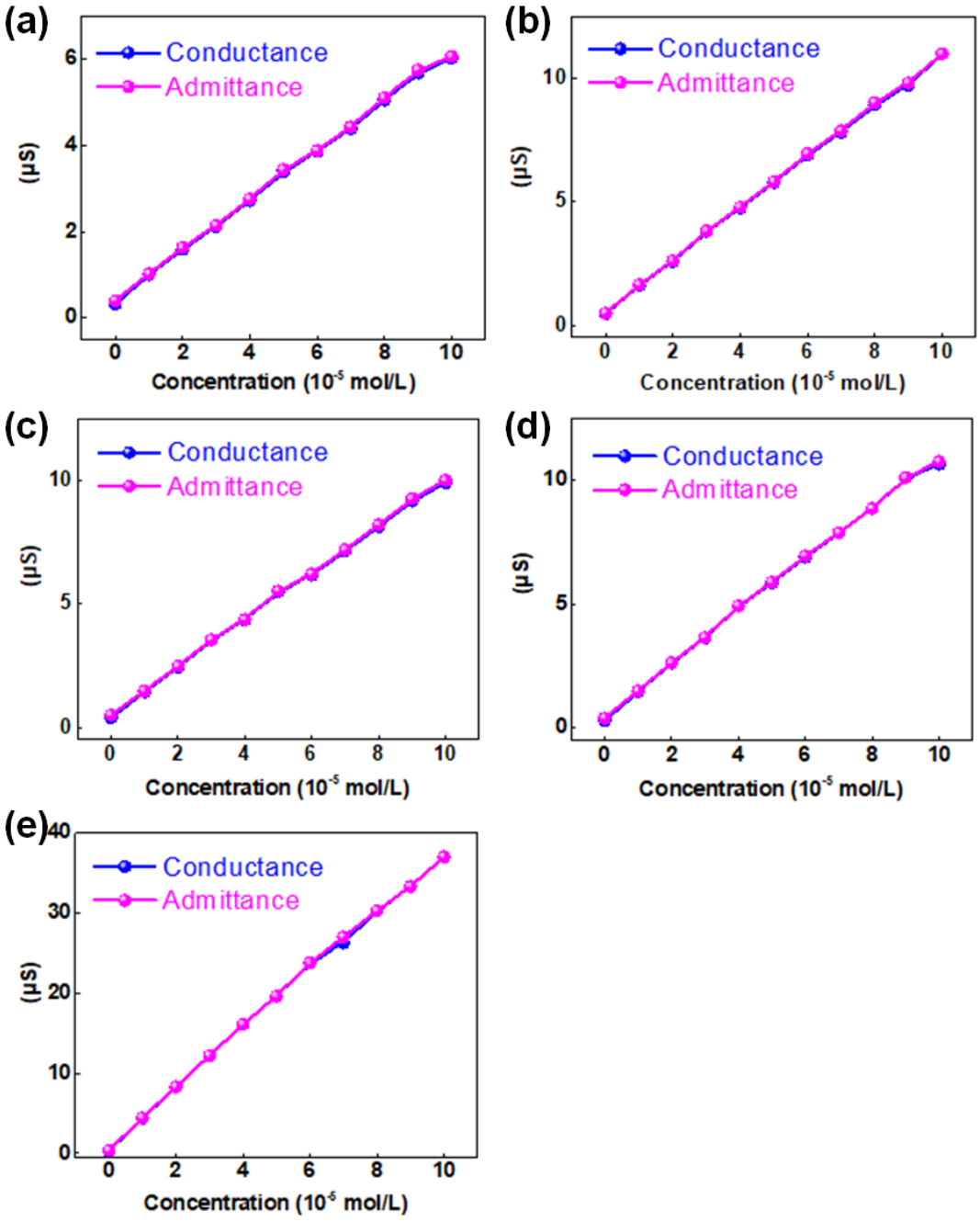

Figure 3.8: The concentration dependence of conductance and admittance for (a) NaCl, (b) Na_2SO_4, (c) $CaCl_2$, (d) $CuCl_2$ and (e) $FeCl_3$ solution under 200 Hz AC signal drive.

3.3.3 Sensing performance

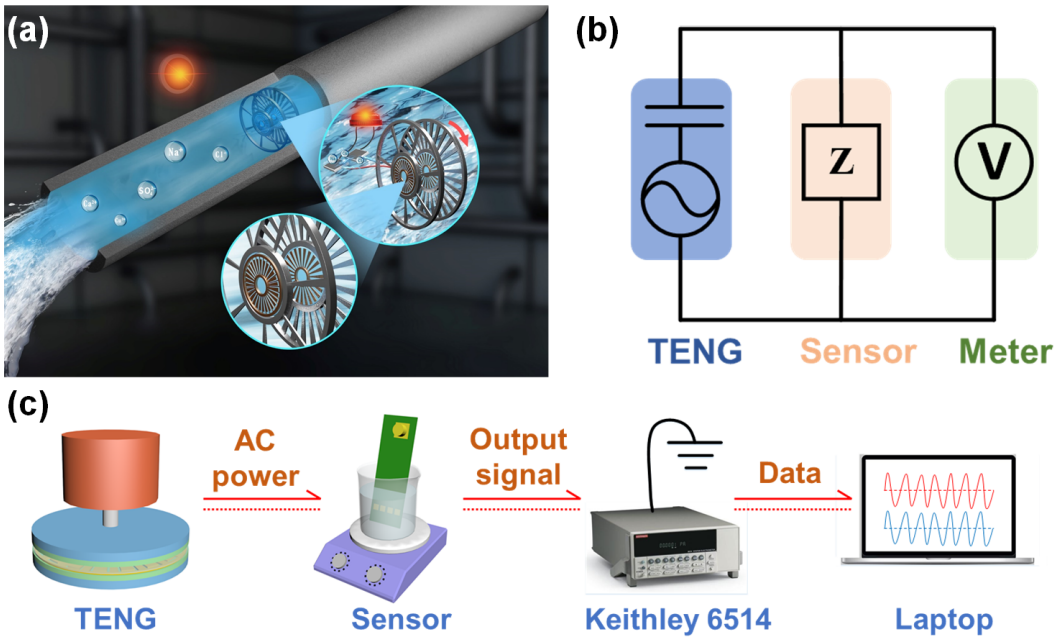

Figure 3.9: (a) Schematic illustration of the self-powered sensing system. (b) The equivalent circuit and (c) the schematic diagram of the experimental setup for the electrical measurements of the self-powered sensing system.

Based on the above results, we proposed a TENG driven self-powered on-line monitoring system in the pipeline transportation of water, as illustrated in Fig. 3.9a. In this system, a packaged RD-TENG is attached to a turbo fan, driven by flowing water in pipeline. Then the ion concentration sensor, immersed in the water, and an alarm component are connected in series with the RD-TENG to form a self-powered sensing system, which enables to convert mechanical energy of the flowing water into electricity and power the ion concentration sensor and alarm. When the ion concentration in the water pipeline has a tiny increase, the alarm will respond immediately.

Fig. 3.9b and c illustrate the equivalent circuit and the schematic diagram of the experimental setup for the electric measurements of the self-powered sensing system. A source meter

was connected in parallel with the sensor to measure the output voltage of the RD-TENG under the rotation speed of 100 rpm.

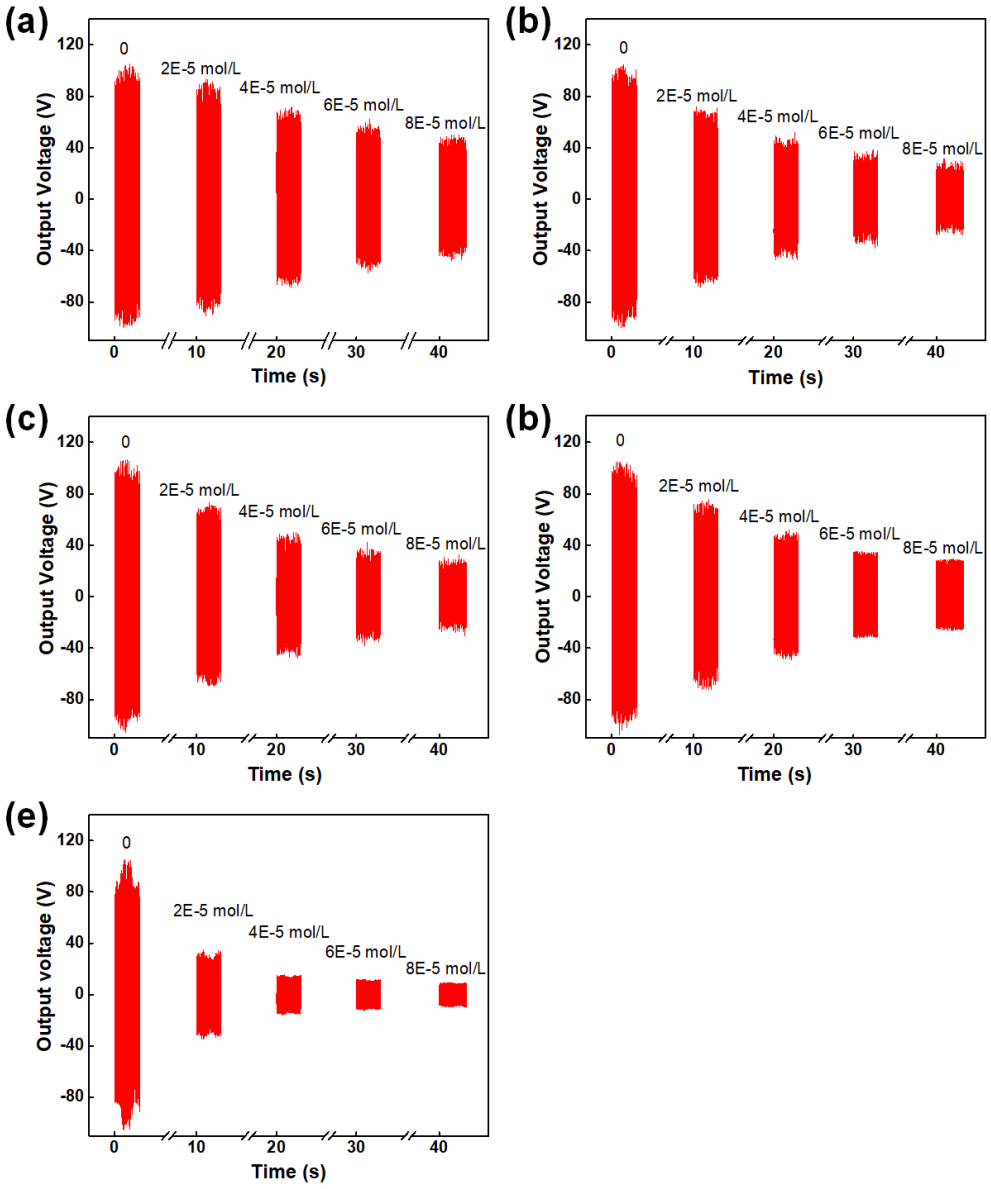

Figure 3.10: Real-time output voltage on the ion concentration sensor when the sensor immersed in the water with different ion concentrations for (a) NaCl, (b) Na_2SO_4, (c) $CaCl_2$, (d) $CuCl_2$ and (e) $FeCl_3$.

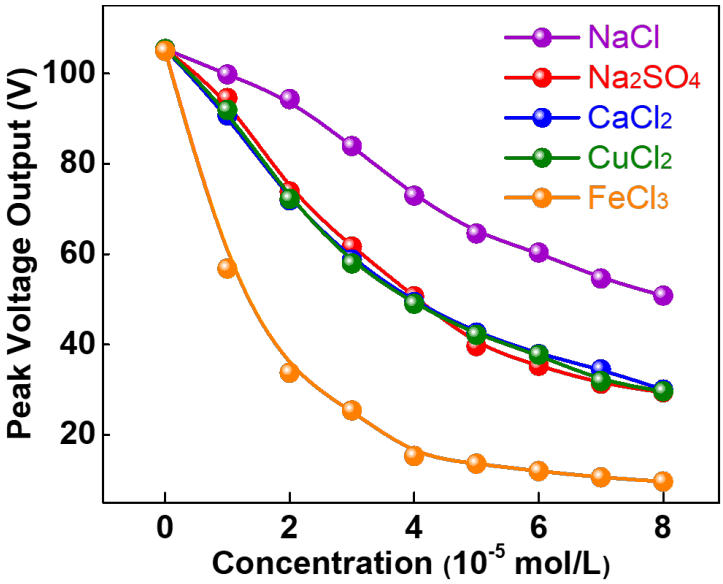

Figure 3.11: Ion concentration dependence of the peak output voltage for different aqueous solutions.

To study the ion concentration dependence of the peak output voltage for different compounds, five different prepared solutions (NaCl, Na_2SO_4, $CaCl_2$, $CuCl_2$ and $FeCl_3$, 0.1 mol/L) were respectively added into the ultra-pure water (150 mL) drop by drop (15 μL per drop), to obtain different ion concentrations. Since the output of TENG is peak output, we only took the positive peak output voltages in the calculation for convenience. For each measurement, we started to collect data when the output signal was stabilized. The duration of each data collection is usually 2~3 s so that we can actually get thousands of signals for each measurement. Fig. 3.10 shows the real-time output voltage on the ion concentration sensor when the sensor immersed in the water with different concentrations for NaCl, Na_2SO_4, $CaCl_2$, $CuCl_2$ and $FeCl_3$. For further analysis, we extracted a period of 200 ms from each measurement and calculated the root mean square of all positive peak voltages as the peak output voltage (V). Then, we plotted peak output voltage *vs*. concentration for different compounds (shown in Fig. 3.11). The peak output voltage suggests an inversely proportional relation with the ion concen-

tration. Among all these five curves, the output voltage starts from ~105 V, which corresponds to the V_{OC} of the RD-TENG. The NaCl curve is most linear and falls most slowly while the $FeCl_3$ curve is most non-linear and falls fastest. Na_2SO_4, $CaCl_2$ and $CuCl_2$ curves are between the NaCl curve and the $FeCl_3$ curve. In addition, these three curves are highly overlapped, which can be explained by the conductance curves in Fig. 3.7c. Back to Eq. 3.8, we assume $R = \frac{1}{kc}$, where k is a factor related to the total concentration of the mobile charges and c is the concentration of the compound. Eq. 3.8 can be rewritten as

$$V_R = \frac{1}{Z_{in} \cdot kc + 1} \cdot V_{OC} \tag{3.10}$$

Obviously, factor k contributes to the shape of the output voltage curve. Based on Eq. 3.10, the smaller the k is, the more linear the curve will be. Here, the NaCl curve almost shows a linear relationship between the peak output voltage and NaCl concentration in the measured range (0~8×10^{-5} mol/L).

To determine the limit of detection (LOD) of NaCl, $(V_{OC} - V)/V_{OC}$ *vs.* concentration was plotted by extracting data from Fig. 3.11. After linear fitting, the relationship (shown in Fig.3.12) between $(V_{OC} - V)/V_{OC}$ and concentration (c) is

$$(V_{OC} - V)/V_{OC} = 6976.50891[L/mol] \cdot c - 0.0029 \tag{3.11}$$

Refer to [103], LOD of $(V_{OC} - V)/V_{OC}$ is defined as

$$LOD = \gamma_B + 3s_B \tag{3.12}$$

where γ_B is the blank signal and s_B is the standard deviation of the blank signal.

The peak output voltage without NaCl is converted to $(V_{OC} - V)/V_{OC}$ as blank signal. A period of 200 ms from the measurement, where there is no NaCl in water, is extracted from Fig. 3.10a. The standard deviation of all positive peak voltages are calculated as s_B. Here, the standard deviation is defined as

$$s_B = \sqrt{\frac{1}{N}\sum_{i=1}^{N}(V_i - \mu)^2} \tag{3.13}$$

where N is the number of peak voltages, V_i is the peak voltage and μ is the mean of peak voltages. Based on the experimental data, γ_B and s_B are 0 and 0.0353, respectively. Back to the fitting Eq. 3.11, the calculated LOD of NaCl is 1.52×10^{-5} mol/L.

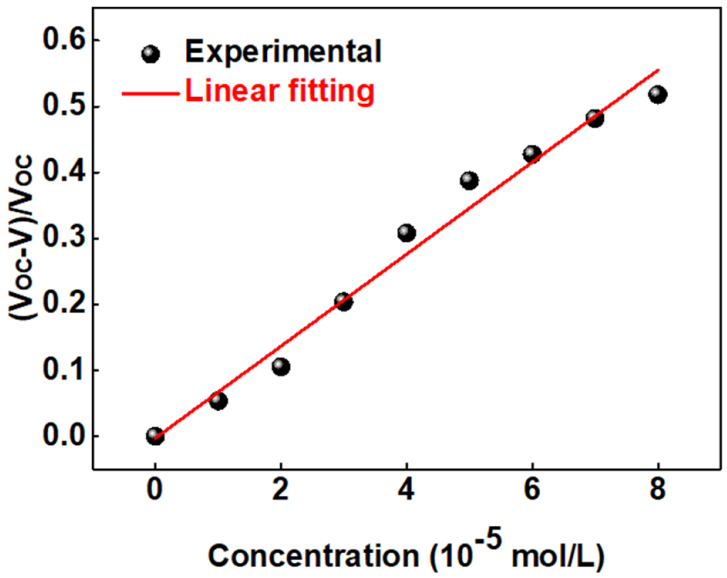

Figure 3.12: Linear relationship between $(V_{OC} - V)/V_{OC}$ and NaCl concentration.

Fig. 3.13 shows the ion concentration dependence of the peak output voltage for NaCl aqueous solution with different rotation speeds. It is observed that the peak output voltage linearity improves with the increase of the rotation speed. From Eq. 3.8, the peak output voltage of the RD-TENG is related to the rotation speed. As the rotation speed increases, the peak output voltage will also increase. When the rotation speed exceeds 100 rpm, the

rotator and the stator tend to separate and make the system unpredictable. Both the current and the inherent impedance of the RD-TENG tends to saturate. As a result, the improvement of the linearity of curves also tends to saturate. Although the rotation speed, correspondingly flowing speed of the water in pipeline, has a significant effect on the output voltage of the RD-TENG, the system can still achieve the sensing function. Furthermore, lower rotation speed will improve the sensitivity of the sensing system.

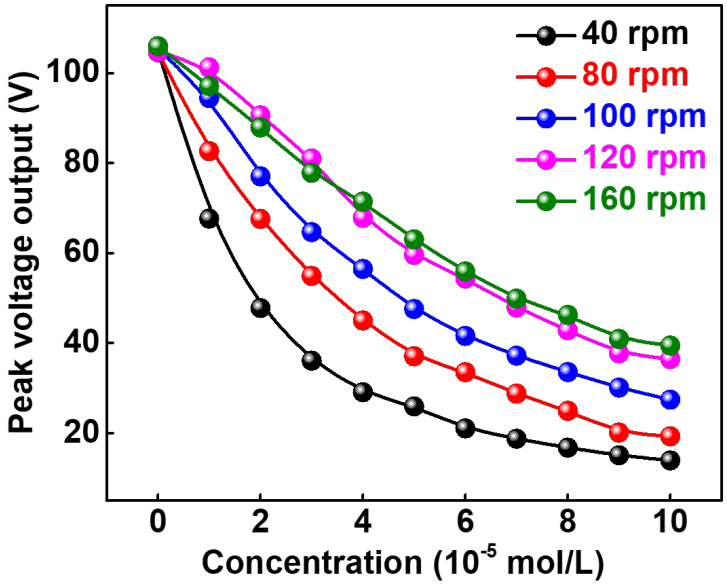

Figure 3.13: The ion concentration dependence of the peak output voltage for NaCl aqueous solution with different rotation speeds.

3.4 Demonstration of the self-powered ion concentration monitoring system

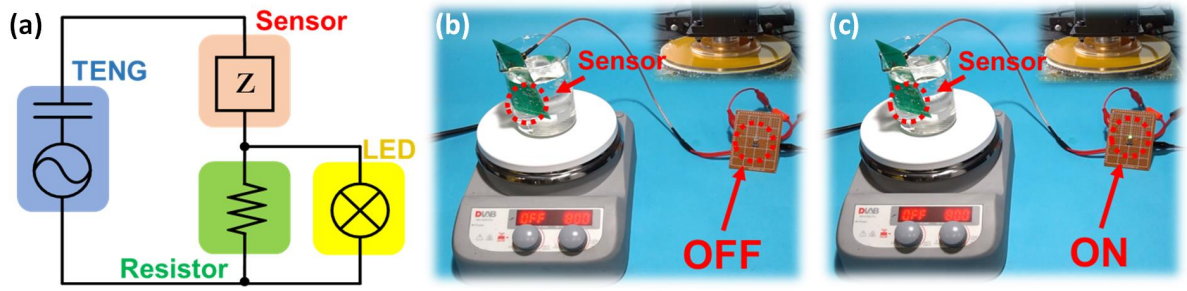

Figure 3.14: (a) The equivalent circuit for demonstrating the application of monitoring the water quality. Alarm LED is (b) OFF for the ultra-pure water, and (c) lighted(ON) with one droplet of 0.1 mol/L NaCl solution.

To bring the self-powered sensing system into practical application, a proper circuit was designed and a real self-powered sensing alarming system was built for demonstration, as shown in Fig. 3.14a. Herein, a beaker filled with 150 mL ultra-pure water was positioned on a magnetic stirrer. The stirrer was to accelerate the mixing of the ion solution. The sensing areas of the sensor were immersed into the water. The NaCl solution of 0.1 mol/L had been prepared in advance. A fixed resistor (150 kΩ) was connected in series with the sensor to control the output voltage of the RD-TENG. A commercial LED (threshold voltage: 1.4 V), in parallel connection with the fixed resistor, was used to realize the alarm function. To simulate the scenario that the turbo fans drive the RD-TENG, a programmable motor was utilized to actuate the rotator of the RD-TENG and control the rotation speed. The rotation speed was set to 100 rpm, corresponding to an AC power with frequency of 200 Hz. Initially, the LED is in the state of OFF, as shown in Fig. 3.14b. Then, one droplet of NaCl solution (15 μL) was added into the ultra-pure water and the LED was turned on instantly (shown in Fig. 3.14c).

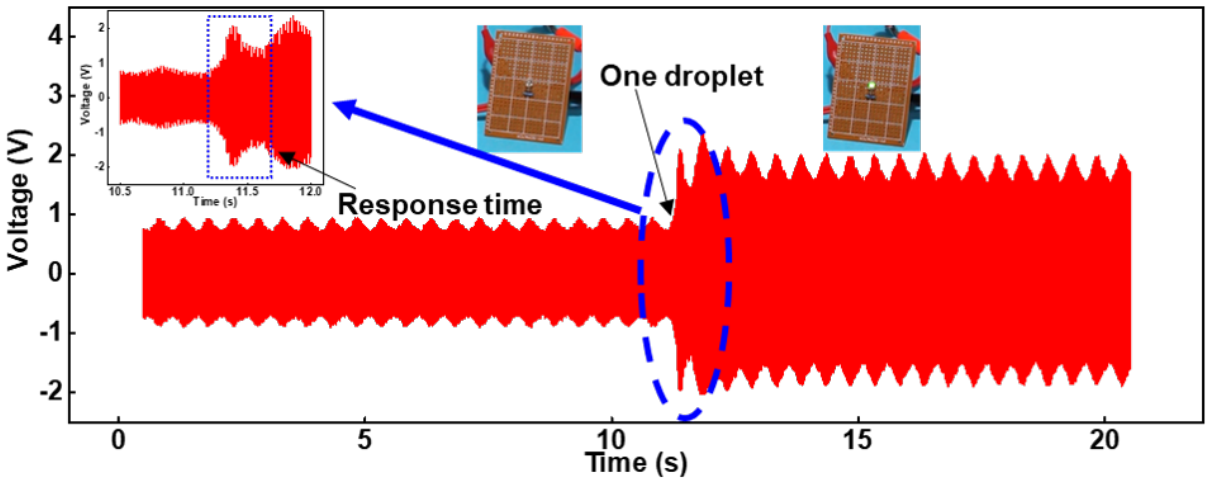

Figure 3.15: Real-time voltage response between the alarm LED during the experiment. Insert: response time of the sensing alarm system.

Fig. 3.15 shows the real-time voltage response of the LED during the experiment. We can clearly see that the peak voltage response of the LED increases from 0.9 V to 2 V instantaneously after one droplet of NaCl solution. The inserted figure is the enlarged view of the circled region. It is illustrated that the response time of the sensing system is in the scale of millisecond. It is also noticed of the periodic fluctuation of the voltage signal. Several factors may cause it. Both contact surfaces are not perfectly flat due to the patterned electrodes. So tiny jitter cannot be avoided during rotation. In addition, the variation of the thickness of the rotator/stator and experimental setups can also make the jitter worse. All these factors could result in the fluctuation of output voltage signal. Since the period of the fluctuation is within second, it will not affect the sensing function in reality.

As aforementioned, the capacitive reactance contributes very little to the variation of the impedance of the sensor at this low working frequency. Hence, change of the capacitive reactance with the ion concentration is not considered and all of the electrical components in the circuit are considered as pure resistance for this alarm system. When the ion concentration in-

creases in the water, the conductivity of the water increases, leading to a decrease of resistance between electrodes of sensor. The output voltage (V_{LED}) on the LED is defined as

$$V_{LED} = \frac{R_{fix}}{R_{fix} + R_{sensor}} V_0 \tag{3.14}$$

where R_{fix} is the resistance of the fixed resistor, R_{sensor} is the resistance of the sensor and V_0 is the output voltage of the RD-TENG with the load resistance of ($R_{fix} + R_{sensor}$). Although the output voltage of the RD-TENG decreases as the increase of the ion concentration in the water, the value is still much higher than the threshold voltage of a commercial LED. Therefore, the voltage on the LED still increases as the ion concentration increases in the water. Actually, the threshold of the output voltage can be adjusted by changing the fixed resistor for different requirements.

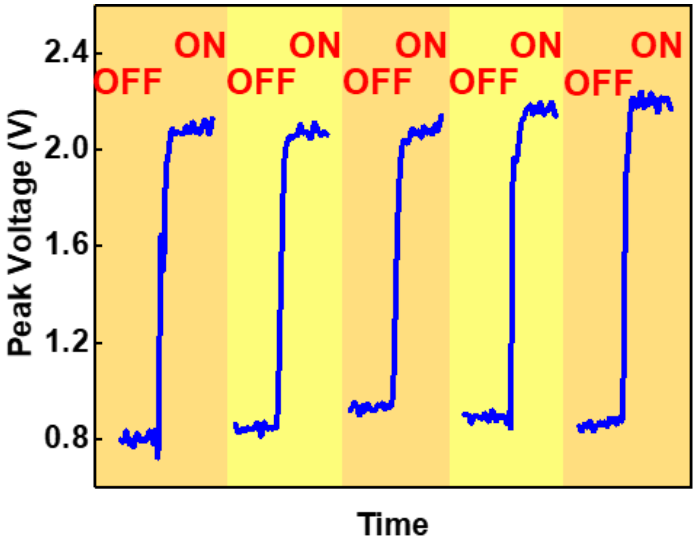

Figure 3.16: Reliability test of the sensing alarm system for 5 cycles.

To study the reliability of the self-powered sensing alarm system, we performed the alarming experiments for five times. After each cycle of experiment, we rinsed the ion concentration sensor and replaced the water in the beaker with fresh ultra-pure water. Then, we repeated

the experiment again. Every time, we measured the peak output voltage on the LED in real time. The peak voltage vs. time was plotted, as depicted in Fig. 3.16. It shows that the peak voltage on the LED is consistently lower than the threshold voltage (1.4 V) of the LED before the addition of NaCl solution, while the peak voltage on LED is always higher than the threshold voltage after the addition of NaCl solution. Hence, the self-powered sensing alarm system exhibits excellent reliability.

Table 3.2: Published self-powered sensing systems based on TENG.

Reference	Target	Sensing mechanism	Limit of detection	Sensitivity	Dynamic range
[48]	Dopamine		0.5 μM	N/A	10 μM to 1 mM
[104]	Phenol		N/A	$0.01\mu M^{-1}$	10 μM to 100 μM
[105]	Mercury	change of surface charge density	30 nM	N/A	100 nM to 5 mM
[106]	Cu; Pb; Cr		N/A	0.005e-6 M^{-1}; 0.003e-6 M^{-1}; 0.004e-6 M^{-1}	0 to 200 μM
[107, 108]	Ethanol		N/A	N/A	N/A

Published TENG-based self-powered sensing systems are listed in Table 3.2. It is observed that all published sensing systems are working under same mechanism. Before the measurement, triboelectric materials are immersed into the testing solutions. Targeting substances will adsorb to the triboelectric surfaces when the triboelectric materials are pulled out and dried. The adsorption of substances on the triboelectric surfaces changes the surface charge density after contact. Therefore, the output voltage/current changes with the concentration of the substances. Based on the reported data, TENG-based sensing systems can reach high sensitivity. However, the biggest issue is that the process is too complicated and this working mechanism can not realize real-time sensing. On the contrary, our proposed monitoring system can perfectly achieve real-time sensing. None of the published sensing systems gave the efficiency of TENG. A possible reason is that the output signal (typically voltage) is the most important parameter for sensing application. Currently, the output voltage of TENG-based sensors is high

enough for measurements. In terms of our RD-TENG, a very similar TENG structure has been reported for harvesting mechanical energy and an efficiency of ~24% can be achieved [95]. We can use this value as an estimation.

3.5 Chapter conclusion

In this chapter, the RD-TENG driven self-powered sensing system for on-line monitoring of ion concentration in water was proposed. This new sensing strategy can convert the mechanical energy from flowing water in pipeline to electrical energy and power a sensing alarm system, realizing high sensitivity, high reliability and low cost. Both RD-TENG and ion concentration sensor were designed and manufactured based on the industrial PCB technology. This fabrication method not only improves the output but also provides the possibility for TENG of mass production in industry. The output voltage of the RD-TENG shows an independence on rotation speed, where the open-circuit is 210 V_{P-P}. At the working rotation speed (100 rpm), the impedance of the sensor in the water could be simply considered as a pure resistance so that the sensing mechanism was much simplified. The real-time ion concentration sensing was based on the impedance matching between the RD-TENG and the ion concentration sensor. A demonstration of self-powered sensing alarm system was successfully presented and exhibited an excellent sensitivity (1.52×10^{-5} mol/L LOD for NaCl).

Improvements can still be taken to enhance the performance of the self-powered system, such as the interdigitated-electrode structure for higher sensitivity and proper coating of the electrodes for better selectivity. Furthermore, the study on the relationship between the output voltage and the load capacitance (Fig. 3.6b) reveals a new strategy for sensing application in the future. It is more practical and reliable to design self-powered sensing system based on the

capacitive impedance matching of TENG because the output is independent on the frequency of the mechanical movement. Less additional factors will affect the sensing output signal.

Chapter 4

Development of micro- triboelectric energy harvester

In the previous chapter, an example of TENG functioning as a power source for self-powered environmental monitoring is exhibited. Other than environmental monitoring, health monitoring is also an important application of energy harvesters. So far, a few studies have been conducted to harvest biomechanical energy for powering implanted devices based on flexible TENG [54, 61, 62]. All these reported TENGs are working under the vertical contact-separation mode, functioning as passive energy harvesters. Although they can directly harness the mechanical energy of organs inside the human body and have high output power (power density up to 0.84 $\mu W/cm^2$), they suffer from the limitation of implanted site, uncertain output power and poor IC integration. Compare to the passive energy harvesting approaches, active energy harvesting technologies can provide a controllable and reliable energy to implanted energy harvester inside the human body. Besides, the signal can even be modulated from the transmitting end, giving more flexibility in practical applications.

EI is currently the most mature technology to actively transfer energy and has been widely applied in wireless charging of cellphone and electric toothbrush. However, EI's output power is significantly affected by the metal coil, including the diameter and turns, resulting in a complex system structure. Other than the coil itself, the efficiency is extremely sensitive to the

alignment of two coils. Differently, AET has exhibited advantages of long-distance transmission, no interference with other electronics and flexible packaging material choices. Up till now, most reported AET systems are based on the bulk PZT transducers with sizes ranging from millimeters to centimeters [17, 109, 110]. Chip-sized integration is an important issue to be solved and it is limiting their further development.

Inspired by the high output of TENG, it is proposed to apply the TENG for the application of AET. Currently, most reported TENGs are handcrafted, leading to a critical issue that huge variations may occur between device to device. Even for two devices with the exactly same structure, the output of them may vary a lot due to some uncertainties during the fabrication. Moreover, the environment, such as humidity, could also have a significant effect on the output of a TENG. Typically, an increased humidity will lead to a dramatic decrease of the TENG's output. Another issue of the existing TENGs is the device size. Though "nano" in the name, the sizes of the reported TENGs never reach nanoscale, not even microscale. The vast majority of them are in the scale of centimeters. Some researchers mentioned their TENGs were based on MEMS technology [33–35, 111]. With micro-/nano- structures patterned on the surface of the triboelectric layers, the sizes of their actual devices are still large.

Aiming at solving the problems hereinbefore, a novel micro- triboelectric energy harvester (μTEH) was developed, which was designed and fabricated entirely based on MEMS technologies. The μTEH brings the size of TENG into the microscale for the very first time. This miniaturized TENG tremendously improves integration level. Furthermore, vacuum cavities were built between the triboelectric pair. The negative effect of the ambient environment is eliminated to the most extent. The features of accuracy, stability and repeatability will greatly promote the application of TENG into IoT in the future.

4.1 Working frequency of acoustic energy harvesting

In this work, the μTEH is potentially applied for biological applications. The selection of the working frequency is based on both the physical limitations and safety concerns.

- Acoustic attenuation

Ultrasonic wave encounters energy losses when traveling through media, which is so-called acoustic attenuation. Essentially, the combination of absorption and scattering is the main reason for acoustic attenuation. In real applications, it plays a non-negligible role. It acts as a measurement of how the ultrasonic intensity decays in the medium. Minimization of the acoustic attenuation is an important concern when selecting the working frequency. In the medium, acoustic attenuation can be modeled as

$$I_z = I_0 e^{-\alpha(f)z} \tag{4.1}$$

where I_z is the intensity of the ultrasonic wave at certain distance z, I_0 is the original intensity and $\alpha(f)$ is the attenuation coefficient of the acoustic wave in medium. $\alpha(f) = \alpha \cdot f^n$ is a frequency-dependent factor of ultrasonic wave in biological tissues. Herein, α=0.15 dBcm^{-1}MHz^{-1} is an average value of attenuation coefficient and n is assumed as unity in biological media [112]. From Eq. 4.1, the intensity of ultrasonic wave will exponentially decay when increasing the working frequency and the separation between the transmitter and the receiver.

- FDA standards

Inevitably, some side-effects may occur when the ultrasonic wave travels through human tissues. Thermal effect and cavitation are the two most prevailing ones. Nowadays, ultrasound

has been widely applied to diagnostic and therapeutic applications [113, 114] and regulations are set to minimize the side effects. Food and Drug Administration (FDA) has provided standards to limit the output power of ultrasound devices in diagnostic applications [115], which can be a reference. The spatial-peak temporal-average intensity (I_{SPTA}) for continuous-wave applications should be less than 720 mW/cm^2 and the spatial-peak pulse-average intensity (I_{SPPA}) for pulsed-wave applications should be less than 190 mW/cm^2. They correspond to the thermal damage and mechanical damage, respectively. To estimate the mechanical damage, mechanical index (MI) is often specified, which is defined as [116]

$$MI = \frac{p}{\sqrt{f_0}} \frac{\sqrt{1MHz}}{1MPa} \tag{4.2}$$

where p is the peak negative ultrasound pressure in MPa derated by 0.3 dBcm^{-1}MHz^{-1} and f_0 is the center frequency of ultrasonic wave in MHz. Recommended by FDA, the MI for the diagnostic systems should be less than 1.9. In other words, a higher center frequency is desired to decrease the mechanical damage.

According to the literature review [17, 18, 109, 117–120], frequencies between 500 kHz and 2 MHz should be suitable as a compromise between the attenuation and safety. Therefore, we choose 1 MHz as the working frequency in this work.

4.2 Working mechanism of the μTEH

Fig. 4.1 illustrates the basic structure and working mechanism of the μTEH, which has a diaphragm structure. It is working under the vertical contact-separation mode. Essentially, a fully clamped silicon membrane is suspended atop a vacuum cavity. The highly-doped silicon layer underneath the silicon oxide (triboelectric & insulating layer) acts as the bottom electrode.

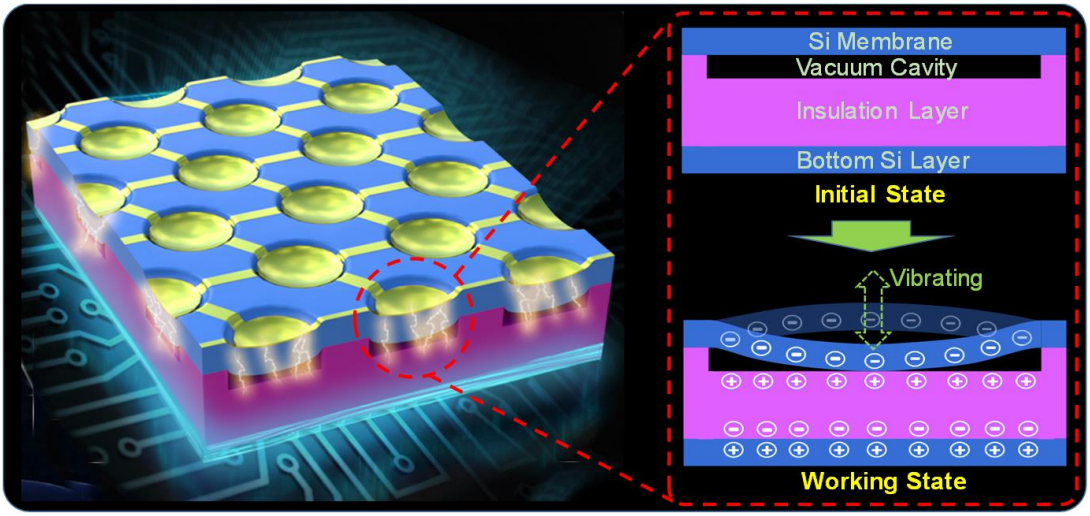

Figure 4.1: Basic structure and working mechanism of the μTEH.

Under the excitation of the incident acoustic wave, the suspended silicon membrane vibrates and hits the silicon oxide substrate. Then, the contact between the silicon and the silicon oxide causes charges redistributed because of the triboelectrification. Due to the opposite triboelectric properties, the silicon membrane is negatively charged while the top surface of the silicon oxide layer is positively charged. According to the conservation of charge and electrostatic induction, free electrons flow through the external circuit back and forth with the vibration of the membrane. Fig. 4.2 demonstrates the detailed working mechanism under the short-circuit condition in one working period. When this working period repeats, AC power is generated in the external circuit.

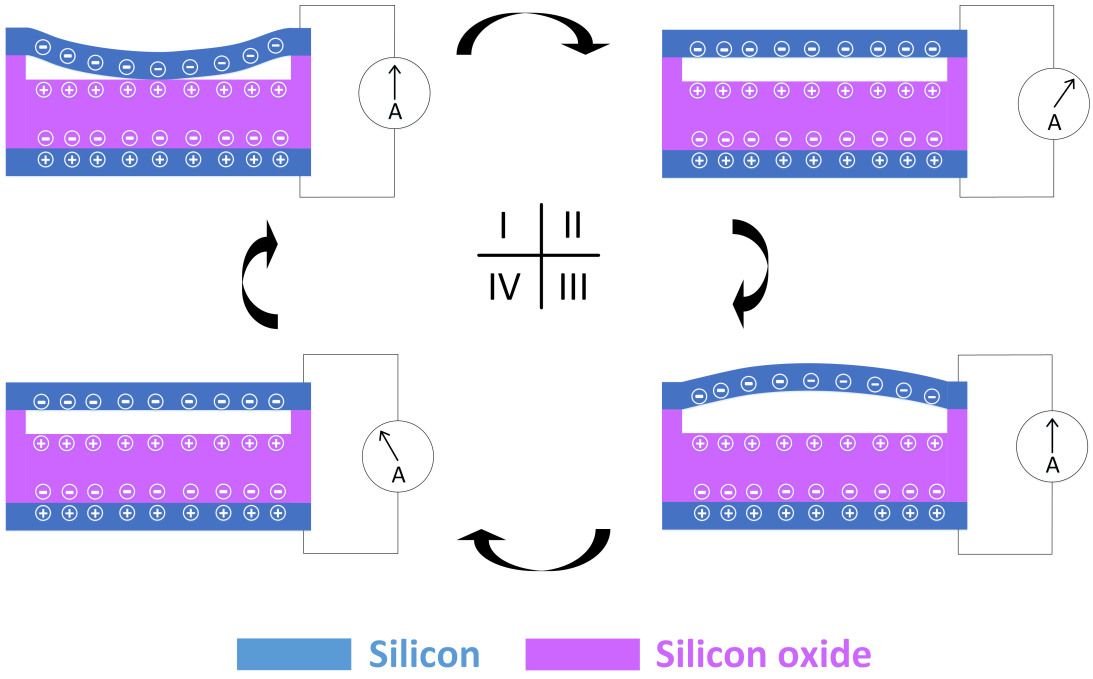

Figure 4.2: Illustration of detailed working mechanism of one single μTEH cell in one working cycle.

4.3 Design of the μTEH

For the diaphragm-structured μTEH, the maximum output should be achieved at the 1st mode resonance and the resonant frequency mainly depends on the membrane, including the structure, the material properties and the boundary conditions. In addition, the static displacement of the membrane induced by the atmospheric pressure should also be taken into consideration.

4.3.1 Resonant frequency

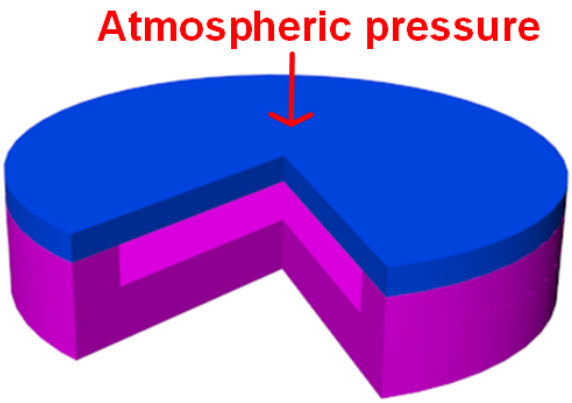

Figure 4.3: 3D structures of the μTEH.

A μTEH with the circular membrane was designed in this work. The 3D structure of the μTEH is depicted in Fig. 4.3. A portion is cut to show the inner structure more clearly. An analytical model was built to calculate the resonant frequency of the μTEH. Since degassed/deionized water has the similar acoustic properties to tissues (see Appendix C), the resonant frequency of the μTEH in water was analyzed. In the analytical calculation, an assumption was made that the effect of the top electrode was eliminated. It is because the thickness of the top electrode is much smaller (10 times smaller) than that of the silicon membrane. At the same time, the intrinsic stress of the membrane was also neglected because the intrinsic stress in the device layer of silicon-on-insulator (SOI) wafer is almost zero.

The 1st mode resonant frequency of the μTEH with a circular membrane in water is [121]

$$f = \frac{0.474\frac{hc_p}{R^2}}{(1 + 0.67\frac{\rho_w R}{\rho h})^{1/2}} \tag{4.3}$$

where

$$c_p = [\frac{E}{(1-\nu^2)\rho}]^{1/2} \tag{4.4}$$

R is the radius of the membrane, h is the thickness of the membrane, ρ is the volumetric density of the membrane material, E is the Young's modulus of the membrane material, ν is the Poisson's ratio of the membrane material and ρ_w is the density of water.

Particularly, the dynamics of the triboelectric effect may also be a concern when determining the working frequency. The question is if there is a frequency that the contact time is too short for charge transfer between two materials. So far, there has been no published paper talking about the charge transfer speed. Actually, quantitative study of triboelectrification is still an important research direction and there is no a conclusive model to fully explain this phenomenon now. Refer to a state-of-the-art study [122], the charge transfer process can be explained by electron-cloud-potential-well model. Electron clouds overlap when two materials contact with each other and electrons hop from one to another. Based on their explanations, this process should happen in the scale of light speed. Therefore, we assume working frequency of MHz is enough for the charge transfer process.

4.3.2 Static displacement under the atmospheric pressure

Other than the working frequency, cavity depth is another key point to design the μTEH. In reality, the membrane is naturally curved down to the substrate due to the atmospheric pressure outside the vacuum cavity. In the extreme case, the membrane will initially collapse if the cavity depth is too small. Then, the vibration of the membrane will be non-linear and be difficult to predict. In another extreme case, the membrane will not touch the substrate if the cavity depth is too large. Therefore, the cavity depth should be conscientiously chosen to avoid the abovementioned situations. To determine the cavity depth of the μTEH, the static displacement of the membranes under the atmospheric pressure should be calculated.

In the calculation, the load pressure is uniformly loaded on the entire top surface of the

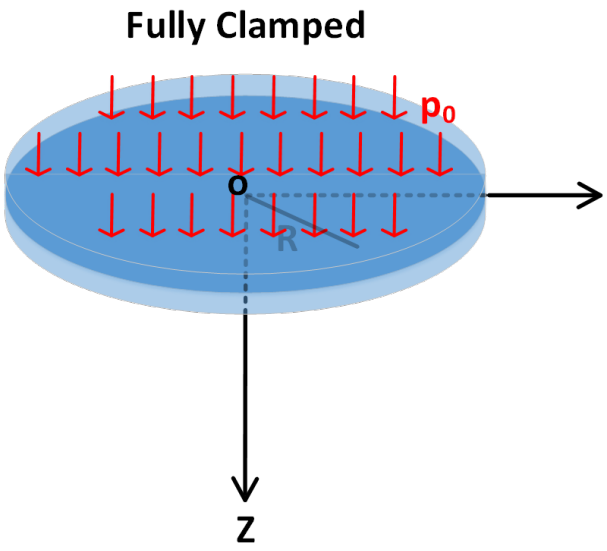

Figure 4.4: 3D model of circular membrane for analytical calculation.

membrane. Since the circular membrane is symmetrical about the z axis, the deflection surface is also axisymmetrical. Thus, Cylindrical coordinate system is more convenient for calculation. For clear expression, the positive direction of the z axis is downward, as shown in Fig. 4.4.

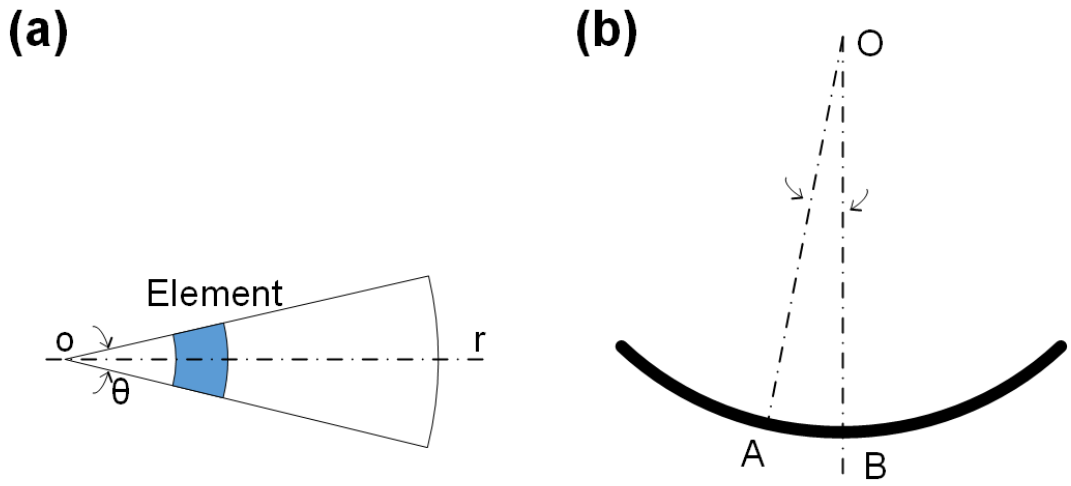

Figure 4.5: (a) The topview of one section of the circular membrane. (b) The cross-sectional view of the circular membrane. B is the center point of the membrane.

The circular membrane can be divided into an infinite number of small elements and the deflection surface of the membrane is the integration of all the elements. Taking one single element (the blue part in Fig. 4.5a), the moments along four edges are summed up and the

equation of equilibrium is obtained as

$$(M_r + \frac{dM_r}{dr}dr)(r + dr)d\theta - M_r r d\theta - M_t dr d\theta + Q_r d\theta dr = 0 \tag{4.5}$$

where M_r is the bending moment per unit length along circumferential sections of the membrane, M_t the bending moment per unit length along the diametral section rz of the membrane and Q_r the shearing force per unit length of the cylindrical section of radius r.

Derived from Kirchhoff–Love plate theory,

$$M_r = -D(\frac{d^2w}{dr^2} + \frac{\nu}{r}\frac{dw}{dr}) = D(\frac{d\varphi}{dr} + \frac{\nu}{r}\varphi) \tag{4.6}$$

$$M_t = -D(\frac{1}{r}\frac{dw}{dr} + \nu\frac{d^2w}{dr^2}) = D(\frac{\varphi}{r} + \nu\frac{d\varphi}{dr}) \tag{4.7}$$

where φ is the small angle between the normal to the small element at point A (corresponding to the blue part in Fig. 4.5a) and the axis OB, which is shown in Fig. 4.5b.

By eliminating small quantities of higher order, Eq. 4.5 can be simplified as

$$M_r + \frac{dM_r}{dr}r - M_t + Q_r = 0 \tag{4.8}$$

Substituting Eq. 4.6 and 4.7 into 4.8, we obtain

$$\frac{d}{dr}\left[\frac{1}{r}\frac{d}{dr}(r\frac{dw}{dr})\right] = \frac{Q}{D} \tag{4.9}$$

When the circular membrane is uniformly loaded by the atmospheric pressure (p_0), the shearing force (Q) at a distance (r) from the center of the membrane is defined as

$$2\pi rQ = \pi r^2 p_0 \tag{4.10}$$

Substituting into Eq. 4.9, we obtain

$$\frac{d}{dr}\left[\frac{1}{r}\frac{d}{dr}(r\frac{dw}{dr})\right] = \frac{p_0 r}{2D} \tag{4.11}$$

The integration of Eq. 4.11 gives

$$w = \frac{p_0 r^4}{64D} + \frac{C_1 r^2}{4} + C_2 log\frac{r}{a} + C_3 \tag{4.12}$$

where a is the radius of the membrane. For the circular membrane with fully clamped edge, the boundary conditions are

$$\begin{aligned} (w)_{r=a} &= 0 \\ (\frac{dw}{dr})_{r=0,a} &= 0 \end{aligned} \tag{4.13}$$

Applying these boundary conditions to Eq. 4.12, we obtain the values of coefficients

$$\begin{aligned} C_1 &= -\frac{p_0 a^2}{8D} \\ C_2 &= 0 \\ C_3 &= \frac{p_0 a^4}{D} \end{aligned} \tag{4.14}$$

Substituting these coefficients into Eq. 4.12, we find the deflection surface of the circular membrane under atmospheric pressure

$$w = \frac{p_0}{64D}(a^2 - r^2)^2 \tag{4.15}$$

4.4 Fabrication of the μTEH

4.4.1 Wafer bonding techniques

The most crucial structure of the μTEH is the vacuum cavity because the damping of the membrane on the backside can be dramatically decreased. In addition, the opposite surfaces of the triboelectric pair will not be affected by the ambient environment, resulting in a reliable output of the μTEH. However, building the vacuum cavity is a challenging work in the fabrication. In the field of MEMS, it is mainly realized by various wafer-to-wafer bonding techniques, such as fusion bonding, anodic bonding and adhesive bonding [123–125]. The anodic bonding technique is particularly for the bonding between Pyrex glass and silicon wafer [126–128]. It is not suitable for μTEH because it is difficult to control the etching of glass and the thickness of the dielectric layer. In terms of adhesive bonding, polymer adhesives should be involved, such as Benzocyclobutene (BCB) [129, 130], epoxies [131, 132] and polyimides [133, 134]. The addition of the adhesive layer makes the mechanical and the electrical behaviors of the membrane much more complicated and unpredictable. Contrarily, the fusion bonding technique is a more direct process to bond a pair of wafer together without the intermediate layer, where the most common bonding pairs are Si-Si and Si-SiOx [135–137]. The mechanism behind the fusion bonding is the formation of covalent bonds between the two surfaces of wafers. Compared to anodic bonding, more flexibility is given for the thickness of the dielectric layer.

To ensure the success of fusion bonding, both the wafer surfaces should be sufficiently cleaned and have a surface roughness (R_{rms}) less than 10 Å [125, 138–140]. Pristine SOI wafer and prime wafer from manufacturers are usually polished and precleaned, having a typical surface roughness (R_{rms}) less than 7 Å, which is fully satisfies the requirement of fusion bonding. Based on the triboelectric series, silicon and silicon oxide have the opposite capability

of gaining/losing electrons, which will be verified in the following section. The μTEH can be fabricated based on the silicon-silicon oxide fusion bonding technique. Taking advantage of the device layer of a commercial SOI wafer, the thickness of the membrane can be accurately controlled. The thickness of the device layer is requested to the manufacturer. Importantly, the intrinsic stress in the device layer of the SOI wafer is almost zero, making the mechanical behavior of the membrane much more predictable.

4.4.2 Fabrication process

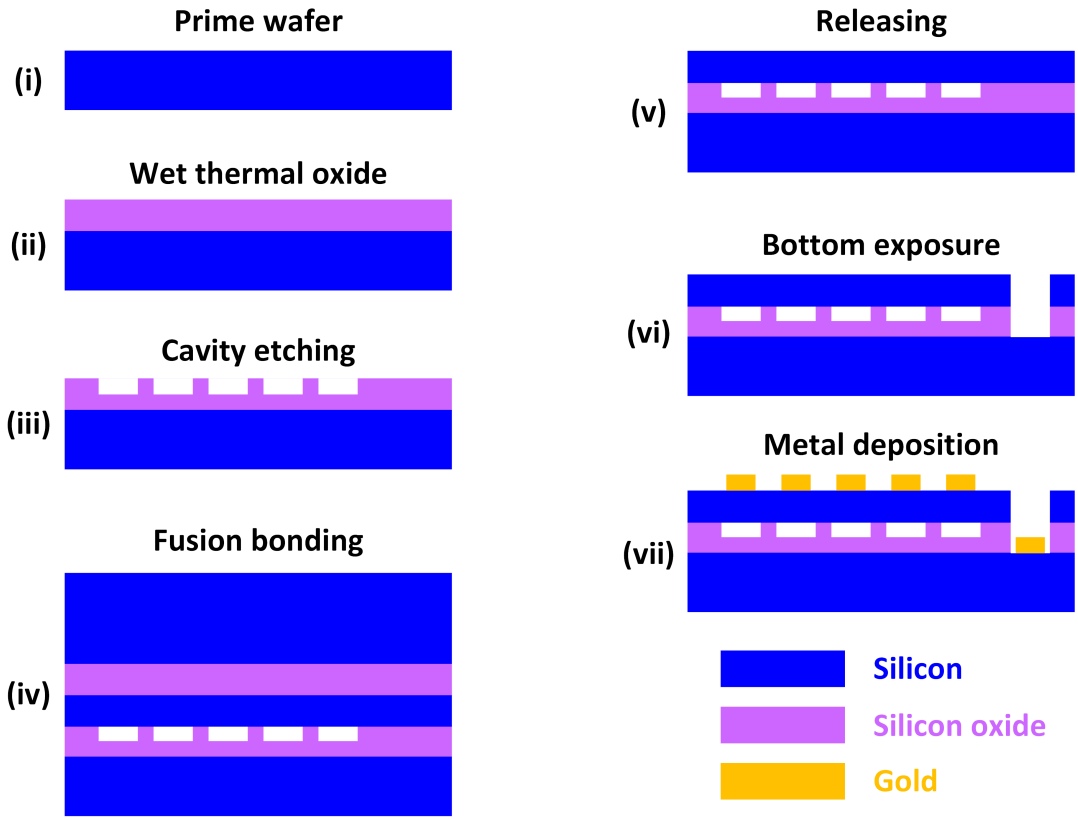

Figure 4.6: Fabrication flow of the μTEH.

The fabrication process of the μTHE started from a 100-mm P-doped 0.01 ohm·cm ⟨100⟩ silicon prime wafer (500 μm thick). (i-ii) 300-nm-thick wet thermal silicon oxide was grown on the surface of the wafer. (iii) Next, the photolithography and RIE process was performed to pattern the cavities. Before fusion bonding, a standard clean process (Piranha cleaning + RCA

cleaning) was conducted for the patterned wafer and the pristine SOI wafer (2 μm of P-doped 0.001 ohm·cm device layer, 1 μm of boxing layer, 350 μm of handling layer; purchased from Ultrasil, Hayward, California). (iv) Then, fusion bonding was performed with the pressure of 3 kg/cm^2 and the temperature of 480°C in vacuum (10^{-3} Pa), followed by 1100°C annealing. Through this step, vacuum cavities were formed. (v) A combination of RIE and tetramethylammonium hydroxide(TMAH) etching was used to etch the handling layer of the SOI wafer. The boxing layer was then removed by a 5:1 buffered oxide etch (BOE) solution. (vi) Another photolithography and RIE process was conducted to expose the bottom silicon (as the bottom electrode). (vii) Lastly, an electron-beam deposition, followed by a lift-off process, was done to create Ni (5 nm)/Au (150 nm) contact pads for wire-bonding.

The fabrication process of the μTEH is almost same as the fabrication process of capacitive miceomachined ultrasounic transducer (CMUT) except the cavity depth. CMUT is working under a DC bias (~80% of the collapse voltage) and the membrane should never touch the substrate. For CMUT, the cavity depth is determined by the maximum displacement at collapse voltage. For μTEH, the cavity depth is highly dependent on the static displacement of the membrane.

4.5 Results and discussions

4.5.1 Surface potential characterizations

Up to now, the exact mechanism of the triboelectrification is still ambiguous. In the area of TENG, a widely-accepted viewpoint to explain the mechanism is that the mobile charges can transfer from the surface with higher energy level to the surface with lower energy level [141, 142]. To experimentally quantify the energy level, a commonly-used measurement is

surface potential. The surface potential difference between two materials suggests how easily the mobile charges can transfer between the two materials. Among all reported TENGs, silicon and silicon oxide are never utilized as the triboelectric pair. To unveil the mechanism of the triboelectrification between silicon and silicon oxide, scanning Kelvin probe microscopy (SKPM) measurements were performed to determine the surface potentials [143–146].

SKPM characterizes the contact potential difference (CPD) between the sample and a reference conductive AFM tip. The representative experimental setup of the SKPM characterization is demonstrated in Fig. 4.7a. Initially, the Fermi energy levels of the sample and the tip are different. During the SKPM characterization, the sample is attached on a conductive and grounded substrate via silver paste and a conductive tip is approaching the sample surface with a tiny separation. When they are close enough, free charges (typically electrons) on the surfaces will transfer from one to the other through tunneling effect. At the steady state, the Fermi energy levels are lined up and a CPD is formed. As shown in Fig. 4.7b, an external DC bias voltage is applied to nullify the CPD. This nullifying voltage is taken as contact potential difference (V_{CPD}), which is defined as

$$V_{CPD} = \frac{\phi_{tip} - \phi_{sample}}{e} \tag{4.16}$$

where ϕ_{tip} and ϕ_{sample} are the work functions of the conductive tip and the sample. According to Eq. 4.16, the material with a higher V_{CPD} has a lower surface energy level. When two materials come into contact, free electrons tend to transfer from the material with higher energy level to the other.

In our experiments, SKPM measurements were performed by the scanning probe microscopy (Cypher S, Asylum Research) with the Ti/Pt (5/20)-coated silicon tip (tip radius of

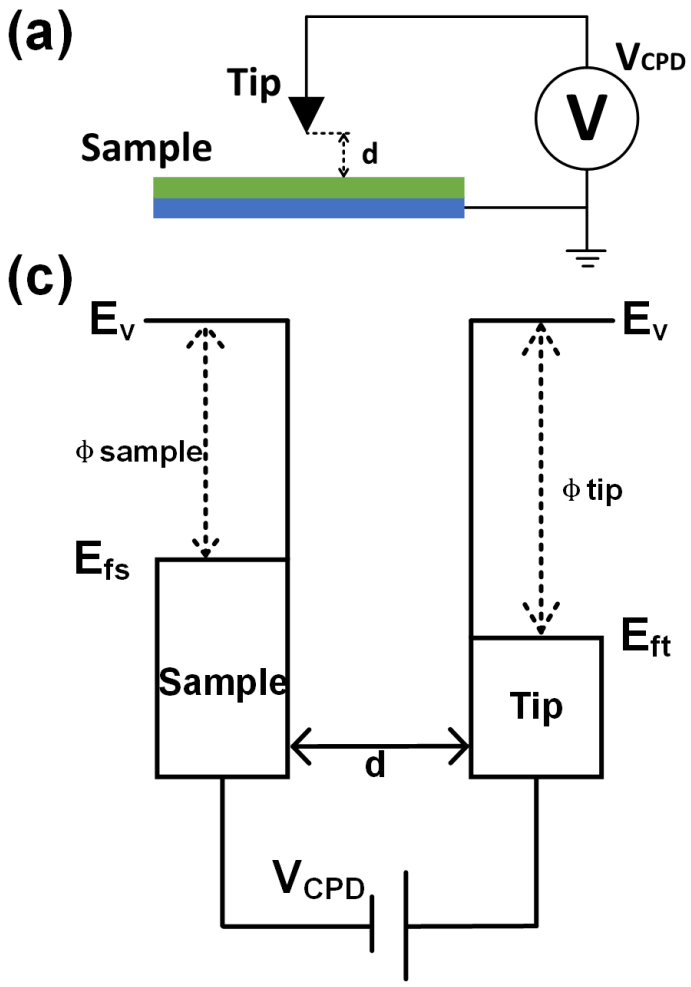

Figure 4.7: (a) The experimental setup and (b) the working principle of the SKPM. E_v is the vacuum energy level. E_{fs} and E_{ft} are the Fermi energy levels of the sample and tip.

28 ± 10 nm, force constant of 2 N·m^{-1}, and the resonant frequency of 70 kHz). 2×2 μm^2 size images were scanned at a scanning frequency of 0.3 Hz, with a separation of 50 nm between the tip and sample in atmospheric pressure at room temperature. To precisely evaluate the V_{CPD} of the triboelectric pair in the μTEH, we used the wafer, with the exactly same parameters as that in the fabrication, for measurements. Bare silicon wafer (P-doped 0.001 ohm·cm ⟨100⟩) and silicon oxide wafer (P-doped 0.01 ohm·cm ⟨100⟩ silicon wafer with 300-nm wet thermal oxide) were prepared and diced into small piece (1×1 cm^2) to fit the sample substrate. After ultrasonic cleaning in acetone, isopropanol and deionized water, we performed the SKPM measurements for silicon and silicon oxide pieces, respectively. Then, silicon and silicon oxide pieces were

forced to tap with each other for 100 times and SKPM measurements were conducted again. The measured mappings of the V_{CPD} are illustrated in Fig. 4.8.

As shown in Fig. 4.8, the average V_{CPD} in the tested area are initially 885.5 mV and 449.5 mV for silicon and silicon oxide, respectively. Apparently, silicon oxide has a higher surface energy level so that electrons will transfer from the silicon oxide surface to the silicon surface through triboelectrification. Thus, the surface of silicon oxide is positively charged while the silicon is negatively charged. Due to the accumulation of charges, the V_{CPD} of the silicon increases and the V_{CPD} of the silicon oxide decreases after tapping.

To further verify the mechanism of the triboelectrification, another SKPM measurements were performed. The accumulated charges on the surface of dielectric material dissipate very slowly so that the surface potential will be kept for a long time. In addition, the distribution of the surface potential on the sample's surface is assumed uniform. It is because the surfaces of both silicon and silicon oxide are flat enough and the whole surface has the same contact condition during measurements. Under these assumptions, the V_{CPD} mappings were also performed for silicon oxide after it was tapped with silicon for 100, 200, 300 and 400 times. The measured results are shown in Fig. 4.9.

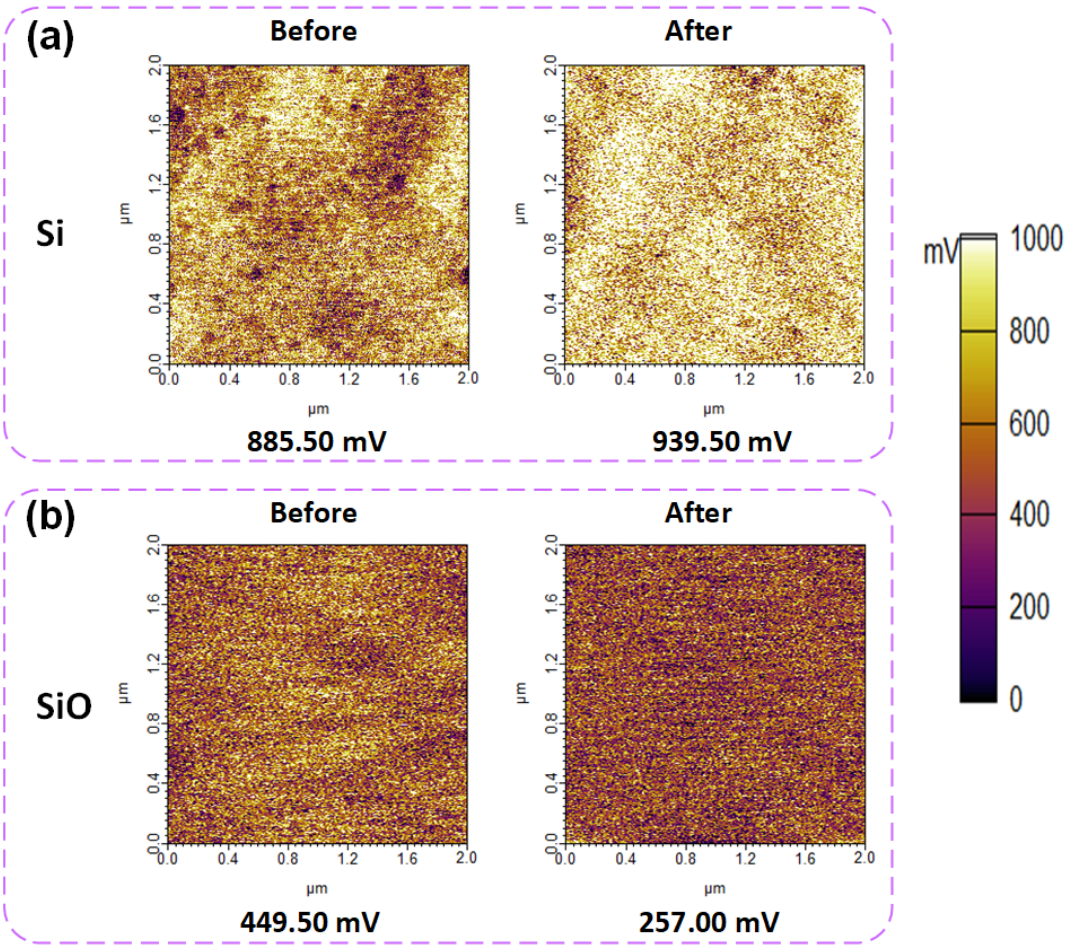

Figure 4.8: The SKPM mappings of(a) the silicon and (b) the silicon oxide before and after contacting.

It is seen that the average V_{CPD} of the silicon oxide keeps decreasing from 257 mV to -156.5 mV. It is because that positive charges keep accumulating on the surface of silicon oxide as tapping number increases. As a result, the surface energy level keeps increasing, inducing a smaller (or more negative) V_{CPD}. It is also noticed that the change of the V_{CPD} becomes slower from the first 100 times tapping to the last 100 times tapping. It is because the accumulated charges on the surface approach saturation after repetitive contacting. The experimental results are in accordance with the tendency of the triboelectric property and further verify the mechanism of the triboelectrification.

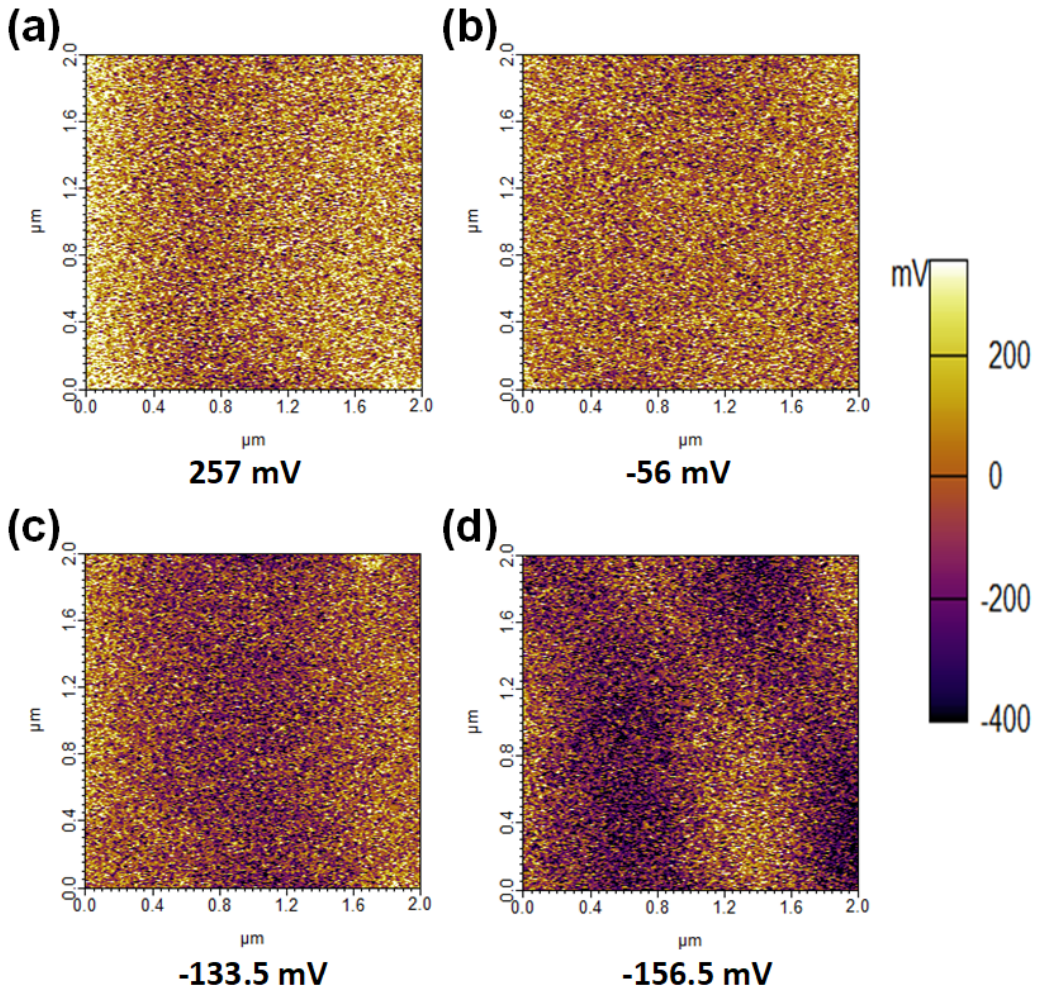

Figure 4.9: The SKPM mappings of the silicon oxide after (a) 100, (b) 200, (c) 300 and (d) 400 times tapping with silicon.

4.5.2 Results of theoretical analysis

Table 4.1 gives the required parameters for the analytical calculation. The radius of the circular membrane is 50 µm. Based on the analytical calculation, the resonant frequency and the static displacement surface of the membrane were calculated. The calculated static displacement surface is shown in Fig. 4.10.

Table 4.1: Parameters for the theoretical analysis.

Parameter	Quantity
Thickness of Si layer	2 μm
Thickness of SiO_2 layer	230 nm
Thickness of top electrode	150 nm
Young's modulus of Si	170 GPa
Poisson ratio of Si	0.28
Density of Si	2329 kg/m^3
Sound speed	m/s
Radius of medium	500 μm
Radius of the circular membrane	50 μm

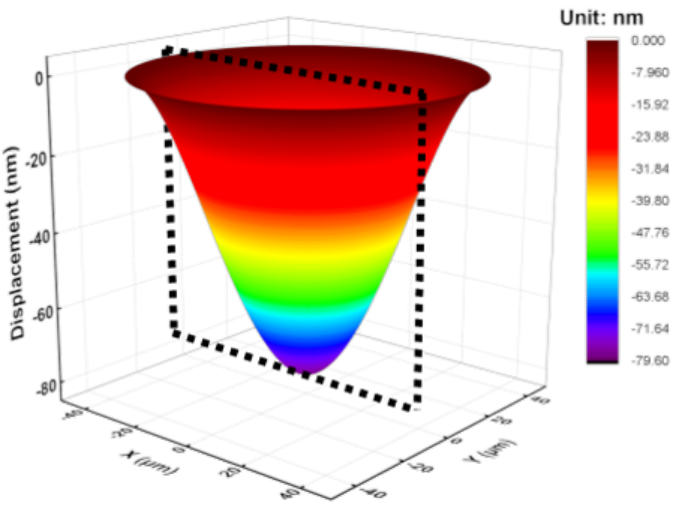

Figure 4.10: The calculated displacement surface of the circular membrane based on the analytical calculation.

For further verification, the finite element method (FEM) was also utilized to simulate the resonant frequencies and the static displacement surface of the circular membrane via the software COMSOL Multiphysics. Two physics (pressure acoustics and solid mechanics) were built in the COMSOL. On top of the membrane, the medium was set as water in agreement with the

analytical calculation. The top surface of the membrane was defined as the acoustic-structure boundary for coupling of two physics. Proper boundary conditions were applied and the mechanical behaviors were simulated. Limited to the computational capacity of the computer, only one-quarter geometry was built and symmetric conditions were applied in COMSOL. Atmospheric pressure was applied by setting a boundary load on the top surface of the membrane in the COMSOL 3D model (shown in Fig. 4.11). Then, an incident acoustic wave was induced in the medium, which propagated in perpendicular to the top surface of the membrane. Frequency sweep of the incident acoustic wave was performed and the displacement of the center point of the membrane was plotted along the frequency spectrum. The parameters for simulation also refer to Table 4.1 and the results are shown in Fig. 4.12a. The resonant frequency of the membrane in water corresponds to the frequency where the maximum displacement happens. The static displacement surface of the membrane was also obtained, shown as Fig. 4.12b.

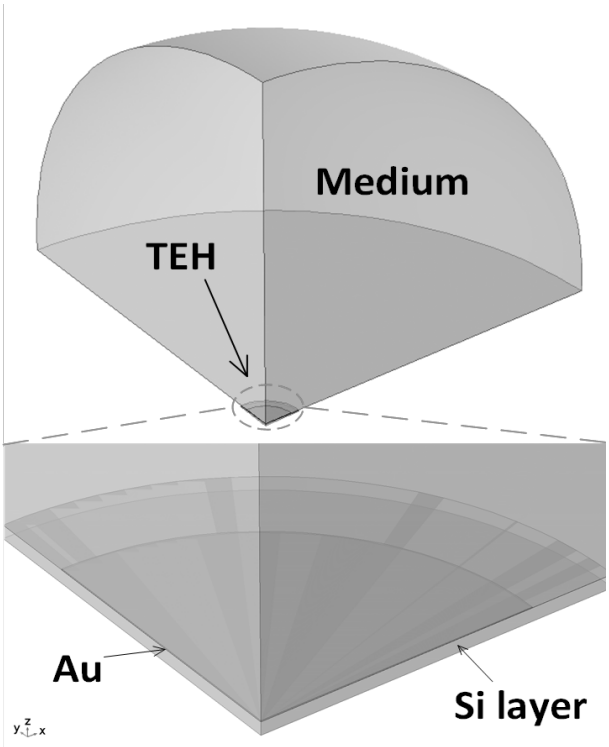

Figure 4.11: 3D model of the μTEH built in COMSOL for FEM simulation.

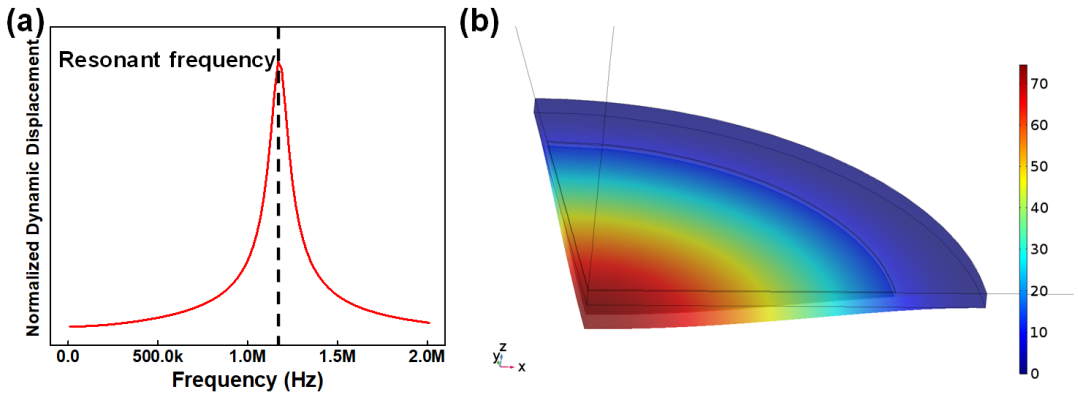

Figure 4.12: (a) The displacement dependence of the frequency of the incident acoustic wave and (b) the simulated displacement surface of the circular membrane in COMSOL.

In both Fig. 4.10 and 4.12b, a vertical plane passing through the center point of the membrane cuts the static displacement surface and profiles of the static displacement were obtained. Fig. 4.13 compares the the static displacement curves from the analytical calculation and the FEM simulation, respectively.

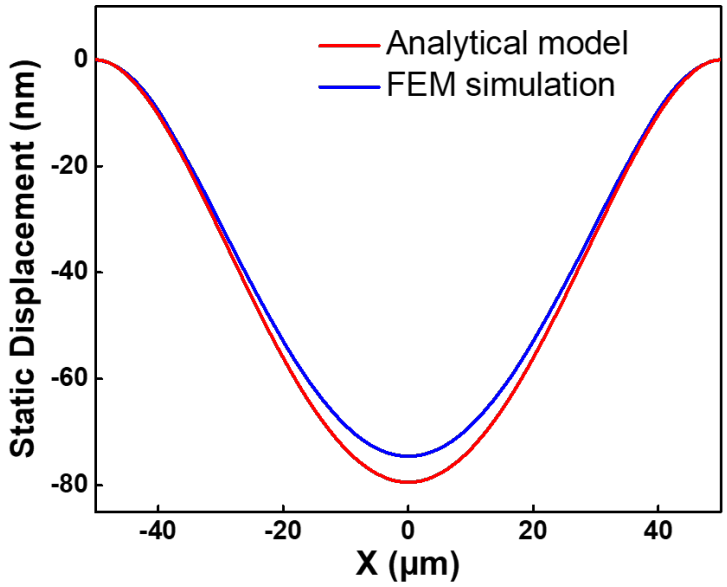

Figure 4.13: The static displacement profiles across the center point of the membrane.

The results from the analytical calculation and FEM simulation are listed in Table 4.2. The resonant frequency of the membrane from the analytical calculation and FEM simulation is 1.18

MHz and 1.17 MHz, respectively. It should be noticed that the resonant frequency from the analytical calculation is slightly smaller than that from the FEM simulation. The discrepancy is because the analytical calculation only considers the silicon membrane and eliminates the effect of the top electrode (Au). On the contrary, everything is taken into consideration in the FEM simulation. Because Young's modulus of silicon is higher than that of Au, the addition of the top electrode decreases the effective Young's modulus of the membrane and lowers the resonant frequency. In addition, the maximum static displacement under the atmospheric pressure is located at the center point of the membrane. Based on the analytical calculation and the FEM simulation, the maximum displacements are 79.4 nm and 74.5 nm, respectively. Though a slight difference, these results still show high consistency. This small distinction can also be explained by the consideration of the top electrode.

In practice, the cavity depth should be larger than the maximum static displacement to avoid collapse. Meantime, a smaller cavity depth is desired to achieve a larger contact area. Therefore, the cavity depth is targeted to 90 nm, which is a little larger than the theoretical maximum membrane displacement. Since RIE is not a scrupulously precise technique and the etching rate varies with the machine conditions, we should take the fabrication deviation into the consideration and give some room for error in the fabrication.

Table 4.2: Results of the analytical calculation and FEM simulation.

Radius		Max Static Displacement	Resonant Frequency
50 μm	(Analytical)	79.4 nm	1.18 MHz
	(FEM)	74.5 nm	1.17 MHz

4.5.3 Structural dimensions

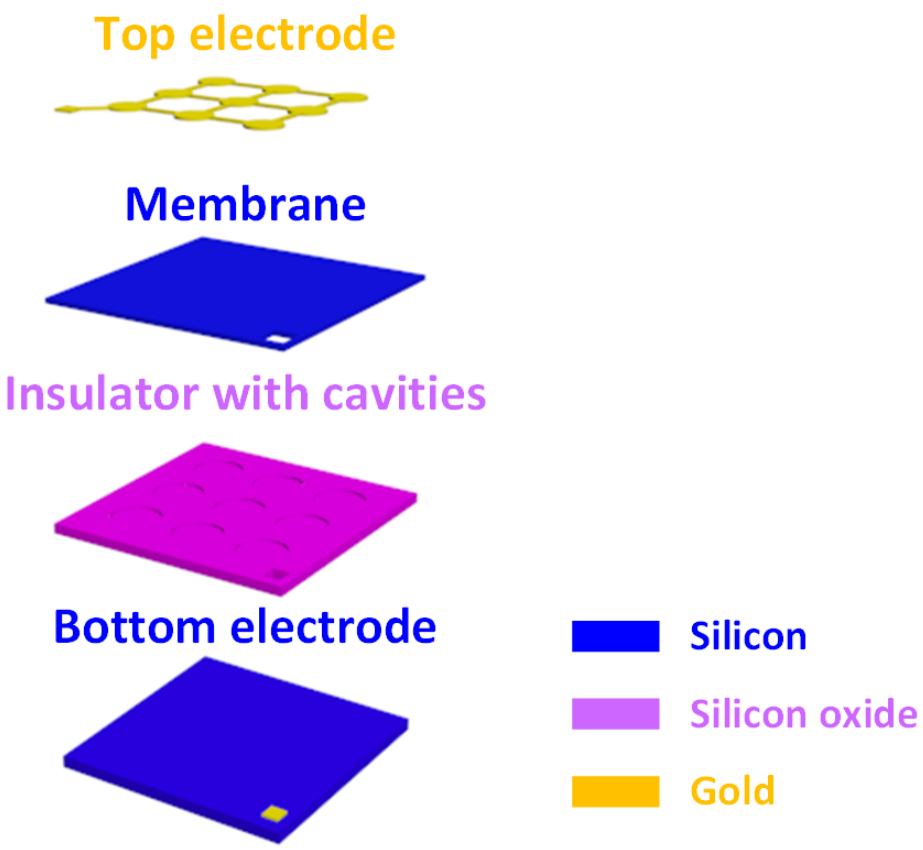

Figure 4.14: The exploded view of the μTEH.

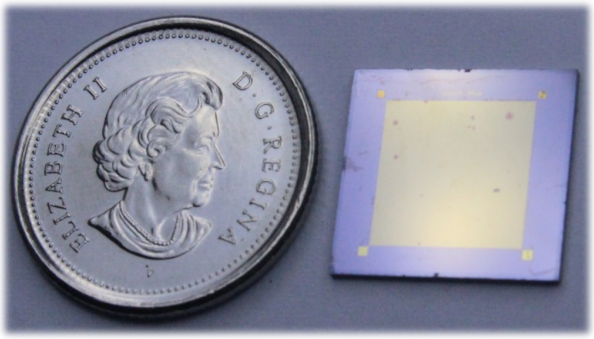

Figure 4.15: The photograph of the real device of the μTEH.

Fig. 4.15 and 4.14 give the photograph and the exploded view of the μTEH. Microscope images were taken to show the structural dimensions of the μTEH from top view (shown as

Fig. 4.16a). The aperture of the μTEH is around 7×7 mm^2. In terms of cells, the radius of the circular membrane is 50 μm and the interspace between two cells is 20 μm.

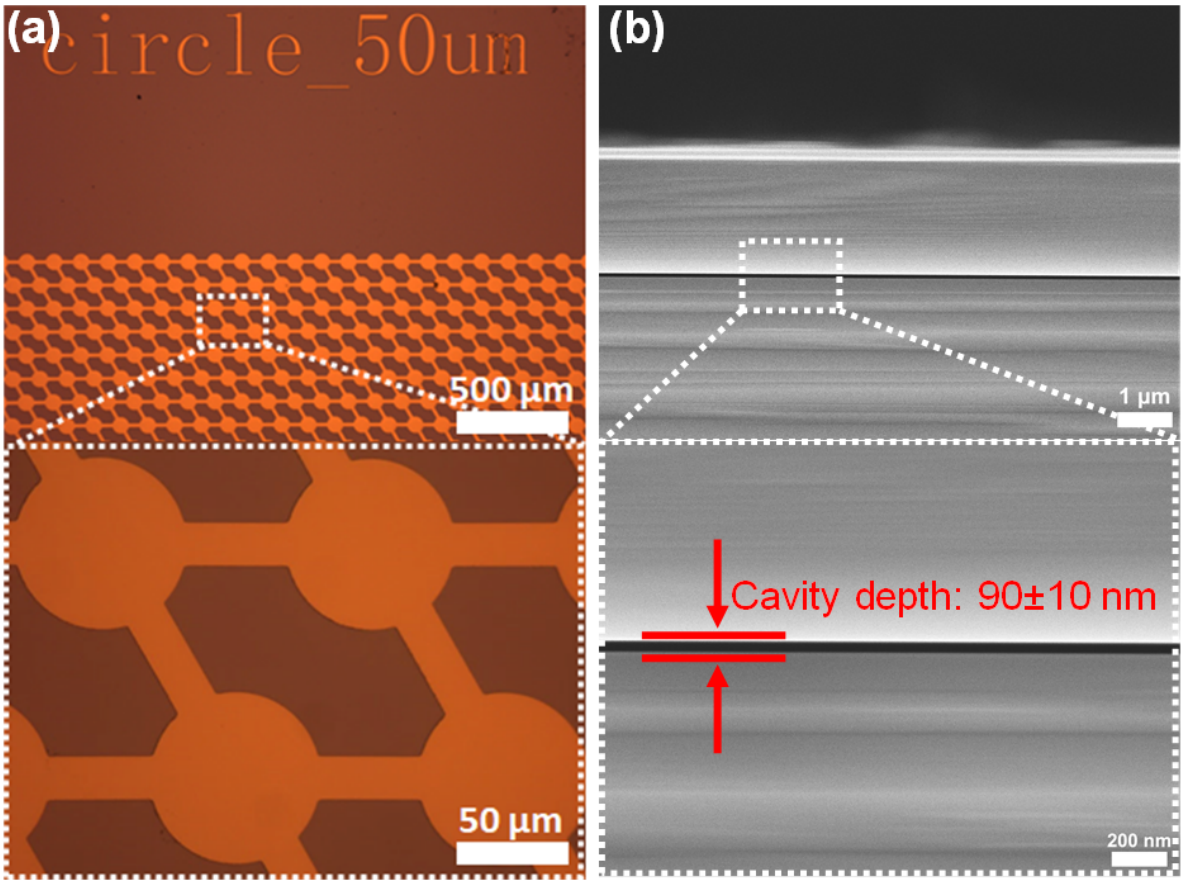

Figure 4.16: (a) The optical microscope images of the μTEH. (b) SEM images of the cross-sectional view of the μTEH.

In consideration of the fabrication deviation, the cavity depth was targeted to 90 nm to satisfy the geometric requirements of the μTEH. SEM images illustrate the cross-sectional view of the μTEH, which clearly show the cavity structure (as shown in Fig. 4.16b). It is seen that the actual cavity depth is exactly 90±10 nm.

4.5.4 An indirect method to verify resonant frequency

Essentially, different methods can be adopted to measure the resonant frequency of the μTEH, such as impedance analysis and vibrometer test. However, neither of them are effective for the fabricated μTEH due to the small separation between the membrane and the substrate. During the tests, the signals are too weak to be detected. An alternative is to perform the pitch-catch experiment. A frequency sweep is performed to the ultrasound source and the open-circuit voltage of the μTEH is measured. The resonant frequency is where the open-circuit voltage has the maximum value. However, it is difficult to find out a perfect ultrasound source that can generate constant acoustic pressure over the whole range of frequency at a specific position.

In this work, we proposed an indirect method to experimentally verify the resonant frequency of the μTEH. We used a pre-fabricated CMUT, which is for another project, to characterize the resonant frequency. The detailed fabrication process is shown in Appendix D.

Fig. 4.17a shows the whole structure of the fabricated CMUT 2D array. From the point of the single cell, the membrane structure of the CMUT are exactly same as that of the μTEH. For both the μTEH and the CMUT, they have the cell radii of 50 μm and the membrane thickness of 2 μm. Fig. 4.17b and c illustrate the structure at the corner of the cavity for the CMUT and the μTEH, respectively. The difference of the cavity depth is clearly shown from the SEM images.

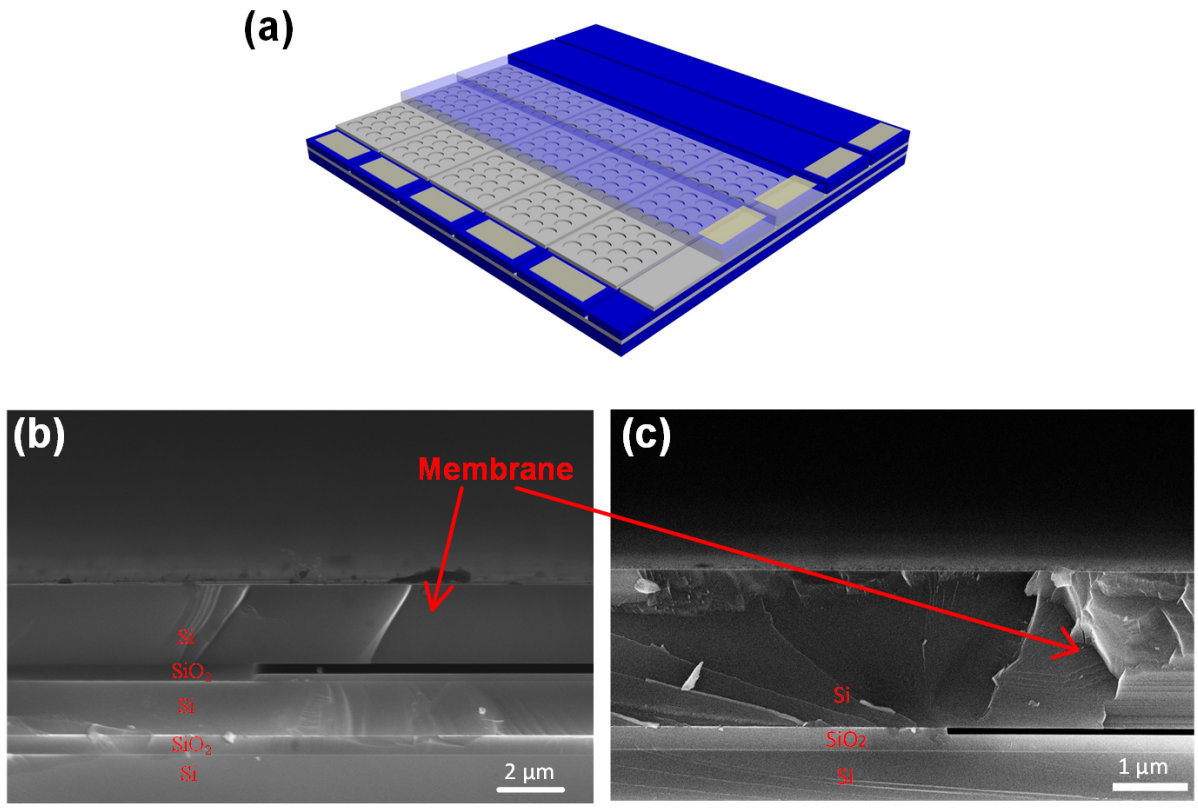

Figure 4.17: (a) The representative diagram of the CMUT. The SEM images of (b) the CMUT and (c) the μTEH.

Typically, the CMUT can be considered as a diaphragm-structured resonator working under a DC bias. The DC bias will dramatically improve the response of the CMUT but cause a red-shift of resonant frequency due to the so-called spring-softening effect. Experimentally, the resonant frequency of the pre-fabricated CMUT in the air was measured by a vector network analyzer (VNA, TTR503a, Tektronix). Fig. 4.18 shows the electrical schematic of the circuit for the VNA test.

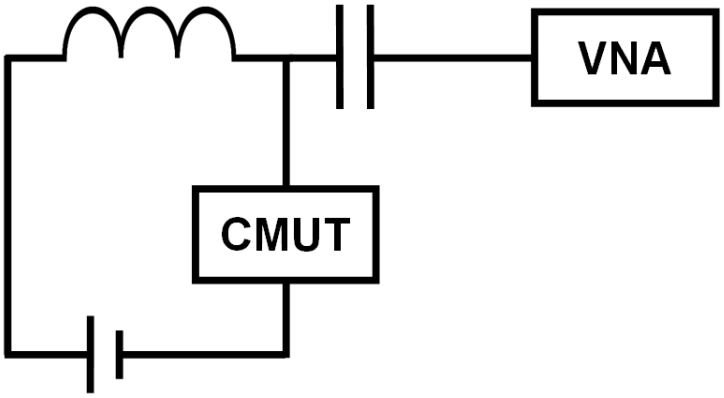

Figure 4.18: The electrical schematic of circuit used to characterize the CMUT.

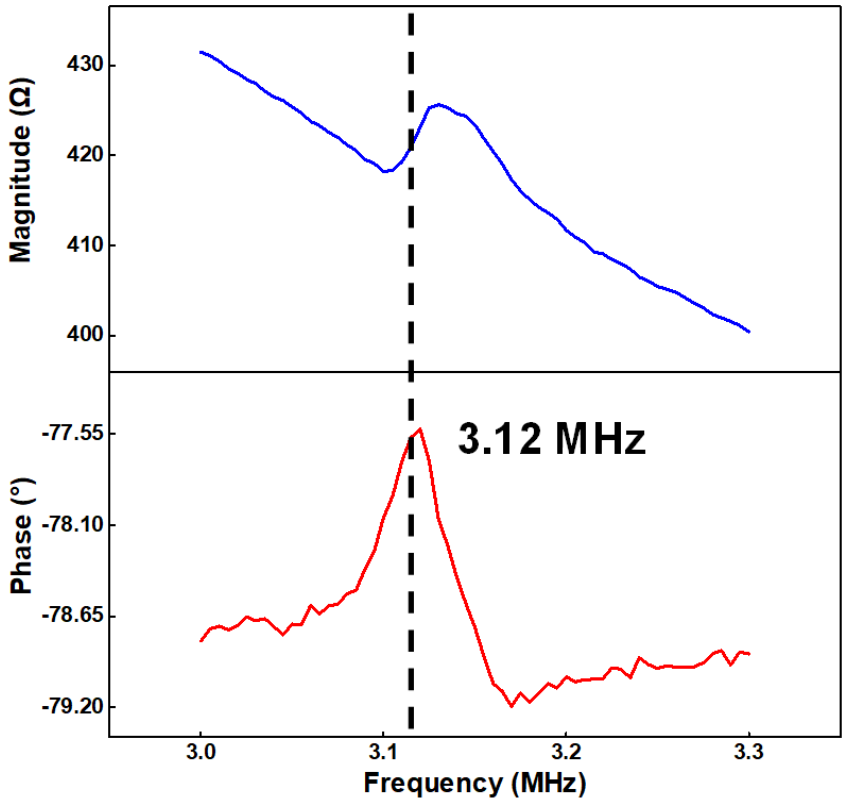

Figure 4.19: The impedance analysis results of the pre-fabricated CMUT.

The measured s-parameter was converted to impedance results by following equation

$$Z = Z_0(\frac{S_{11}+1}{S_{11}-1}) \tag{4.17}$$

where Z is the complex impedance of the tested device and Z_0 is the system impedance (50 Ω). S_{11} is the reflection coefficient of the input port of the VNA. Fig. 4.19 is the converted impedance results of the pre-fabricated CMUT under 10 V bias. From the impedance analysis, the resonant frequency of the 10 V biased CMUT is 3.12 MHz in air. Back to the analytical calculation, the 1st mode resonant frequency of the μTEH with a circular membrane in air is[121]

$$f = 0.469\frac{hc_p}{a^2} \tag{4.18}$$

Substituting the parameters from Table 4.2, the calculated resonant frequency is 3.34 MHz. Taking the DC bias into consideration, the measured resonant frequency and calculated one are consistent with each other. Due to the damping of the water, the in-immersion resonant frequency of the diaphragm-structured resonator is typically ~3 times lower than the in-air resonant frequency. Therefore, the resonant frequency of the circular μTEH can be reasonably considered close to 1 MHz in immersion.

4.5.5 Response to ultrasound

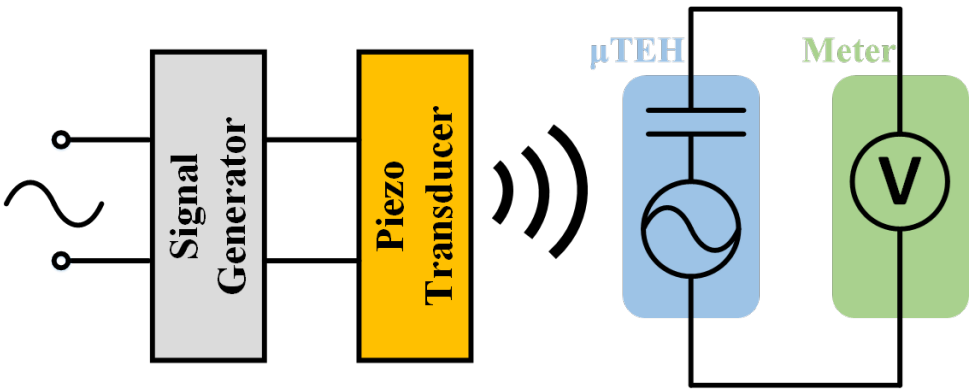

Figure 4.20: The schematic of the experimental setup.

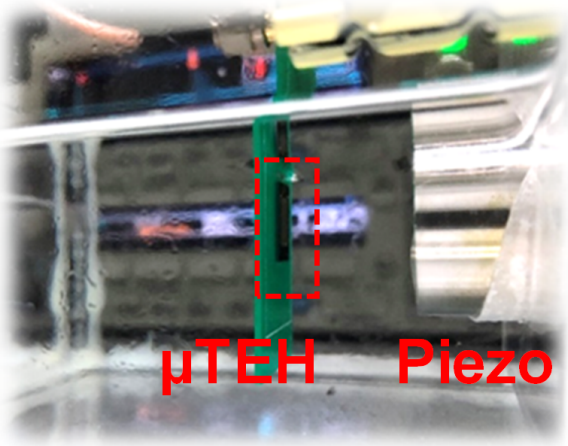

Figure 4.21: The photograph of the ultrasound link.

To characterize the electrical output performance of the μTEH, an ultrasound link was designed and established. The schematic of the experimental setup is illustrated as Fig 4.20. A commercial piezo transducer (ABLL, China) was used to generate ultrasound, whose resonant frequency was 1.0105 MHz (impedance analysis is shown in Fig. 4.22). As shown in Fig. 4.21, both the μTEH and the piezo transducer were immersed into vegetable oil with a distance of ~25 mm. In the experiment, vegetable oil was used as the medium because it had similar acoustic properties as water but can prevent shorting (see Appendix C). Fig. 4.22 illustrates the impedance analysis of the commercial piezo transducer, whose fundamental resonant frequency is 1.0105 MHz. During the experiment, the piezo transducer was actuated by a continuous sinusoidal wave with the amplitude of 10 V and the frequency of 1 MHz. From Fig. 4.22, the piezo transducer has the impedance of 57.4 Ω at the frequency of 1 MHz and this impedance is close to the output impedance of the signal generator (50 Ω). The actual driving signal applied to the piezo transducer has the amplitude of ~5 V. The open-circuit voltage (V_{OC}) of the μTEH is ~15.5 mV_{P-P} (illustrated in Fig. 4.23). It is also noticed that the positive peak voltage is ~6.6 mV while the negative peak voltage is ~7.7 mV. This attributes to the asymmetry of the operating mode, where silicon and silicon oxide contact in half cycle and do not contact in the

other half cycle. Since the displacement of the membrane is quite small, the responses of these two half cycles only have tiny difference.

Furthermore, a linear relationship between the peak open-circuit voltage and the incident acoustic pressure for the μTEH was found (shown in Fig. 4.24). This linear property of the output voltage are attributed to the change of the contact area. As the incident acoustic pressure increases, the contact area between the silicon membrane and the silicon oxide substrate also increases. This induces a more sufficient triboelectrification (higher surface charge density) and a higher output voltage. It is noted that the plot is fairly noisy. It is because the separation between the piezo transducer and the μTEH is ~25 mm, which is within the near field of the piezo transducer. The generated acoustic pressure within near field is relatively perturbative.

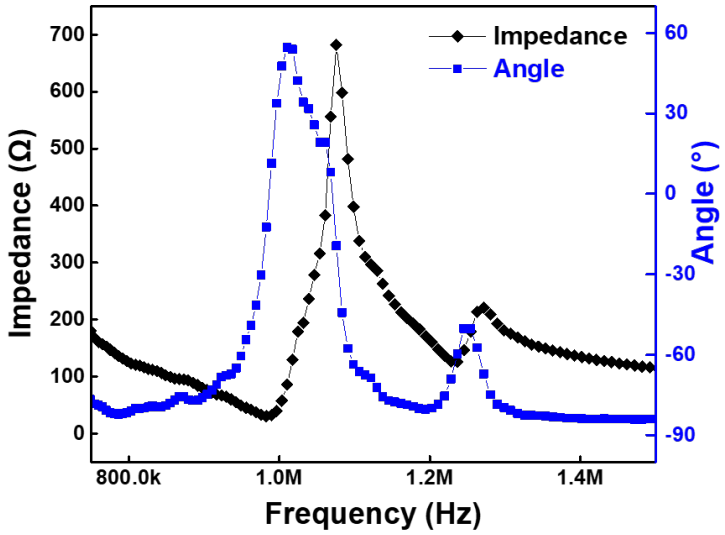

Figure 4.22: The impedance analysis of the commercial piezo transducer.

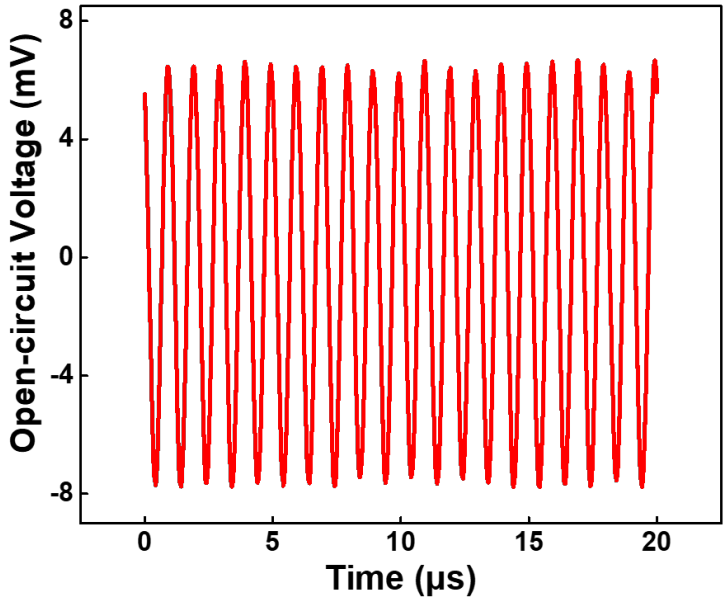

Figure 4.23: The open-circuit voltage (V_{OC}) of the μTEH.

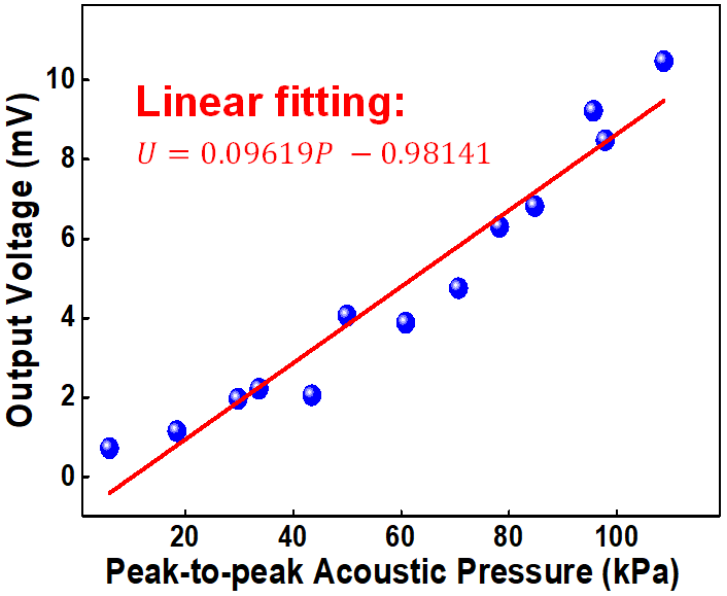

Figure 4.24: The relationship between the amplitude of the open-circuit voltage and the incident acoustic pressure for the μTEH (1 MHz).

4.6 Chapter conclusion

In this chapter, a novel μTEH was successfully developed by MEMS technologies. It is the very first MEMS TENG in the world. The combination of TENG and MEMS technology significantly promotes the miniaturization and the integration of TENG. Taking advantage of the wafer bonding technique, vacuum cavities were built to improve the output and the performance reliability of the TENG. With the incident acoustic wave (1 MHz, 63 kPa), the μTEH could achieve the open-circuit voltage of 15.5 mV_{P-P}. A linear relationship between the peak open-circuit voltage and the acoustic pressure was also observed.

Chapter 5

Potential applications and optimization methodologies of the micro- triboelectric energy harvester

In the previous chapter, a novel triboelectric energy harvester was successfully developed. This chapter will demonstrate two potential applications of the μTEH. Further optimization methodologies are also proposed to improve the performance of the μTEH.

5.1 Demonstration of potential applications

In this section, potential applications of the μTEH were explored and demonstrated in vitro. As aforementioned in the previous chapter, we proposed to use the μTEH for acoustic energy transfer and wireless communication via ultrasound link, demonstrated in Fig. 5.1.

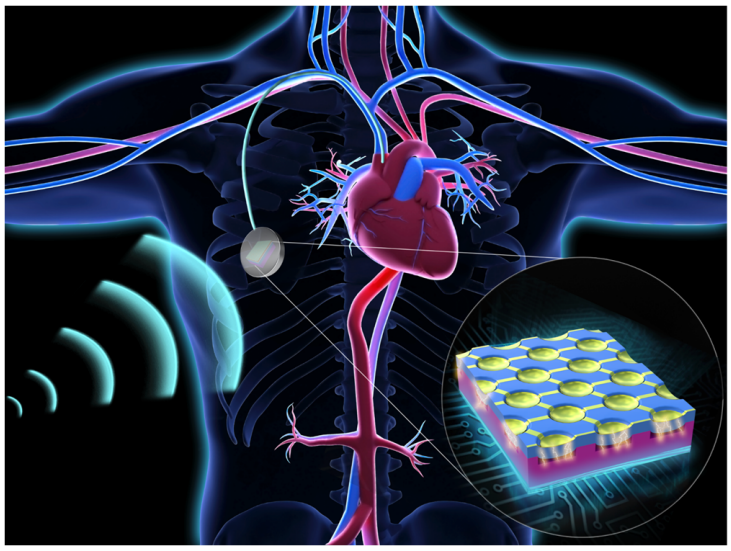

Figure 5.1: Representative diagram of acoustic energy transfer and wireless communication via ultrasound link.

5.1.1 Acoustic energy transfer

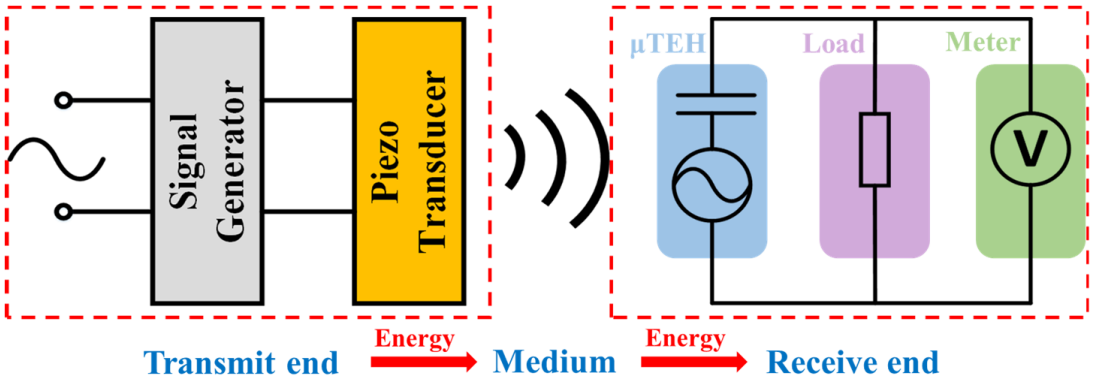

Figure 5.2: The schematic of the experimental setup for wireless energy transfer.

To demonstrate the application of the μTEH for AET, an ultrasound link was established (schematically shown as Fig. 5.2). A commercial piezo transducer, actuated by a signal generator, was used as an external acoustic source. The μTEH, mounted on a customized PCB, acted as a receiver to harvest the acoustic energy. A load resistor was connected in series with the μTEH for calculating the output electrical power. The piezo transducer and the μTEH (with a distance of ~25 mm) were well aligned and immersed into vegetable oil, which simulates the

human tissues and prevents shorting (depicted as Fig. 4.21). A continuous sinusoidal wave (20 V_{P-P}, 1 MHz), produced by a signal generator (Tektronix, AFG 1022), was input into the piezo transducer and the output voltage on the load resistor was measured by an oscilloscope (Tektronix, MDO 3024).

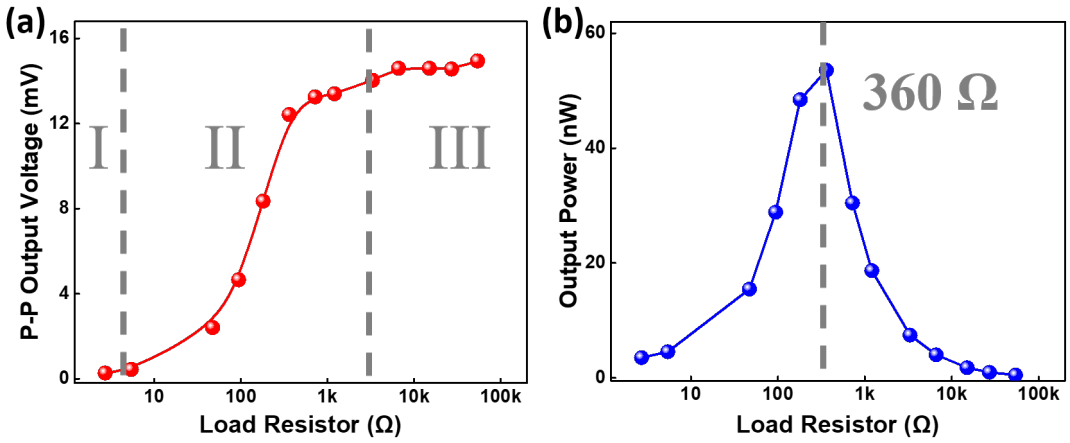

Figure 5.3: (a) The relationship between the output voltage of the μTEH and the load resistor. (b) The relationship between the output power of the μTEH and the load resistor.

The relationship between the output voltage of the μTEH and the load resistor is illustrated in 5.3a. It is clearly seen that three regions (marked as region I, II and III) can be defined though the output voltage keeps increasing along all three regions. The output voltage increases gently in the region I and III but rapidly in region II. It can be explained that the inherent impedance of the μTEH is dominant compared to the external load resistor in the region I and the circuit can be considered as a short circuit. In region III, the resistance of the external load resistor is much greater than the inherent impedance of the μTEH, such that the open-circuit voltage almost applies on the load resistor. However, the impedance of the μTEH and load resistor is comparable in region II and the output voltage changes with the load resistance dramatically.

Meanwhile, the dependence of the output power on the load resistor was plotted in Fig. 5.3b. With the load resistor of around 360 Ω, the μTEH reaches the peak output power, 50 nW.

In the medium, the ultrasound intensity (I) of continuous wave is defined as

$$I = \frac{P^2}{2\rho c} \tag{5.1}$$

where P is the amplitude of the ultrasound pressure, ρ is the density of the medium and c is the sound speed in the medium.

With the same experimental setups and settings, the μTEH was replaced by a hydrophone (Precision Acoustics, 46 mV/MPa sensitivity @1 MHz) to measure the acoustic pressure at the location of TEH. The measured acoustic pressure amplitude (P) is 63 kPa and the calculated ultrasound intensity is 132 mW/cm^2. From chapter 4, the open-circuit voltage of the μTEH shows an approximately linear relationship with the incident acoustic pressure. Therefore, the relationship between the output power on the load resistor and the incident acoustic pressure is also considered in linearity. The maximum output on the load resistor can reach up to 273 nW if we give the incident acoustic pressure to 720 mW/cm^2, which is the limit set by FDA regulations. To power electronics, a high-frequency rectifier is required to convert the AC power to DC power. Several researchers have reported the rectification circuit design and the efficiency can approach up to 89% [147]. Thus, the theoretically maximum output DC power should be more than 243 nW.

In the experiments, the variation of the output power along the axial direction was also observed (shown in Fig. 5.4). This phenomenon can be explained by the standing wave effect. Standing wave is a stationary wave, where each point on the axis of the wave has constant amplitude. The location, with minimum amplitude, is node while the location, with maximum amplitude, is antinode (shown in Fig. 5.5). Energy fluctuates along the axis: nodes have the maximum acoustic energy and antinodes have the minimum one. When the receiver is located

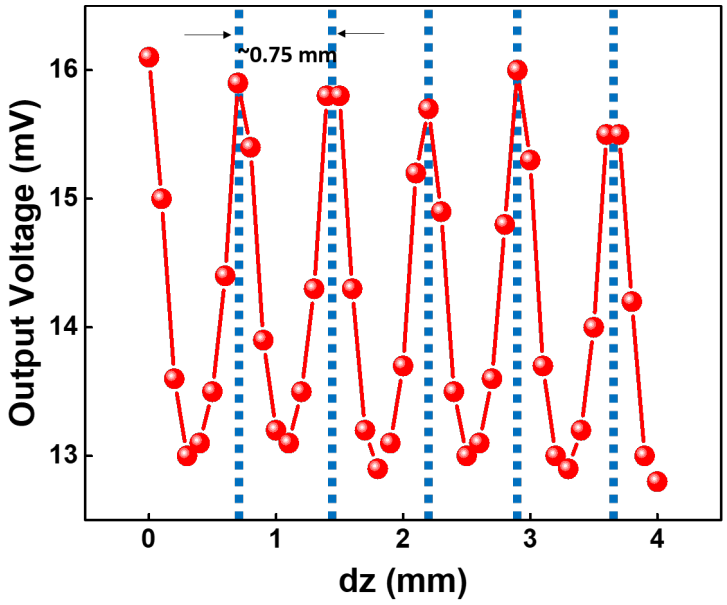

Figure 5.4: The standing wave effect on the acoustic energy transfer.

at the point where the acoustic energy is maximum, it will receive more acoustic energy and convert to more electric energy. Since piezo transducer and the μTEH are well aligned, the standing wave may be generated between the transmitter and receiver. Considering the acoustic impedance mismatch between transducers and medium, acoustic wave reflects every time it hits the transducer. These reflections make the acoustic energy persistent in the form of the standing wave. Therefore, the efficiency of the ultrasonic link is sensitive to the separation between transmitter and receiver. Only when the separation is integer multiples of one-half wavelength, the efficiency of the ultrasound link will be maximized.

In practice, the separation between transmitter and receiver is almost impossible to be precisely controlled. A so-called frequency tuning method is often used to solve this problem [148, 149]. By changing the frequency of the acoustic wave from the transmit end, the wavelength will also be changed, making the separation meets the abovementioned requirements. From the point of the receiver, it is highly desired that the energy harvester has a broad operating bandwidth. Otherwise, the output power will dramatically decrease when the acoustic wave's frequency deviates from the resonant frequency of the receiver. Because of the damping

outside the membrane, the diaphragm-structured transducer inherently has a wider operating bandwidth in immersion [149–151]. This inherent characteristic makes this type of transducer advantageous as a receiver in this particular application.

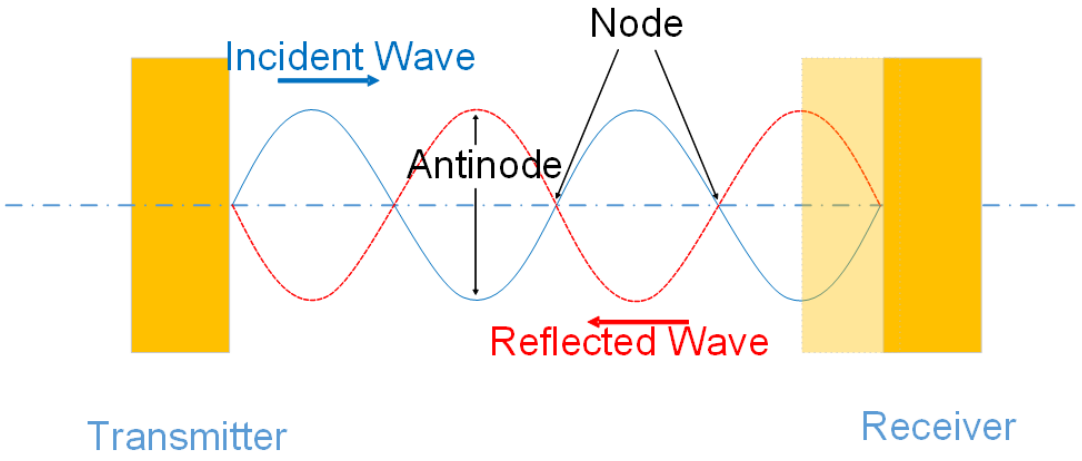

Figure 5.5: A simplified graphic representation of standing wave effect.

So far, very few MEMS acoustic energy harvesters are reported. Table 5.1 lists the published data of MEMS acoustic energy harvesters for implanted devices. For all references, the incident acoustic power density is normalized to 720 mW/cm^2. It is noticed that the efficiencies of reported MEMS acoustic energy harvesters are overall low (generally lower than 1%). Given the available reports, the power consumption of the implanted device can be lower than 100 nW [152]. Even though the efficiency of this work is still low, the output power can be stored or directly used for implanted devices. More importantly, the μTEH in this work is the very first MEMS TENG and has not been optimized yet. The output power can still be dramatically improved in the future.

Table 5.1: Published data of MEMS acosutic energy harvesters.

Reference	Frequency	Transducer type	Medium	Range	Power density	Efficiency
Fowler *et al.* [153]	25 kHz	Electrostatic	Air	50 mm	N/A (max 24.7 nW)	0.42%-1.58%
Horowitz *et al.* [154]	5.2 & 13.6 kHz	PZT thin film	Air	N/A	3.06 μW/cm^2	4×10^{-4}%-0.012%
Shi *et al.* [149]	300 kHz	PZT film	Water	10 mm	2.9 mW/cm^2	0.375%
This work	1 MHz	Triboelectric	Water	25 mm	0.50 μW/cm^2	4×10^{-4}%

5.1.2 Wireless communication

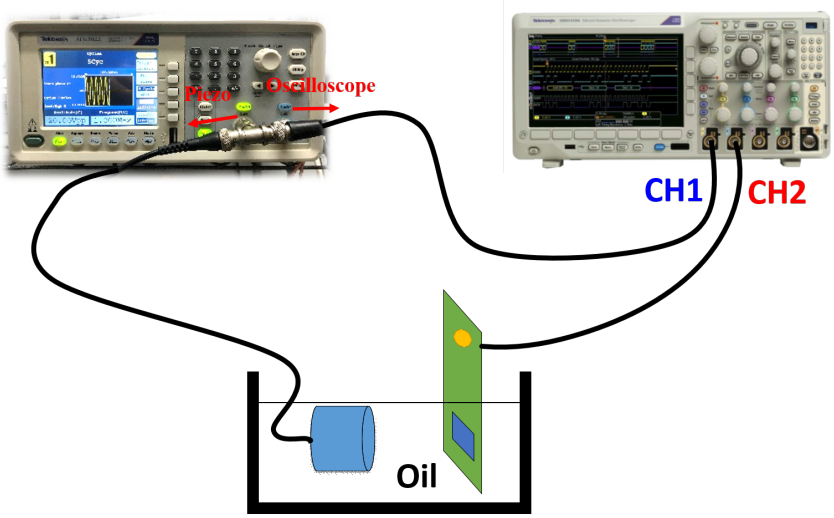

Figure 5.6: The schematic diagram of the experimental setup.

Another potential application of the μTEH is signal communication. With the similar experimental setups (shown in Fig. 5.6), burst-mode sinusoidal signal (20 V_{P-P}, 1 MHz) was input into the piezo transducer instead of the continuous wave. In this experiment, a tee adapter was adopted to split the output signal from the signal generator so that both the signal from the signal generator and the recovered signal from the μTEH can be monitored at the same time. In the oscilloscope, CH1 and CH2 give the signal from the tee adapter and the signal recovered from the μTEH, respectively. Both signals are averaged for 64 times to stabilize the reading.

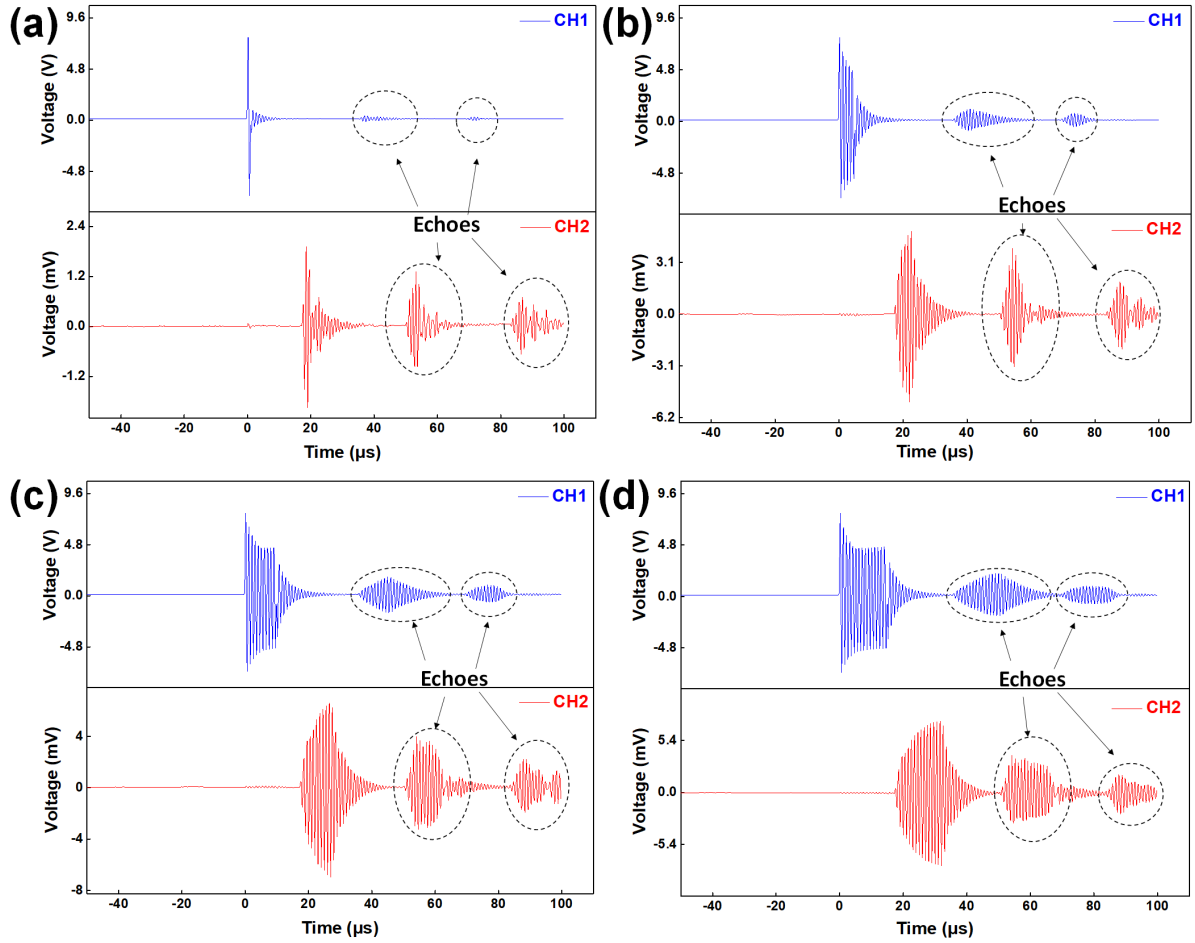

Figure 5.7: The input signal to piezo transducer and the output signal from the μTEH under (a) 1-cyc, (b) 5-cyc, (c) 10-cyc and (d) 15-cyc sine wave driven (1 MHz, around 25 mm separation).

The amplitude of the recovered signals from the μTEH is dependent on the cyclic number of the pulse. Fig. 5.7 shows the relationship between the amplitude of the recovered signals and the cyclic number of the pulse. It is observed that the amplitude of the recovered signal keeps increasing from 1 cycle to 15 cycles. The amplitude shows negligible change when further increasing the cyclic number. Among all four figures, echo signals can be seen for both the piezo transducer and the μTEH, indicating the separation of ~25 mm.

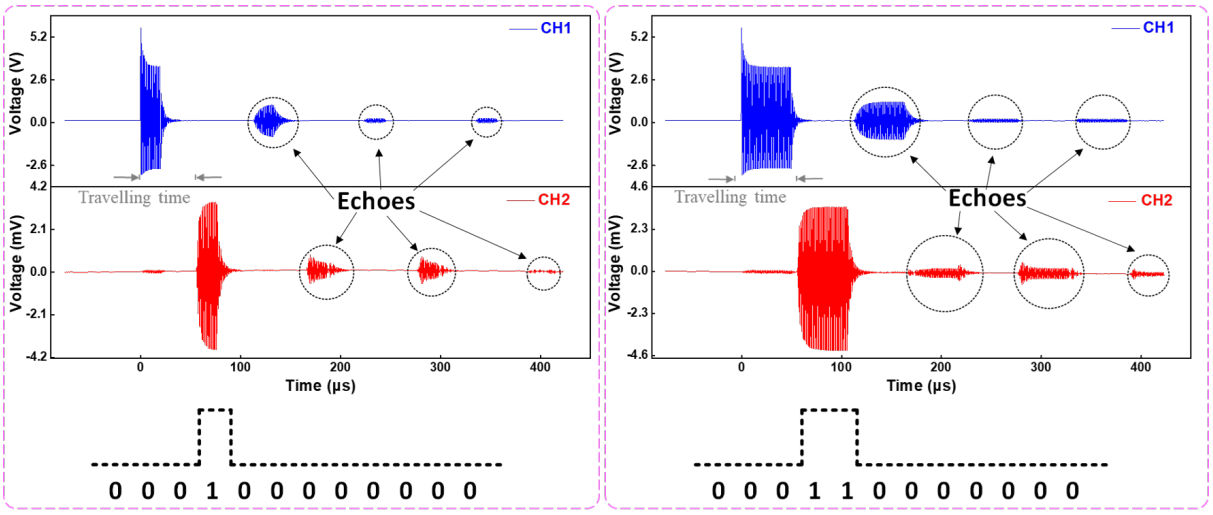

Figure 5.8: The input signal to piezo transduer and the output signal from the μTEH under 20-cyc (left) and 50-cyc (right) sine wave driven (1 MHz, around 85 mm separation).

Fig. 5.8 illustrates the CH1 and CH2 signals when 20-cyc (left) and 50-cyc (right) sinusoidal pulse signals input. To clearly distinguish the recovered signal and the echo signals, the piezo transducer and the μTEH were separated by ~85 mm, presenting ~56 μs traveling time of the ultrasound in the figure. Based on the recovered signal, the signal-to-noise ratio (SNR) of the μTEH can be calculated as 20.54 dB. If the transmitted control signal is modulated by digits"0" and "1", so-called amplitude shift keying (ASK) modulation, digital information can be transmitted via the ultrasound link [109, 155].

5.2 Optimization methodologies

Currently, the power consumption of most implanted devices is typically in the range of μW [156, 157]. Our reported AET system can only generate 243 nW power with 720 mW/cm^2 incident acoustic power, which is not a useful amount of power currently. It needs much more acoustic power than is currently allow under FDA limits if we actually apply it for powering

implanted devices. Refer to [65, 158], triboelectric acoustic energy harvesters can achieve energy conversion efficiency of 60% and 13.1% in water and in air, respectively. Therefore, further optimizations are still needed to improve the output power on the load in the future. Even if the efficiency of the μTEH can be improved to ~1%, the generated power will be useful. Most existing researches on the optimization of TENG are based on the trial-and-error method experimentally due to the lack of related theories. This section will qualitatively propose some optimization methods to improve the output of the μTEH according to the existing theories.

From the point of view of acoustic receiver, acoustic impedance can also affect the transmission efficiency. However, the structure of the μTEH is inspired by CMUT, which has the diaphragm structure. One of the advantages of this type of transducer is low mechanical impedance. For example, the acoustic impedance of CMUT is generally less than 10 MRayl. We usually consider that the acoustic impedances between the membrane and the medium are already matched. So, we will not put too much focus on the acoustic impedance matching at this stage.

5.2.1 Performance figure-of-merits of TENG

To compare the maximum output of TENGs (even with different configurations) in a fair manner, an important term is introduced: performance figure-of-merit (FOM_P) [159, 160]. FOM_P is a nondimensional parameter, which is independent of the working mode and the structural dimensions of the TENG, to evaluate the maximum output power of a TENG. Ideally, the output power of a TENG reaches the maximum in a particular condition, which is called cycles for maximum energy output (CMEO).

Fundamentally, FOM_P is expressed as

$$FOM_P = FOM_S \cdot FOM_M \tag{5.2}$$

where FOM_S is the stucture figure-of-merit and FOM_M is the material figure-of-merit.

- Material figure-of-merit

It is obvious that the evaluation of the TENG's output is from two aspects: triboelectric material and structure of the TENG. For a TENG with a certain structure, the only determinant of the output power is the FOM_M, which is defined as

$$FOM_M = \sigma^2 \tag{5.3}$$

where σ is the surface charge density.

- Structure figure-of-merit

When the triboelectric pair is determined, the FOM_S is the only determinant and is defined as

$$FOM_S = \frac{2\varepsilon_0}{\sigma^2}\frac{E_m}{Ax_{max}} \tag{5.4}$$

where ε_0 is the vacuum dielectric constant, A is the contact area and x_{max} is the maximum separation between the triboelectric pair. For a certain TENG and external mechanical load (assuming the surface charges on a triboelectric material have already been saturated), the ideal maximum output power (E_m) in one cycle is defined as

$$E_m = \frac{1}{2}Q_{SC,max}(V_{OC,max} + V'_{max}) \tag{5.5}$$

where $Q_{SC,max}$ is the maximum short-circuit transferred charges, $V_{OC,max}$ is the maximum open-circuit voltage and V'_{max} is the maximum output voltage for the TENG.

5.3 Optimization methods of the μTEH

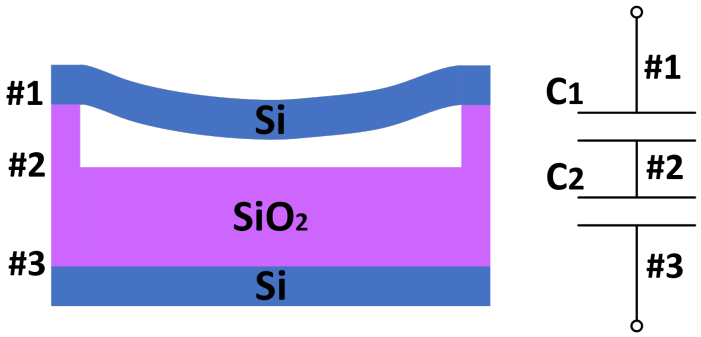

Figure 5.9: The basic structure of the μTEH and the corresponding equivalent circuit.

Based on the abovementioned figure-of-merit, optimization methods are proposed particularly for the μTEH in this section. In the case of the μTEH, the vertical contact-separation working mode and the corresponding equivalent circuit are illustrated in Fig. 5.9. The μTEH can be modeled as a series of two capacitors in the equivalent circuit. Based on the theories in Chapter 2, the relevant parameters are expressed as follows

$$V_{OC,max} = \frac{A\sigma}{C_1(x_{max})} \tag{5.6}$$

$$Q_{SC,max} = \sigma A \frac{C_2}{C_1(x_max) + C_2} \tag{5.7}$$

$$V'_{max} = \frac{\sigma A}{C_1(x_{max}) + C_2} \tag{5.8}$$

In terms of the μTEH, the membrane size is much larger than the cavity depth. Thus, both C_1 and C_2 can be calculated based on the theory of parallel-plate capacitor.

$$C_1 = \frac{A}{\varepsilon_0 x_{max}} \tag{5.9}$$

$$C_2 = \frac{A}{\varepsilon_1 t_{oxide}} \tag{5.10}$$

where ε_1 and t_{oxide} are the dielectric constant and the thickness of the silicon oxide layer.

5.3.1 Geometry

The geometry of the μTEH can affect the mechanical loading, further affecting the output performance of the μTEH. Hence, it deserves to comprehensively explore the effect of μTEH's geometry. In this theoretical analysis, we are still targeting the bio-applications so that the working frequency is still set as 1 MHz. The triboelectric pair and fabrication method are also same as that in chapter 4.

When the triboelectric materials are determined, the key parameters affecting the resonant frequency and the mechanical behaviors are the size and the thickness of the membrane. Since the fusion bonding technique is based on the SOI wafer, the thickness of the membrane is highly dependent on the availability of the commercial SOI wafer. Currently, SOI manufacturers have abandoned the production line of the 4-inch wafer with sub-micrometer device layer. The thinnest device layer of the SOI wafer we can purchase is 2 μm thick. Therefore, the range of the thickness starts from 2 μm. According to Eq. 4.3 and 4.15, the resonant frequencies and the maximum static displacement under the atmospheric pressure of the membrane are shown in Fig. 5.10.

To keep the consistent resonant frequency (1 MHz), a thinner membrane corresponds to a smaller size and a larger maximum static displacement. Table 5.2 gives calculated maximum static displacement for nine combinations of thickness and size.

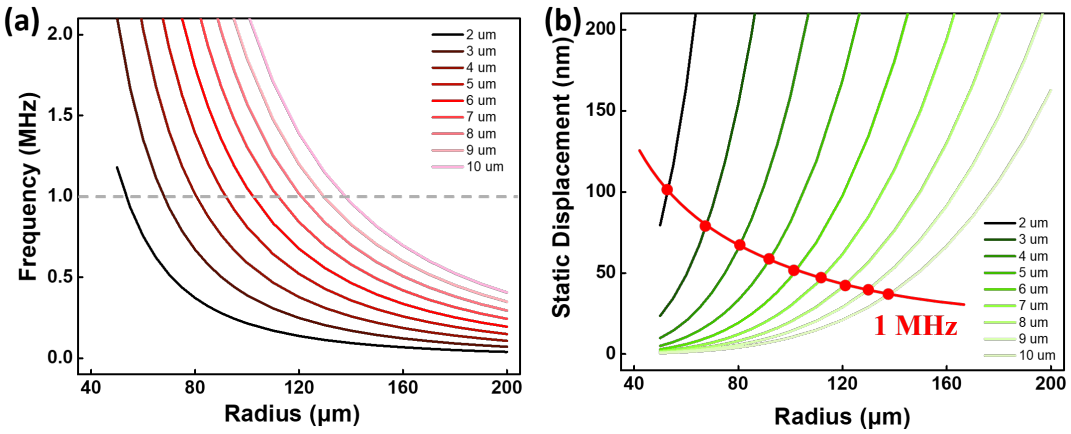

Figure 5.10: The dependence of the (a) resonant frequency and (b) the maximum displacement on the size of the membrane.

Table 5.2: The requirements for water in the electronics and semiconductor industries.

Thickness (μm)	Radius (μm)	Max static displacement (nm)
2	53	100.2555
3	68	80.4946
4	80	65.0541
5	92	58.2554
6	102	50.938
7	112	46.6308
8	121	42.5565
9	129	38.6123
10	138	36.8647

Based on the 3D COMSOL model in chapter 4, the dynamic behaviors of different combinations were simulated (shown in Fig. 5.11). It is seen that a thinner membrane results in a larger dynamic displacement at resonance. For a given gap depth, the contact between the membrane and the substrate will be more sufficient (larger contact area) for a thinner membrane. Much literature has concluded that sufficient contact will give a higher output power because of higher surface charge density [64, 65, 161, 162]. Thus, thinner membrane can potentially contribute to higher output power.

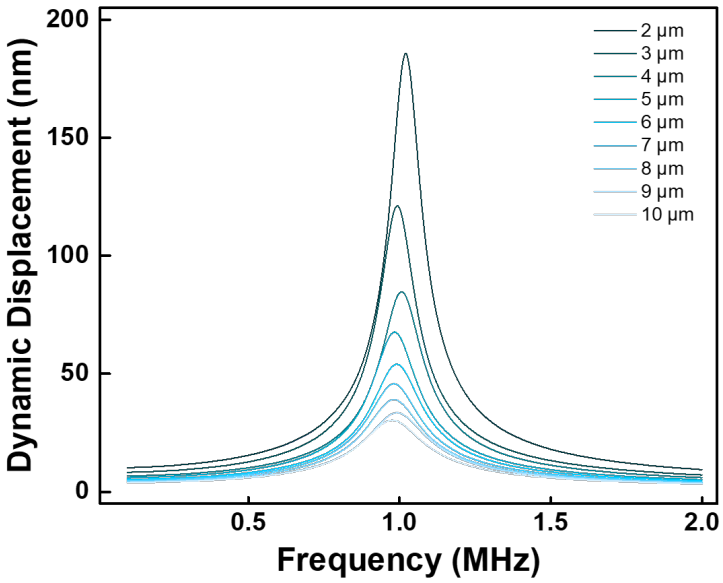

Figure 5.11: The dynamic behavior of the membrane for different thickness.

Then, the FOM_S is calculated to evaluate the effect of the geometry on the output. From Fig. 5.11 and Table 5.2, the dynamic displacement of the membrane is comparable to the static displacement, so that the x_{max} is reasonably approximated as the cavity depth of the cavity. Other required parameters in the calculation are listed in Table 5.3.

Table 5.3: The required parameters for analysis

Parameter	Quantity
Radius of membrane	50 μm
Surface charge density	10e-6 C/m^2
Relative permittivity of silicon oxide	3.8

Based on the Eq. 5.4, the relationship between the FOM_s and the x_{max} for the μTEH is illustrated in Fig. 5.12. Generally, the FOM_S increases as the x_{max} increases, indicating that large cavity depth is beneficial to improving the output power. Moreover, Fig. 5.12 reports that a thinner dielectric layer will also improve the FOM_s.

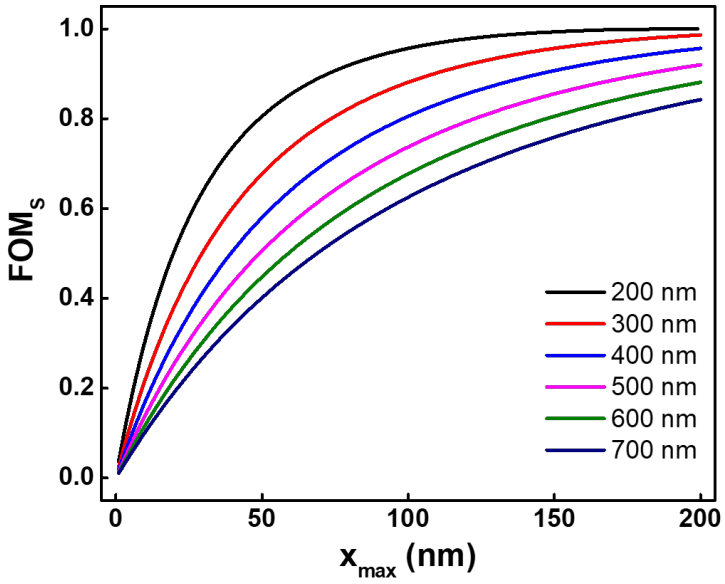

Figure 5.12: The relationship between the FOM$_s$ and the x$_{max}$ for the μTEH with different thickness of silicon oxide layer.

5.3.2 Materials

According to Eq. 5.3, surface charge density is the only factor determining the material figure-of-merit. Additionally, the quadratic relationship indicates that the surface charge density has a significant effect on the performance of the TENG. In some degree, the surface charge density plays the most important role in the output of the TENG. To enhance the surface charge density, the triboelectric pair is usually select as far as possible in the triboelectric series. In the current design of the μTEH, the selection of silicon and silicon oxide is more because of the fabrication concerns. To meet the requirements of the fusion bonding, the output performance of the μTEH is partly sacrificed.

Until now, choosing the triboelectric pair is highly dependent on the experience and specific applications. Trial-and-error method is currently the most prevailing and effective way to determine the triboelectric pair. The vast majority of the reported TENGs use polymers

as triboelectric materials, such as PTFE and PDMS and nylon, because these polymers are located at the most negative end of the triboelectric series. Previous studies have already exhibited the excellent potential of polymer-based TENG for acoustic energy harvesting and sensing [66, 161–163]. The introduction of the polymer layer is expected to dramatically increase the surface charge density and improve the output power of the μTEH.

However, an important point to note is that polymers are not compatible with the fusion bonding technique. Adhesive wafer bonding technique is a good alternative to the fusion bonding technique. Therefore, the fabrication process based on adhesive wafer bonding should be in investigated in the future [130, 164].

5.4 Chapter conclusion

This chapter demonstrated a prototyped AET system based on the μTEH. Under 1 MHZ, 132 mW/cm^2 incident acoustic power, the output power on the load resistor can reach up to 50 nW. Up till now, very few reported AET systems were based on the MEMS energy harvester, especially for bio-applications. Overall, the output of the MEMS energy harvester is low (tens of nW to several μW). The development of the TENG is still in the very early stage at present. Although the current output of the μTEH is low, there is a huge space for the improvement. Optimization methodologies, in the aspects of structure design and material selection, were proposed in this chapter to improve the output of the μTEH and adhesive wafer bonding is expected as a promising way to fabricate the μTEH in the future. In addition, pulse experiments demonstrated the μTEH's potential of wireless communication via the ultrasound link.

Chapter 6

Summary and future work

6.1 Summary

As an emerging technology, TENG gives us another new method to collect mechanical energy and convert to electrical energy. Novel strategies for self-powered sensing and energy harvesting based on TENG were proposed in this thesis.

A self-powered on-line ion concentration monitoring system based on TENG was developed for the first time. Ion concentration is an important criterion to evaluate the water quality in the industry. Based on TENG, a self-powered ion concentration sensing system was proposed to realize water quality monitoring in real time. An RD-TENG was designed and manufactured, based on industrial PCB technology. Different from handcrafted TENG, sophisticated and dense electrode structures can be patterned by PCB technology. Therefore, a higher and more reliable output signal can be achieved, leading to a higher sensitivity. By converting the mechanical energy of flowing water in the pipeline to electrical energy, the RD-TENG worked as an energy source to power the ion concentration sensor, which was also fabricated by PCB technology. Working under the freestanding triboelectric-layer mode, copper and PTFE were adopted as a triboelectric pair to maximize the output signal. The open-circuit voltage and short-circuit current of the RD-TENG can reach up to 210 V_{P-P} and 112 μA, respectively. The

sensing mechanism of the self-powered sensing system is based on the impedance matching between the RD-TENG and the ion concentration sensor. When the rotation speed is less than 250 rpm, the ion concentration sensor shows a pure resistance property in the water, which makes the construction of the sensing system much easier. By connecting the RD-TENG, ion concentration sensor and a fixed resistor (150 kΩ) in series, an alarming circuit was designed for real-time ion concentration monitoring. The monitoring system can achieve the LOD of NaCl 1.52×10^{-5} mol/L and the response time in the scale of milliseconds.

A theoretical basis was also proposed for the frequency-independent sensing based on the capacitive impedance matching between TENG and capacitance-type sensor. Currently, most reported self-powered sensing systems are based on the resistive impedance matching between TENG and resistance-type sensor. By experimentally and theoretically studying the output of the RD-TENG with load impedance, it is revealed that the relationship between the output voltage and the load resistance has a frequency dependence while the relationship between the output voltage and the load capacitance has no frequency dependence. Hence, the sensing performance of a capacitance-type sensor will not be affected by the mechanical load.

A micro- triboelectric energy harvester (μTEH) was successfully fabricated based on MEMS technologies for the first time. The vast majority of the reported TENGs are fabricated by hand at present. This fabrication method has a lot of drawbacks, such as bulky size, huge performance variation among devices, poor reliability and *etc*. The utilization of PCB technology makes the fabrication of the TENG more standard and more reliable. It is crucial for TENG's commercialization in the future. However, further miniaturization and higher integration are desired in bio-applications, such as energy harvesting for implanted devices. A μTEH was developed by virtue of the MEMS technologies. Targeting acoustic energy transferring for implanted devices, 1 MHz was selected as the working frequency as a compromise of the acoustic

attenuation and mechanical damage. The μTEH works under the vertical contact-separation mode, where silicon and wet thermal oxide function as a triboelectric pair. SKPM measurements were performed to the silicon and the wet thermal oxide to unveil the mechanism of the triboelectrification between them. Taking advantage of the SOI's device layer and fusion bonding technique, vacuum cavities were formed underneath the silicon membrane (2 μm thick). Based on the analytical calculation and FEM simulation, the maximum static displacement of the silicon membrane induced by the atmospheric pressure was approximately 74.5 nm. Then, the actual depth of the cavity was 90 ± 10 nm to ensure the triboelectrification.

Potential applications of the μTEH were demonstrated. In the vegetable oil, the μTEH can achieve the open-circuit voltage of ~15.5 V_{P-P} under 63 kPa acoustic pressure (1 MHz). A linear relationship between the peak open-circuit voltage and the incident acoustic pressure was also observed. When connecting a load resistor with the μTEH, it can output maximally 50 nW power under 1MHz, 132 mW/cm^2 incident acoustic power. Although the value is fairly low compared to piezo transducer-based energy harvesters, it can be argued that the performance of this μTEH is sacrificed to compromise with the fusion bonding technique. According to chapter 5, the selection of the triboelectric pair has the most significant effect on the output of the TENG. Yet, silicon and wet thermal oxide is not perfect selection. In the future, introducing a polymer thin film with adhesive wafer bonding technique is expected to dramatically increase the output power of the μTEH. Additionally, standing wave effect was also observed during the experiments. Pulse experiments were performed and the SNR of the μTEH can reach 20.54 dB. The results indicate that the μTEH has the promising potential for wireless data communication by ASK modulation.

Lastly, optimization methodologies were proposed to improve the output of the μTEH in the future. By introducing the figure-of-merit (FOM) to the μTEH, it was concluded that thinner

membrane and thinner dielectric layer can result in a higher output. More importantly, it is revealed that the change of the triboelectric pair is the most effective way to improve the output of the μTEH. In particular, this research opened up a new field and laid a good groundwork for designing the MEMS TENG devices.

6.2 Contributions

The first contribution is that a self-powered ion concentration monitoring system, where both the sensor and the TENG were fabricated by mature printed circuit board (PCB) technology, was developed based on the impedance matching effect of TENG. A comprehensive study of the impedance matching effect of the TENG was performed. This work further promotes the understanding of the working principles of TENG, particularly the frequency dependence of impedance matching effect in aqueous solution.

The second contribution is the development of a novel triboelectric energy harvester based on MEMS technologies. This is the very first MEMS TENG in the world. The working mechanism, structure design and fabrication process were explored. Particularly, a novel wafer-bonding-based fabrication method of TENG was proposed. MEMS technologies dramatically miniaturize the size of TENG and greatly improves its compatibility with other electronics.

The third contribution is that TENG is firstly adopted in the ultrasound-related applications. Compared to acoustic energy harvesting in the audible frequency range [64–66], this work broadened the application of TENG, especially in the in-immersion applications.

The last contribution is that the optimization methodologies of the MEMS TENG were proposed to improve the output in the future. This work can guide not only the geometry design but also the material choices of the MEMS TENG.

6.3 Future work

Currently, the study of TENG is still at the primary stage and a lot of work can be done to explore new territories or improve the performance of existing TENGs. From the view of engineering, several directions to extend the related research are proposed here based on the work in this thesis.

- Self-powered ion concentration sensing

Selectivity is also an important criterion of a sensing system. In the practical application of ion concentration sensing, the aqueous environment is complicated. Proper coating materials can be developed and coated on the surface of electrodes to selectively monitor the water quality.

Reliable packaging techniques are highly required, especially in the aqueous environment. Since most TENGs contain moving parts inside, it is challenging to isolate the TENG from the outer environment for a stable output. A lot of effort needs to be done in this respect.

A new configuration of TENG based on liquid–solid contact electrification [165, 166] will be explored in the future to overcome the wearing issue of triboelectric materials, as well as the packaging problem. When water slides the inner surface of the pipe, water and the pipe will be oppositely charged by the contact electrification. According to this mechanism, single-electrode mode and freestanding mode TENGs can be constructed for energy generation. Other than the wearing issue, this new structure may also dramatically miniaturize the sensing system because of the elimination of mechanical moving parts.

In this thesis, is has been proved that the capacitive impedance matching of TENG is independent on the frequency of the mechanical load, which is a good point for frequency-

independent sensing applications. In the future, the integration between TENG and capacitance-type sensors will be a good direction to pursue.

- Micro- triboelectric energy harvester

In chapter 5, several optimization methods are proposed in the respects of structure and materials. Among the optimization methods, improvement of the surface charge density is the most key point to improve the efficiency. Therefore, increasing the contact area and change of the triboelectric pair are expected as the most effective way to improve the output of the μTEH. Hence, μTEH based on adhesive bonding technology is a valuable research direction in the future.

Packaging is also an issue for the μTEH. Since silicon is not a bio-compatible material, proper packaging material is needed if we want to apply the μTEH for powering implanted devices.

This thesis only focused on the development of the μTEH and did not consider too much the electric circuit. In reality, energy loss in the circuit is also an important concern, especially for the high-frequency circuit. Impedance matching circuit should also be designed to minimize this loss. Indeed, circuit design and the post data process are also important particularly for the application of wireless communication. Therefore, a lot of work on the circuit can be done in the future.

Copyright permissions

RightsLink®

Home | Account Info | Help

Title: Self-Powered Triboelectric Nanosensor with Poly(tetrafluoroethylene) Nanoparticle Arrays for Dopamine Detection

Author: Yang Jie, Ning Wang, Xia Cao, et al

Publication: ACS Nano

Publisher: American Chemical Society

Date: Aug 1, 2015

Logged in as:
CHEN CHEN
LOGOUT

PERMISSION/LICENSE IS GRANTED FOR YOUR ORDER AT NO CHARGE

This type of permission/license, instead of the standard Terms & Conditions, is sent to you because no fee is being charged for your order. Please note the following:

- Permission is granted for your request in both print and electronic formats, and translations.
- If figures and/or tables were requested, they may be adapted or used in part.
- Please print this page for your records and send a copy of it to your publisher/graduate school.
- Appropriate credit for the requested material should be given as follows: "Reprinted (adapted) with permission from (COMPLETE REFERENCE CITATION). Copyright (YEAR) American Chemical Society." Insert appropriate information in place of the capitalized words.
- One-time permission is granted only for the use specified in your request. No additional uses are granted (such as derivative works or other editions). For any other uses, please submit a new request.

If credit is given to another source for the material you requested, permission must be obtained from that source.

BACK CLOSE WINDOW

Title: Integrating a Silicon Solar Cell with a Triboelectric Nanogenerator via a Mutual Electrode for Harvesting Energy from Sunlight and Raindrops

Author: Yuqiang Liu, Na Sun, Jiawei Liu, et al

Publication: ACS Nano

Publisher: American Chemical Society

Date: Mar 1, 2018

PERMISSION/LICENSE IS GRANTED FOR YOUR ORDER AT NO CHARGE

This type of permission/license, instead of the standard Terms & Conditions, is sent to you because no fee is being charged for your order. Please note the following:

- Permission is granted for your request in both print and electronic formats, and translations.
- If figures and/or tables were requested, they may be adapted or used in part.
- Please print this page for your records and send a copy of it to your publisher/graduate school.
- Appropriate credit for the requested material should be given as follows: "Reprinted (adapted) with permission from (COMPLETE REFERENCE CITATION). Copyright (YEAR) American Chemical Society." Insert appropriate information in place of the capitalized words.
- One-time permission is granted only for the use specified in your request. No additional uses are granted (such as derivative works or other editions). For any other uses, please submit a new request.

Title: Liquid-Metal-Based Super-Stretchable and Structure-Designable Triboelectric Nanogenerator for Wearable Electronics

Author: Yanqin Yang, Na Sun, Zhen Wen, et al

Publication: ACS Nano

Publisher: American Chemical Society

Date: Feb 1, 2018

PERMISSION/LICENSE IS GRANTED FOR YOUR ORDER AT NO CHARGE

This type of permission/license, instead of the standard Terms & Conditions, is sent to you because no fee is being charged for your order. Please note the following:

- Permission is granted for your request in both print and electronic formats, and translations.
- If figures and/or tables were requested, they may be adapted or used in part.
- Please print this page for your records and send a copy of it to your publisher/graduate school.
- Appropriate credit for the requested material should be given as follows: "Reprinted (adapted) with permission from (COMPLETE REFERENCE CITATION). Copyright (YEAR) American Chemical Society." Insert appropriate information in place of the capitalized words.
- One-time permission is granted only for the use specified in your request. No additional uses are granted (such as derivative works or other editions). For any other uses, please submit a new request.

If credit is given to another source for the material you requested, permission must be obtained from that source.

Home | Account Info | Help

Title:	Personalized Keystroke Dynamics for Self-Powered Human–Machine Interfacing
Author:	Jun Chen, Guang Zhu, Jin Yang, et al
Publication:	ACS Nano
Publisher:	American Chemical Society
Date:	Jan 1, 2015

Logged in as:
CHEN CHEN
Account #: 3001453676

LOGOUT

PERMISSION/LICENSE IS GRANTED FOR YOUR ORDER AT NO CHARGE

This type of permission/license, instead of the standard Terms & Conditions, is sent to you because no fee is being charged for your order. Please note the following:

- Permission is granted for your request in both print and electronic formats, and translations.
- If figures and/or tables were requested, they may be adapted or used in part.
- Please print this page for your records and send a copy of it to your publisher/graduate school.
- Appropriate credit for the requested material should be given as follows: "Reprinted (adapted) with permission from (COMPLETE REFERENCE CITATION). Copyright (YEAR) American Chemical Society." Insert appropriate information in place of the capitalized words.
- One-time permission is granted only for the use specified in your request. No additional uses are granted (such as derivative works or other editions). For any other uses, please submit a new request.

If credit is given to another source for the material you requested, permission must be obtained from that source.

BACK | CLOSE WINDOW

Title: Triboelectrification-Based Organic Film Nanogenerator for Acoustic Energy Harvesting and Self-Powered Active Acoustic Sensing

Author: Jin Yang, Jun Chen, Ying Liu, et al

Publication: ACS Nano

Publisher: American Chemical Society

Date: Mar 1, 2014

PERMISSION/LICENSE IS GRANTED FOR YOUR ORDER AT NO CHARGE

This type of permission/license, instead of the standard Terms & Conditions, is sent to you because no fee is being charged for your order. Please note the following:

- Permission is granted for your request in both print and electronic formats, and translations.
- If figures and/or tables were requested, they may be adapted or used in part.
- Please print this page for your records and send a copy of it to your publisher/graduate school.
- Appropriate credit for the requested material should be given as follows: "Reprinted (adapted) with permission from (COMPLETE REFERENCE CITATION). Copyright (YEAR) American Chemical Society." Insert appropriate information in place of the capitalized words.
- One-time permission is granted only for the use specified in your request. No additional uses are granted (such as derivative works or other editions). For any other uses, please submit a new request.

If credit is given to another source for the material you requested, permission must be obtained from that source.

JOHN WILEY AND SONS LICENSE TERMS AND CONDITIONS

May 14, 2019

This Agreement between Chen Chen ("You") and John Wiley and Sons ("John Wiley and Sons") consists of your license details and the terms and conditions provided by John Wiley and Sons and Copyright Clearance Center.

License Number	4587961075261
License date	May 14, 2019
Licensed Content Publisher	John Wiley and Sons
Licensed Content Publication	Advanced Functional Materials
Licensed Content Title	Self-Powered Vehicle Emission Testing System Based on Coupling of Triboelectric and Chemoresistive Effects
Licensed Content Author	Qingqing Shen, Xinkai Xie, Mingfa Peng, et al
Licensed Content Date	Dec 15, 2017
Licensed Content Volume	28
Licensed Content Issue	10
Licensed Content Pages	8
Type of use	Dissertation/Thesis
Requestor type	University/Academic
Format	Electronic
Portion	Figure/table
Number of figures/tables	1
Original Wiley figure/table number(s)	Figure 1
Will you be translating?	No
Title of your thesis / dissertation	Development of Triboelectric Devices for Self-powered Sensing And Energy Harvesting Applications
Expected completion date	Aug 2019
Expected size (number of pages)	150
Requestor Location	Chen Chen 200 University Avenue West Waterloo, ON N2L 3G1 Canada Attn: Chen Chen
Publisher Tax ID	EU826007151
Total	0.00 CAD
Terms and Conditions	

TERMS AND CONDITIONS

This copyrighted material is owned by or exclusively licensed to John Wiley & Sons, Inc. or one of its group companies (each a"Wiley Company") or handled on behalf of a society with

JOHN WILEY AND SONS LICENSE TERMS AND CONDITIONS

May 14, 2019

This Agreement between Chen Chen ("You") and John Wiley and Sons ("John Wiley and Sons") consists of your license details and the terms and conditions provided by John Wiley and Sons and Copyright Clearance Center.

License Number	4587970260610
License date	May 14, 2019
Licensed Content Publisher	John Wiley and Sons
Licensed Content Publication	Advanced Materials Technologies
Licensed Content Title	Impedance Matching Effect between a Triboelectric Nanogenerator and a Piezoresistive Pressure Sensor Induced Self-Powered Weighing
Licensed Content Author	Xinkai Xie, Zhen Wen, Qingqing Shen, et al
Licensed Content Date	Apr 23, 2018
Licensed Content Volume	3
Licensed Content Issue	6
Licensed Content Pages	7
Type of use	Dissertation/Thesis
Requestor type	University/Academic
Format	Electronic
Portion	Figure/table
Number of figures/tables	1
Original Wiley figure/table number(s)	Figure 5
Will you be translating?	No
Title of your thesis / dissertation	Development of Triboelectric Devices for Self-powered Sensing And Energy Harvesting Applications
Expected completion date	Aug 2019
Expected size (number of pages)	150
Requestor Location	Chen Chen 200 University Avenue West Waterloo, ON N2L 3G1 Canada Attn: Chen Chen
Publisher Tax ID	EU826007151
Total	0.00 CAD
Terms and Conditions	

TERMS AND CONDITIONS

This copyrighted material is owned by or exclusively licensed to John Wiley & Sons, Inc. or one of its group companies (each a"Wiley Company") or handled on behalf of a society with

ELSEVIER LICENSE
TERMS AND CONDITIONS

May 14, 2019

This Agreement between Chen Chen ("You") and Elsevier ("Elsevier") consists of your license details and the terms and conditions provided by Elsevier and Copyright Clearance Center.

License Number	4587971465939
License date	May 14, 2019
Licensed Content Publisher	Elsevier
Licensed Content Publication	Nano Energy
Licensed Content Title	Largely enhanced triboelectric nanogenerator for efficient harvesting of water wave energy by soft contacted structure
Licensed Content Author	Ping Cheng,Hengyu Guo,Zhen Wen,Chunlei Zhang,Xing Yin,Xinyuan Li,Di Liu,Weixing Song,Xuhui Sun,Jie Wang,Zhong Lin Wang
Licensed Content Date	Mar 1, 2019
Licensed Content Volume	57
Licensed Content Issue	n/a
Licensed Content Pages	8
Start Page	432
End Page	439
Type of Use	reuse in a thesis/dissertation
Intended publisher of new work	other
Portion	figures/tables/illustrations
Number of figures/tables/illustrations	1
Format	electronic
Are you the author of this Elsevier article?	No
Will you be translating?	No
Original figure numbers	Figure 1
Title of your thesis/dissertation	Development of Triboelectric Devices for Self-powered Sensing And Energy Harvesting Applications
Expected completion date	Aug 2019
Estimated size (number of pages)	150
Requestor Location	Chen Chen 200 University Avenue West Waterloo, ON N2L 3G1 Canada Attn: Chen Chen
Publisher Tax ID	GB 494 6272 12

THE AMERICAN ASSOCIATION FOR THE ADVANCEMENT OF SCIENCE LICENSE TERMS AND CONDITIONS

May 15, 2019

This Agreement between Chen Chen ("You") and The American Association for the Advancement of Science ("The American Association for the Advancement of Science") consists of your license details and the terms and conditions provided by The American Association for the Advancement of Science and Copyright Clearance Center.

License Number	4590010313800
License date	May 15, 2019
Licensed Content Publisher	The American Association for the Advancement of Science
Licensed Content Publication	Science Robotics
Licensed Content Title	A highly sensitive, self-powered triboelectric auditory sensor for social robotics and hearing aids
Licensed Content Author	Hengyu Guo,Xianjie Pu,Jie Chen,Yan Meng,Min-Hsin Yeh,Guanlin Liu,Qian Tang,Baodong Chen,Di Liu,Song Qi,Changsheng Wu,Chenguo Hu,Jie Wang,Zhong Lin Wang
Licensed Content Date	Jul 25, 2018
Licensed Content Volume	3
Licensed Content Issue	20
Volume number	3
Issue number	20
Type of Use	Thesis / Dissertation
Requestor type	Scientist/individual at a research institution
Format	Print and electronic
Portion	Figure
Number of figures/tables	1
Order reference number	
Title of your thesis / dissertation	Development of Triboelectric Devices for Self-powered Sensing And Energy Harvesting Applications
Expected completion date	Aug 2019
Estimated size(pages)	150
Requestor Location	Chen Chen 200 University Avenue West Waterloo, ON N2L 3G1 Canada Attn: Chen Chen
Total	0.00 CAD
Terms and Conditions	

American Association for the Advancement of Science TERMS AND CONDITIONS
Regarding your request, we are pleased to grant you non-exclusive, non-transferable permission, to republish the AAAS material identified above in your work identified above,

ELSEVIER LICENSE
TERMS AND CONDITIONS

May 14, 2019

This Agreement between Chen Chen ("You") and Elsevier ("Elsevier") consists of your license details and the terms and conditions provided by Elsevier and Copyright Clearance Center.

License Number	4587961307878
License date	May 14, 2019
Licensed Content Publisher	Elsevier
Licensed Content Publication	Nano Energy
Licensed Content Title	Self-powered ammonia nanosensor based on the integration of the gas sensor and triboelectric nanogenerator
Licensed Content Author	Siwen Cui,Youbin Zheng,Tingting Zhang,Daoai Wang,Feng Zhou,Weimin Liu
Licensed Content Date	Jul 1, 2018
Licensed Content Volume	49
Licensed Content Issue	n/a
Licensed Content Pages	9
Start Page	31
End Page	39
Type of Use	reuse in a thesis/dissertation
Intended publisher of new work	other
Portion	figures/tables/illustrations
Number of figures/tables/illustrations	1
Format	electronic
Are you the author of this Elsevier article?	No
Will you be translating?	No
Original figure numbers	Figure 8
Title of your thesis/dissertation	Development of Triboelectric Devices for Self-powered Sensing And Energy Harvesting Applications
Expected completion date	Aug 2019
Estimated size (number of pages)	150
Requestor Location	Chen Chen 200 University Avenue West Waterloo, ON N2L 3G1 Canada Attn: Chen Chen
Publisher Tax ID	GB 494 6272 12

Total 0.00 CAD

Terms and Conditions

INTRODUCTION

1. The publisher for this copyrighted material is Elsevier. By clicking "accept" in connection with completing this licensing transaction, you agree that the following terms and conditions apply to this transaction (along with the Billing and Payment terms and conditions established by Copyright Clearance Center, Inc. ("CCC"), at the time that you opened your Rightslink account and that are available at any time at http://myaccount.copyright.com).

GENERAL TERMS

2. Elsevier hereby grants you permission to reproduce the aforementioned material subject to the terms and conditions indicated.
3. Acknowledgement: If any part of the material to be used (for example, figures) has appeared in our publication with credit or acknowledgement to another source, permission must also be sought from that source. If such permission is not obtained then that material may not be included in your publication/copies. Suitable acknowledgement to the source must be made, either as a footnote or in a reference list at the end of your publication, as follows:
"Reprinted from Publication title, Vol /edition number, Author(s), Title of article / title of chapter, Pages No., Copyright (Year), with permission from Elsevier [OR APPLICABLE SOCIETY COPYRIGHT OWNER]." Also Lancet special credit - "Reprinted from The Lancet, Vol. number, Author(s), Title of article, Pages No., Copyright (Year), with permission from Elsevier."
4. Reproduction of this material is confined to the purpose and/or media for which permission is hereby given.
5. Altering/Modifying Material: Not Permitted. However figures and illustrations may be altered/adapted minimally to serve your work. Any other abbreviations, additions, deletions and/or any other alterations shall be made only with prior written authorization of Elsevier Ltd. (Please contact Elsevier at permissions@elsevier.com). No modifications can be made to any Lancet figures/tables and they must be reproduced in full.
6. If the permission fee for the requested use of our material is waived in this instance, please be advised that your future requests for Elsevier materials may attract a fee.
7. Reservation of Rights: Publisher reserves all rights not specifically granted in the combination of (i) the license details provided by you and accepted in the course of this licensing transaction, (ii) these terms and conditions and (iii) CCC's Billing and Payment terms and conditions.
8. License Contingent Upon Payment: While you may exercise the rights licensed immediately upon issuance of the license at the end of the licensing process for the transaction, provided that you have disclosed complete and accurate details of your proposed use, no license is finally effective unless and until full payment is received from you (either by publisher or by CCC) as provided in CCC's Billing and Payment terms and conditions. If full payment is not received on a timely basis, then any license preliminarily granted shall be deemed automatically revoked and shall be void as if never granted. Further, in the event that you breach any of these terms and conditions or any of CCC's Billing and Payment terms and conditions, the license is automatically revoked and shall be void as if never granted. Use of materials as described in a revoked license, as well as any use of the materials beyond the scope of an unrevoked license, may constitute copyright infringement and publisher reserves the right to take any and all action to protect its copyright in the materials.
9. Warranties: Publisher makes no representations or warranties with respect to the licensed material.
10. Indemnity: You hereby indemnify and agree to hold harmless publisher and CCC, and their respective officers, directors, employees and agents, from and against any and all

claims arising out of your use of the licensed material other than as specifically authorized pursuant to this license.
11. No Transfer of License: This license is personal to you and may not be sublicensed, assigned, or transferred by you to any other person without publisher's written permission.
12. No Amendment Except in Writing: This license may not be amended except in a writing signed by both parties (or, in the case of publisher, by CCC on publisher's behalf).
13. Objection to Contrary Terms: Publisher hereby objects to any terms contained in any purchase order, acknowledgment, check endorsement or other writing prepared by you, which terms are inconsistent with these terms and conditions or CCC's Billing and Payment terms and conditions. These terms and conditions, together with CCC's Billing and Payment terms and conditions (which are incorporated herein), comprise the entire agreement between you and publisher (and CCC) concerning this licensing transaction. In the event of any conflict between your obligations established by these terms and conditions and those established by CCC's Billing and Payment terms and conditions, these terms and conditions shall control.
14. Revocation: Elsevier or Copyright Clearance Center may deny the permissions described in this License at their sole discretion, for any reason or no reason, with a full refund payable to you. Notice of such denial will be made using the contact information provided by you. Failure to receive such notice will not alter or invalidate the denial. In no event will Elsevier or Copyright Clearance Center be responsible or liable for any costs, expenses or damage incurred by you as a result of a denial of your permission request, other than a refund of the amount(s) paid by you to Elsevier and/or Copyright Clearance Center for denied permissions.

LIMITED LICENSE

The following terms and conditions apply only to specific license types:
15. **Translation**: This permission is granted for non-exclusive world **English** rights only unless your license was granted for translation rights. If you licensed translation rights you may only translate this content into the languages you requested. A professional translator must perform all translations and reproduce the content word for word preserving the integrity of the article.
16. **Posting licensed content on any Website**: The following terms and conditions apply as follows: Licensing material from an Elsevier journal: All content posted to the web site must maintain the copyright information line on the bottom of each image; A hyper-text must be included to the Homepage of the journal from which you are licensing at http://www.sciencedirect.com/science/journal/xxxxx or the Elsevier homepage for books at http://www.elsevier.com; Central Storage: This license does not include permission for a scanned version of the material to be stored in a central repository such as that provided by Heron/XanEdu.
Licensing material from an Elsevier book: A hyper-text link must be included to the Elsevier homepage at http://www.elsevier.com . All content posted to the web site must maintain the copyright information line on the bottom of each image.

Posting licensed content on Electronic reserve: In addition to the above the following clauses are applicable: The web site must be password-protected and made available only to bona fide students registered on a relevant course. This permission is granted for 1 year only. You may obtain a new license for future website posting.
17. **For journal authors:** the following clauses are applicable in addition to the above:
Preprints:
A preprint is an author's own write-up of research results and analysis, it has not been peer-reviewed, nor has it had any other value added to it by a publisher (such as formatting, copyright, technical enhancement etc.).
Authors can share their preprints anywhere at any time. Preprints should not be added to or enhanced in any way in order to appear more like, or to substitute for, the final versions of

articles however authors can update their preprints on arXiv or RePEc with their Accepted Author Manuscript (see below).
If accepted for publication, we encourage authors to link from the preprint to their formal publication via its DOI. Millions of researchers have access to the formal publications on ScienceDirect, and so links will help users to find, access, cite and use the best available version. Please note that Cell Press, The Lancet and some society-owned have different preprint policies. Information on these policies is available on the journal homepage.
Accepted Author Manuscripts: An accepted author manuscript is the manuscript of an article that has been accepted for publication and which typically includes author-incorporated changes suggested during submission, peer review and editor-author communications.
Authors can share their accepted author manuscript:

- immediately
  - via their non-commercial person homepage or blog
  - by updating a preprint in arXiv or RePEc with the accepted manuscript
  - via their research institute or institutional repository for internal institutional uses or as part of an invitation-only research collaboration work-group
  - directly by providing copies to their students or to research collaborators for their personal use
  - for private scholarly sharing as part of an invitation-only work group on commercial sites with which Elsevier has an agreement
- After the embargo period
  - via non-commercial hosting platforms such as their institutional repository
  - via commercial sites with which Elsevier has an agreement

In all cases accepted manuscripts should:

- link to the formal publication via its DOI
- bear a CC-BY-NC-ND license - this is easy to do
- if aggregated with other manuscripts, for example in a repository or other site, be shared in alignment with our hosting policy not be added to or enhanced in any way to appear more like, or to substitute for, the published journal article.

Published journal article (JPA): A published journal article (PJA) is the definitive final record of published research that appears or will appear in the journal and embodies all value-adding publishing activities including peer review co-ordination, copy-editing, formatting, (if relevant) pagination and online enrichment.
Policies for sharing publishing journal articles differ for subscription and gold open access articles:
Subscription Articles: If you are an author, please share a link to your article rather than the full-text. Millions of researchers have access to the formal publications on ScienceDirect, and so links will help your users to find, access, cite, and use the best available version.
Theses and dissertations which contain embedded PJAs as part of the formal submission can be posted publicly by the awarding institution with DOI links back to the formal publications on ScienceDirect.
If you are affiliated with a library that subscribes to ScienceDirect you have additional private sharing rights for others' research accessed under that agreement. This includes use for classroom teaching and internal training at the institution (including use in course packs and courseware programs), and inclusion of the article for grant funding purposes.
Gold Open Access Articles: May be shared according to the author-selected end-user license and should contain a CrossMark logo, the end user license, and a DOI link to the formal publication on ScienceDirect.
Please refer to Elsevier's posting policy for further information.

18. **For book authors** the following clauses are applicable in addition to the above: Authors are permitted to place a brief summary of their work online only. You are not allowed to download and post the published electronic version of your chapter, nor may you scan the printed edition to create an electronic version. **Posting to a repository:** Authors are permitted to post a summary of their chapter only in their institution's repository.
19. **Thesis/Dissertation**: If your license is for use in a thesis/dissertation your thesis may be submitted to your institution in either print or electronic form. Should your thesis be published commercially, please reapply for permission. These requirements include permission for the Library and Archives of Canada to supply single copies, on demand, of the complete thesis and include permission for Proquest/UMI to supply single copies, on demand, of the complete thesis. Should your thesis be published commercially, please reapply for permission. Theses and dissertations which contain embedded PJAs as part of the formal submission can be posted publicly by the awarding institution with DOI links back to the formal publications on ScienceDirect.

Elsevier Open Access Terms and Conditions

You can publish open access with Elsevier in hundreds of open access journals or in nearly 2000 established subscription journals that support open access publishing. Permitted third party re-use of these open access articles is defined by the author's choice of Creative Commons user license. See our open access license policy for more information.

Terms & Conditions applicable to all Open Access articles published with Elsevier:

Any reuse of the article must not represent the author as endorsing the adaptation of the article nor should the article be modified in such a way as to damage the author's honour or reputation. If any changes have been made, such changes must be clearly indicated.

The author(s) must be appropriately credited and we ask that you include the end user license and a DOI link to the formal publication on ScienceDirect.

If any part of the material to be used (for example, figures) has appeared in our publication with credit or acknowledgement to another source it is the responsibility of the user to ensure their reuse complies with the terms and conditions determined by the rights holder.

Additional Terms & Conditions applicable to each Creative Commons user license:

CC BY: The CC-BY license allows users to copy, to create extracts, abstracts and new works from the Article, to alter and revise the Article and to make commercial use of the Article (including reuse and/or resale of the Article by commercial entities), provided the user gives appropriate credit (with a link to the formal publication through the relevant DOI), provides a link to the license, indicates if changes were made and the licensor is not represented as endorsing the use made of the work. The full details of the license are available at http://creativecommons.org/licenses/by/4.0.

CC BY NC SA: The CC BY-NC-SA license allows users to copy, to create extracts, abstracts and new works from the Article, to alter and revise the Article, provided this is not done for commercial purposes, and that the user gives appropriate credit (with a link to the formal publication through the relevant DOI), provides a link to the license, indicates if changes were made and the licensor is not represented as endorsing the use made of the work. Further, any new works must be made available on the same conditions. The full details of the license are available at http://creativecommons.org/licenses/by-nc-sa/4.0.

CC BY NC ND: The CC BY-NC-ND license allows users to copy and distribute the Article, provided this is not done for commercial purposes and further does not permit distribution of the Article if it is changed or edited in any way, and provided the user gives appropriate credit (with a link to the formal publication through the relevant DOI), provides a link to the license, and that the licensor is not represented as endorsing the use made of the work. The full details of the license are available at http://creativecommons.org/licenses/by-nc-nd/4.0.

Any commercial reuse of Open Access articles published with a CC BY NC SA or CC BY NC ND license requires permission from Elsevier and will be subject to a fee.

Commercial reuse includes:

- Associating advertising with the full text of the Article
- Charging fees for document delivery or access
- Article aggregation
- Systematic distribution via e-mail lists or share buttons

Posting or linking by commercial companies for use by customers of those companies.

20. **Other Conditions**:

v1.9

Bibliography

[1] S. Priya and D. J. Inman, *Energy harvesting technologies*. Springer, 2009, vol. 21.

[2] J. Olivo, S. Carrara, and G. De Micheli, "Energy harvesting and remote powering for implantable biosensors," *IEEE Sensors Journal*, vol. 11, no. 7, pp. 1573–1586, 2010.

[3] L. Mateu and F. Moll, "Review of energy harvesting techniques and applications for microelectronics," in *VLSI Circuits and Systems II*, vol. 5837. International Society for Optics and Photonics, 2005, pp. 359–373.

[4] S. Beeby, M. Tudor, E. Koukharenko, N. White, T. O'Donnell, C. Saha, S. Kulkarni, and S. Roy, "Micromachined silicon generator for harvesting power from vibrations," 2004.

[5] D.-A. Wang and K.-H. Chang, "Electromagnetic energy harvesting from flow induced vibration," *Microelectronics Journal*, vol. 41, no. 6, pp. 356–364, 2010.

[6] D.-A. Wang, C.-Y. Chiu, and H.-T. Pham, "Electromagnetic energy harvesting from vibrations induced by kármán vortex street," *Mechatronics*, vol. 22, no. 6, pp. 746–756, 2012.

[7] A. Marin, S. Bressers, and S. Priya, "Multiple cell configuration electromagnetic vibration energy harvester," *Journal of Physics D: Applied Physics*, vol. 44, no. 29, p. 295501, 2011.

[8] P. D. Mitcheson, B. H. Stark, P. Miao, E. M. Yeatman, A. S. Holmes, and T. C. Green, "Analysis and optimisation of mems electrostatic on-chip power supply for self-powering of slow-moving sensors," 2003.

[9] R. Tashiro, N. Kabei, K. Katayama, Y. Ishizuka, F. Tsuboi, and K. Tsuchiya, "Development of an electrostatic generator that harnesses the motion of a living body: use of a resonant phenomenon," *JSME International Journal Series C Mechanical Systems, Machine Elements and Manufacturing*, vol. 43, no. 4, pp. 916–922, 2000.

[10] E. O. Torres and G. A. Rincón-Mora, "Electrostatic energy-harvesting and battery-charging cmos system prototype," *IEEE Transactions on Circuits and Systems I: Regular Papers*, vol. 56, no. 9, pp. 1938–1948, 2009.

[11] L. G. W. Tvedt, D. S. Nguyen, and E. Halvorsen, "Nonlinear behavior of an electrostatic energy harvester under wide-and narrowband excitation," *Journal of Microelectromechanical systems*, vol. 19, no. 2, pp. 305–316, 2010.

[12] C. P. Le and E. Halvorsen, "Mems electrostatic energy harvesters with end-stop effects," *Journal of Micromechanics and Microengineering*, vol. 22, no. 7, p. 074013, 2012.

[13] M. A. Hannan, S. Mutashar, S. A. Samad, and A. Hussain, "Energy harvesting for the implantable biomedical devices: issues and challenges," *Biomedical engineering online*, vol. 13, no. 1, p. 79, 2014.

[14] B. Saravanakumar, R. Mohan, K. Thiyagarajan, and S.-J. Kim, "Fabrication of a zno nanogenerator for eco-friendly biomechanical energy harvesting," *RSC Advances*, vol. 3, no. 37, pp. 16 646–16 656, 2013.

[15] G. Zhu, R. Yang, S. Wang, and Z. L. Wang, "Flexible high-output nanogenerator based on lateral zno nanowire array," *Nano letters*, vol. 10, no. 8, pp. 3151–3155, 2010.

[16] Z. L. Wang and J. Song, "Piezoelectric nanogenerators based on zinc oxide nanowire arrays," *Science*, vol. 312, no. 5771, pp. 242–246, 2006.

[17] S. Ozeri and D. Shmilovitz, "Ultrasonic transcutaneous energy transfer for powering implanted devices," *Ultrasonics*, vol. 50, no. 6, pp. 556–566, 2010.

[18] Y. Shigeta, Y. Hori, K. Fujimori, K. Tsuruta, and S. Nogi, "Development of highly efficient transducer for wireless power transmission system by ultrasonic," in *2011 IEEE MTT-S international microwave workshop series on innovative wireless power transmission: technologies, systems, and applications*. IEEE, 2011, pp. 171–174.

[19] S.-n. Suzuki, S. Kimura, T. Katane, H. Saotome, O. Saito, and K. Kobayashi, "Power and interactive information transmission to implanted medical device using ultrasonic," *Japanese journal of applied physics*, vol. 41, no. 5S, p. 3600, 2002.

[20] Y. Jeon, R. Sood, J.-H. Jeong, and S.-G. Kim, "Mems power generator with transverse mode thin film pzt," *Sensors and Actuators A: Physical*, vol. 122, no. 1, pp. 16–22, 2005.

[21] W. Choi, Y. Jeon, J.-H. Jeong, R. Sood, and S.-G. Kim, "Energy harvesting mems device based on thin film piezoelectric cantilevers," *Journal of Electroceramics*, vol. 17, no. 2-4, pp. 543–548, 2006.

[22] K.-I. Park, J. H. Son, G.-T. Hwang, C. K. Jeong, J. Ryu, M. Koo, I. Choi, S. H. Lee, M. Byun, Z. L. Wang *et al.*, "Highly-efficient, flexible piezoelectric pzt thin film nanogenerator on plastic substrates," *Advanced materials*, vol. 26, no. 16, pp. 2514–2520, 2014.

[23] S.-G. Kim, S. Priya, and I. Kanno, "Piezoelectric mems for energy harvesting," *MRS bulletin*, vol. 37, no. 11, pp. 1039–1050, 2012.

[24] A. Khan, Z. Abas, H. S. Kim, and I.-K. Oh, "Piezoelectric thin films: an integrated review of transducers and energy harvesting," *Smart Materials and Structures*, vol. 25, no. 5, p. 053002, 2016.

[25] F.-R. Fan, Z.-Q. Tian, and Z. L. Wang, "Flexible triboelectric generator," *Nano energy*, vol. 1, no. 2, pp. 328–334, 2012.

[26] Z. L. Wang, "Triboelectric nanogenerators as new energy technology for self-powered systems and as active mechanical and chemical sensors," *ACS nano*, vol. 7, no. 11, pp. 9533–9557, 2013.

[27] C. Wu, A. C. Wang, W. Ding, H. Guo, and Z. L. Wang, "Triboelectric nanogenerator: A foundation of the energy for the new era," *Advanced Energy Materials*, vol. 9, no. 1, p. 1802906, 2019.

[28] J. Henniker, "Triboelectricity in polymers," *Nature*, vol. 196, no. 4853, p. 474, 1962.

[29] D. Davies, "Charge generation on dielectric surfaces," *Journal of Physics D: Applied Physics*, vol. 2, no. 11, p. 1533, 1969.

[30] M. S. Rogalski and S. B. Palmer, *Advanced university physics*. CRC Press, 2018.

[31] J. D. Jackson, "Classical electrodynamics," 1999.

[32] Z. L. Wang, "On maxwell's displacement current for energy and sensors: the origin of nanogenerators," *Materials Today*, vol. 20, no. 2, pp. 74–82, 2017.

[33] C. K. Jeong, K. M. Baek, S. Niu, T. W. Nam, Y. H. Hur, D. Y. Park, G.-T. Hwang, M. Byun, Z. L. Wang, Y. S. Jung *et al.*, "Topographically-designed triboelectric nanogenerator via block copolymer self-assembly," *Nano letters*, vol. 14, no. 12, pp. 7031–7038, 2014.

[34] H. S. Wang, C. K. Jeong, M.-H. Seo, D. J. Joe, J. H. Han, J.-B. Yoon, and K. J. Lee, "Performance-enhanced triboelectric nanogenerator enabled by wafer-scale nanograte s of multistep pattern downscaling," *Nano Energy*, vol. 35, pp. 415–423, 2017.

[35] S. Wang, L. Lin, and Z. L. Wang, "Nanoscale triboelectric-effect-enabled energy conversion for sustainably powering portable electronics," *Nano letters*, vol. 12, no. 12, pp. 6339–6346, 2012.

[36] J. Chun, J. W. Kim, W.-s. Jung, C.-Y. Kang, S.-W. Kim, Z. L. Wang, and J. M. Baik, "Mesoporous pores impregnated with au nanoparticles as effective dielectrics for enhancing triboelectric nanogenerator performance in harsh environments," *Energy & Environmental Science*, vol. 8, no. 10, pp. 3006–3012, 2015.

[37] W. Li, Y. Zhang, L. Liu, D. Li, L. Liao, and C. Pan, "A high energy output nanogenerator based on reduced graphene oxide," *Nanoscale*, vol. 7, no. 43, pp. 18 147–18 151, 2015.

[38] Z.-H. Lin, Y. Xie, Y. Yang, S. Wang, G. Zhu, and Z. L. Wang, "Enhanced triboelectric nanogenerators and triboelectric nanosensor using chemically modified tio2 nanomaterials," *ACS nano*, vol. 7, no. 5, pp. 4554–4560, 2013.

[39] S. Niu, Y. Liu, S. Wang, L. Lin, Y. S. Zhou, Y. Hu, and Z. L. Wang, "Theory of sliding-mode triboelectric nanogenerators," *Advanced materials*, vol. 25, no. 43, pp. 6184–6193, 2013.

[40] S. Niu, Y. Liu, S. Wang, L. Lin, Y. S. Zhou, Y. Hu, and Z. L. Wang, "Theoretical investigation and structural optimization of single-electrode triboelectric nanogenerators," *Advanced Functional Materials*, vol. 24, no. 22, pp. 3332–3340, 2014.

[41] S. Niu, Y. S. Zhou, S. Wang, Y. Liu, L. Lin, Y. Bando, and Z. L. Wang, "Simulation method for optimizing the performance of an integrated triboelectric nanogenerator energy harvesting system," *Nano Energy*, vol. 8, pp. 150–156, 2014.

[42] S. Niu and Z. L. Wang, "Theoretical systems of triboelectric nanogenerators," *Nano Energy*, vol. 14, pp. 161–192, 2015.

[43] S. Niu, S. Wang, L. Lin, Y. Liu, Y. S. Zhou, Y. Hu, and Z. L. Wang, "Theoretical study of contact-mode triboelectric nanogenerators as an effective power source," *Energy & Environmental Science*, vol. 6, no. 12, pp. 3576–3583, 2013.

[44] Q. Shen, X. Xie, M. Peng, N. Sun, H. Shao, H. Zheng, Z. Wen, and X. Sun, "Self-powered vehicle emission testing system based on coupling of triboelectric and chemoresistive effects," *Advanced Functional Materials*, vol. 28, no. 10, p. 1703420, 2018.

[45] X. Xie, Z. Wen, Q. Shen, C. Chen, M. Peng, Y. Yang, N. Sun, P. Cheng, H. Shao, Y. Zhang *et al.*, "Impedance matching effect between a triboelectric nanogenerator and a piezoresistive pressure sensor induced self-powered weighing," *Advanced Materials Technologies*, vol. 3, no. 6, p. 1800054, 2018.

[46] P. Bai, G. Zhu, Z.-H. Lin, Q. Jing, J. Chen, G. Zhang, J. Ma, and Z. L. Wang, "Integrated multilayered triboelectric nanogenerator for harvesting biomechanical energy from human motions," *ACS nano*, vol. 7, no. 4, pp. 3713–3719, 2013.

[47] S. Niu, Y. Liu, X. Chen, S. Wang, Y. S. Zhou, L. Lin, Y. Xie, and Z. L. Wang, "Theory of freestanding triboelectric-layer-based nanogenerators," *Nano Energy*, vol. 12, pp. 760–774, 2015.

[48] Y. Jie, N. Wang, X. Cao, Y. Xu, T. Li, X. Zhang, and Z. L. Wang, "Self-powered triboelectric nanosensor with poly (tetrafluoroethylene) nanoparticle arrays for dopamine detection," *ACS nano*, vol. 9, no. 8, pp. 8376–8383, 2015.

[49] S. Cui, Y. Zheng, T. Zhang, D. Wang, F. Zhou, and W. Liu, "Self-powered ammonia nanosensor based on the integration of the gas sensor and triboelectric nanogenerator," *Nano energy*, vol. 49, pp. 31–39, 2018.

[50] H. Wang, H. Wu, D. Hasan, T. He, Q. Shi, and C. Lee, "Self-powered dual-mode amenity sensor based on the water–air triboelectric nanogenerator," *ACS nano*, vol. 11, no. 10, pp. 10 337–10 346, 2017.

[51] H. Guo, T. Li, X. Cao, J. Xiong, Y. Jie, M. Willander, X. Cao, N. Wang, and Z. L. Wang, "Self-sterilized flexible single-electrode triboelectric nanogenerator for energy harvesting and dynamic force sensing," *ACS nano*, vol. 11, no. 1, pp. 856–864, 2017.

[52] Y. Liu, N. Sun, J. Liu, Z. Wen, X. Sun, S.-T. Lee, and B. Sun, "Integrating a silicon solar cell with a triboelectric nanogenerator via a mutual electrode for harvesting energy from sunlight and raindrops," *ACS nano*, vol. 12, no. 3, pp. 2893–2899, 2018.

[53] P. Cheng, H. Guo, Z. Wen, C. Zhang, X. Yin, X. Li, D. Liu, W. Song, X. Sun, J. Wang *et al.*, "Largely enhanced triboelectric nanogenerator for efficient harvesting of water wave energy by soft contacted structure," *Nano Energy*, vol. 57, pp. 432–439, 2019.

[54] Q. Zheng, H. Zhang, B. Shi, X. Xue, Z. Liu, Y. Jin, Y. Ma, Y. Zou, X. Wang, Z. An *et al.*, "In vivo self-powered wireless cardiac monitoring via implantable triboelectric nanogenerator," *Acs Nano*, vol. 10, no. 7, pp. 6510–6518, 2016.

[55] Y. Yang, N. Sun, Z. Wen, P. Cheng, H. Zheng, H. Shao, Y. Xia, C. Chen, H. Lan, X. Xie *et al.*, "Liquid-metal-based super-stretchable and structure-designable triboelectric nanogenerator for wearable electronics," *ACS nano*, vol. 12, no. 2, pp. 2027–2034, 2018.

[56] Z. Zhao, X. Pu, C. Du, L. Li, C. Jiang, W. Hu, and Z. L. Wang, "Freestanding flag-type triboelectric nanogenerator for harvesting high-altitude wind energy from arbitrary directions," *ACS nano*, vol. 10, no. 2, pp. 1780–1787, 2016.

[57] L. Zhang, B. Zhang, J. Chen, L. Jin, W. Deng, J. Tang, H. Zhang, H. Pan, M. Zhu, W. Yang *et al.*, "Lawn structured triboelectric nanogenerators for scavenging sweeping wind energy on rooftops," *Advanced Materials*, vol. 28, no. 8, pp. 1650–1656, 2016.

[58] P. Cheng, Y. Liu, Z. Wen, H. Shao, A. Wei, X. Xie, C. Chen, Y. Yang, M. Peng, Q. Zhuo *et al.*, "Atmospheric pressure difference driven triboelectric nanogenerator for efficiently harvesting ocean wave energy," *Nano Energy*, vol. 54, pp. 156–162, 2018.

[59] Q. Liang, X. Yan, Y. Gu, K. Zhang, M. Liang, S. Lu, X. Zheng, and Y. Zhang, "Highly transparent triboelectric nanogenerator for harvesting water-related energy reinforced by antireflection coating," *Scientific reports*, vol. 5, p. 9080, 2015.

[60] N. Sun, Z. Wen, F. Zhao, Y. Yang, H. Shao, C. Zhou, Q. Shen, K. Feng, M. Peng, Y. Li *et al.*, "All flexible electrospun papers based self-charging power system," *Nano Energy*, vol. 38, pp. 210–217, 2017.

[61] Q. Zheng, B. Shi, F. Fan, X. Wang, L. Yan, W. Yuan, S. Wang, H. Liu, Z. Li, and Z. L. Wang, "In vivo powering of pacemaker by breathing-driven implanted triboelectric nanogenerator," *Advanced materials*, vol. 26, no. 33, pp. 5851–5856, 2014.

[62] Q. Zheng, Y. Zou, Y. Zhang, Z. Liu, B. Shi, X. Wang, Y. Jin, H. Ouyang, Z. Li, and Z. L. Wang, "Biodegradable triboelectric nanogenerator as a life-time designed implantable power source," *Science advances*, vol. 2, no. 3, p. e1501478, 2016.

[63] J. Chen, G. Zhu, J. Yang, Q. Jing, P. Bai, W. Yang, X. Qi, Y. Su, and Z. L. Wang, "Personalized keystroke dynamics for self-powered human–machine interfacing," *ACS nano*, vol. 9, no. 1, pp. 105–116, 2015.

[64] X. Fan, J. Chen, J. Yang, P. Bai, Z. Li, and Z. L. Wang, "Ultrathin, rollable, paper-based triboelectric nanogenerator for acoustic energy harvesting and self-powered sound recording," *ACS nano*, vol. 9, no. 4, pp. 4236–4243, 2015.

[65] J. Yang, J. Chen, Y. Liu, W. Yang, Y. Su, and Z. L. Wang, "Triboelectrification-based organic film nanogenerator for acoustic energy harvesting and self-powered active acoustic sensing," *ACS nano*, vol. 8, no. 3, pp. 2649–2657, 2014.

[66] H. Guo, X. Pu, J. Chen, Y. Meng, M.-H. Yeh, G. Liu, Q. Tang, B. Chen, D. Liu, S. Qi *et al.*, "A highly sensitive, self-powered triboelectric auditory sensor for social robotics and hearing aids," *Science Robotics*, vol. 3, no. 20, p. eaat2516, 2018.

[67] S. Li, W. Peng, J. Wang, L. Lin, Y. Zi, G. Zhang, and Z. L. Wang, "All-elastomer-based triboelectric nanogenerator as a keyboard cover to harvest typing energy," *ACS nano*, vol. 10, no. 8, pp. 7973–7981, 2016.

[68] C. Wu, W. Ding, R. Liu, J. Wang, A. C. Wang, J. Wang, S. Li, Y. Zi, and Z. L. Wang, "Keystroke dynamics enabled authentication and identification using triboelectric nanogenerator array," *Materials Today*, vol. 21, no. 3, pp. 216–222, 2018.

[69] Y. Jie, H. Zhu, X. Cao, Y. Zhang, N. Wang, L. Zhang, and Z. L. Wang, "One-piece triboelectric nanosensor for self-triggered alarm system and latent fingerprint detection," *ACS nano*, vol. 10, no. 11, pp. 10 366–10 372, 2016.

[70] X. Pu, H. Guo, J. Chen, X. Wang, Y. Xi, C. Hu, and Z. L. Wang, "Eye motion triggered self-powered mechnosensational communication system using triboelectric nanogenerator," *Science advances*, vol. 3, no. 7, p. e1700694, 2017.

[71] T. Ehmann, C. Mantler, D. Jensen, and R. Neufang, "Monitoring the quality of ultra-pure water in the semiconductor industry by online ion chromatography," *Microchimica Acta*, vol. 154, no. 1-2, pp. 15–20, 2006.

[72] W. H. Organization, *Guidelines for drinking-water quality*. World Health Organization, 2004, vol. 1.

[73] N. Savage and M. S. Diallo, "Nanomaterials and water purification: opportunities and challenges," *Journal of Nanoparticle research*, vol. 7, no. 4-5, pp. 331–342, 2005.

[74] R. A. Khaydarov, R. R. Khaydarov, and O. Gapurova, "Water purification from metal ions using carbon nanoparticle-conjugated polymer nanocomposites," *Water research*, vol. 44, no. 6, pp. 1927–1933, 2010.

[75] T. Sreeprasad, S. M. Maliyekkal, K. Lisha, and T. Pradeep, "Reduced graphene oxide–metal/metal oxide composites: facile synthesis and application in water purification," *Journal of hazardous materials*, vol. 186, no. 1, pp. 921–931, 2011.

[76] S. Bolisetty and R. Mezzenga, "Amyloid–carbon hybrid membranes for universal water purification," *Nature nanotechnology*, vol. 11, no. 4, p. 365, 2016.

[77] M. Shenashen, S. El-Safty, and E. Elshehy, "Architecture of optical sensor for recognition of multiple toxic metal ions from water," *Journal of hazardous materials*, vol. 260, pp. 833–843, 2013.

[78] A. I. Zia, A. M. Syaifudin, S. Mukhopadhyay, P. Yu, I. Al-Bahadly, C. P. Gooneratne, J. Kosel, and T.-S. Liao, "Electrochemical impedance spectroscopy based mems sensors for phthalates detection in water and juices," in *Journal of Physics: Conference Series*, vol. 439, no. 1. IOP Publishing, 2013, p. 012026.

[79] G. Sener, L. Uzun, and A. Denizli, "Colorimetric sensor array based on gold nanoparticles and amino acids for identification of toxic metal ions in water," *ACS applied materials & interfaces*, vol. 6, no. 21, pp. 18 395–18 400, 2014.

[80] I.-B. Kim and U. H. Bunz, "Modulating the sensory response of a conjugated polymer by proteins: an agglutination assay for mercury ions in water," *Journal of the American Chemical Society*, vol. 128, no. 9, pp. 2818–2819, 2006.

[81] L. Sartore, M. Barbaglio, L. Borgese, and E. Bontempi, "Polymer-grafted qcm chemical sensor and application to heavy metal ions real time detection," *Sensors and Actuators B: Chemical*, vol. 155, no. 2, pp. 538–544, 2011.

[82] F. Tan, L. Cong, N. M. Saucedo, J. Gao, X. Li, and A. Mulchandani, "An electrochemically reduced graphene oxide chemiresistive sensor for sensitive detection of hg2+ ion in water samples," *Journal of hazardous materials*, vol. 320, pp. 226–233, 2016.

[83] C. Chouteau, S. Dzyadevych, C. Durrieu, and J.-M. Chovelon, "A bi-enzymatic whole cell conductometric biosensor for heavy metal ions and pesticides detection in water samples," *Biosensors and Bioelectronics*, vol. 21, no. 2, pp. 273–281, 2005.

[84] H. Guedri and C. Durrieu, "A self-assembled monolayers based conductometric algal whole cell biosensor for water monitoring," *Microchimica Acta*, vol. 163, no. 3-4, pp. 179–184, 2008.

[85] F. Long, A. Zhu, H. Shi, H. Wang, and J. Liu, "Rapid on-site/in-situ detection of heavy metal ions in environmental water using a structure-switching dna optical biosensor," *Scientific reports*, vol. 3, p. 2308, 2013.

[86] Z. L. Wang, J. Chen, and L. Lin, "Progress in triboelectric nanogenerators as a new energy technology and self-powered sensors," *Energy & Environmental Science*, vol. 8, no. 8, pp. 2250–2282, 2015.

[87] Z. Wen, M.-H. Yeh, H. Guo, J. Wang, Y. Zi, W. Xu, J. Deng, L. Zhu, X. Wang, C. Hu *et al.*, "Self-powered textile for wearable electronics by hybridizing fiber-shaped nanogenerators, solar cells, and supercapacitors," *Science advances*, vol. 2, no. 10, p. e1600097, 2016.

[88] Y. Liu, N. Sun, J. Liu, Z. Wen, X. Sun, S.-T. Lee, and B. Sun, "Integrating a silicon solar cell with a triboelectric nanogenerator via a mutual electrode for harvesting energy from sunlight and raindrops," *ACS nano*, vol. 12, no. 3, pp. 2893–2899, 2018.

[89] Z. L. Wang, "Nanogenerators, self-powered systems, blue energy, piezotronics and piezo-phototronics–a recall on the original thoughts for coining these fields," *Nano Energy*, vol. 54, pp. 477–483, 2018.

[90] A. Wei, X. Xie, Z. Wen, H. Zheng, H. Lan, H. Shao, X. Sun, J. Zhong, and S.-T. Lee, "Triboelectric nanogenerator driven self-powered photoelectrochemical water splitting based on hematite photoanodes," *ACS nano*, vol. 12, no. 8, pp. 8625–8632, 2018.

[91] X. Cao, Y. Jie, N. Wang, and Z. L. Wang, "Triboelectric nanogenerators driven self-powered electrochemical processes for energy and environmental science," *Advanced Energy Materials*, vol. 6, no. 23, p. 1600665, 2016.

[92] Z. Wen, Q. Shen, and X. Sun, "Nanogenerators for self-powered gas sensing," *Nano-micro letters*, vol. 9, no. 4, p. 45, 2017.

[93] Z. Wen, J. Fu, L. Han, Y. Liu, M. Peng, L. Zheng, Y. Zhu, X. Sun, and Y. Zi, "Toward self-powered photodetection enabled by triboelectric nanogenerators," *Journal of Materials Chemistry C*, vol. 6, no. 44, pp. 11 893–11 902, 2018.

[94] Z. Wen, J. Chen, M.-H. Yeh, H. Guo, Z. Li, X. Fan, T. Zhang, L. Zhu, and Z. L. Wang, "Blow-driven triboelectric nanogenerator as an active alcohol breath analyzer," *Nano Energy*, vol. 16, pp. 38–46, 2015.

[95] G. Zhu, J. Chen, T. Zhang, Q. Jing, and Z. L. Wang, "Radial-arrayed rotary electrification for high performance triboelectric generator," *Nature communications*, vol. 5, p. 3426, 2014.

[96] S. Niu, S. Wang, Y. Liu, Y. S. Zhou, L. Lin, Y. Hu, K. C. Pradel, and Z. L. Wang, "A theoretical study of grating structured triboelectric nanogenerators," *Energy & Environmental Science*, vol. 7, no. 7, pp. 2339–2349, 2014.

[97] S. Chen, N. Wang, L. Ma, T. Li, M. Willander, Y. Jie, X. Cao, and Z. L. Wang, "Triboelectric nanogenerator for sustainable wastewater treatment via a self-powered electrochemical process," *Advanced Energy Materials*, vol. 6, no. 8, p. 1501778, 2016.

[98] C. Han, C. Zhang, W. Tang, X. Li, and Z. L. Wang, "High power triboelectric nanogenerator based on printed circuit board (pcb) technology," *Nano Research*, vol. 8, no. 3, pp. 722–730, 2015.

[99] G. Barbero, F. Batalioto, and A. Figueiredo Neto, "Theory of small-signal ac response of a dielectric liquid containing two groups of ions," *Applied Physics Letters*, vol. 92, no. 17, p. 172908, 2008.

[100] I. Lelidis and G. Barbero, "Effect of different anionic and cationic mobilities on the impedance spectroscopy measurements," *Physics Letters A*, vol. 343, no. 6, pp. 440–445, 2005.

[101] J. Picalek and J. Kolafa, "Molecular dynamics study of conductivity of ionic liquids: The kohlrausch law," *Journal of Molecular Liquids*, vol. 134, no. 1-3, pp. 29–33, 2007.

[102] J. J. Davis, *Engineering the bioelectronic interface: applications to analyte biosensing and protein detection*. Royal Society of Chemistry, 2009.

[103] J. N. Miller and J. C. Miller, *Statistics and chemometrics for analytical chemistry, sixth edition*. Pearson Education, 2010.

[104] Z. Li, J. Chen, J. Yang, Y. Su, X. Fan, Y. Wu, C. Yu, and Z. L. Wang, "β-cyclodextrin enhanced triboelectrification for self-powered phenol detection and electrochemical degradation," *Energy & Environmental Science*, vol. 8, no. 3, pp. 887–896, 2015.

[105] Z.-H. Lin, G. Zhu, Y. S. Zhou, Y. Yang, P. Bai, J. Chen, and Z. L. Wang, "A self-powered triboelectric nanosensor for mercury ion detection," *Angewandte Chemie International Edition*, vol. 52, no. 19, pp. 5065–5069, 2013.

[106] Z. Li, J. Chen, H. Guo, X. Fan, Z. Wen, M.-H. Yeh, C. Yu, X. Cao, and Z. L. Wang, "Triboelectrification-enabled self-powered detection and removal of heavy metal ions in wastewater," *Advanced Materials*, vol. 28, no. 15, pp. 2983–2991, 2016.

[107] H. Zhang, Y. Yang, Y. Su, J. Chen, C. Hu, Z. Wu, Y. Liu, C. P. Wong, Y. Bando, and Z. L. Wang, "Triboelectric nanogenerator as self-powered active sensors for detecting liquid/gaseous water/ethanol," *Nano Energy*, vol. 2, no. 5, pp. 693–701, 2013.

[108] Z.-H. Lin, G. Cheng, W. Wu, K. C. Pradel, and Z. L. Wang, "Dual-mode triboelectric nanogenerator for harvesting water energy and as a self-powered ethanol nanosensor," *ACS nano*, vol. 8, no. 6, pp. 6440–6448, 2014.

[109] S.-n. Suzuki, S. Kimura, T. Katane, H. Saotome, O. Saito, and K. Kobayashi, "Power and interactive information transmission to implanted medical device using ultrasonic," *Japanese journal of applied physics*, vol. 41, no. 5S, p. 3600, 2002.

[110] J. Leadbetter, J. A. Brown, and R. B. Adamson, "The design of ultrasonic lead magnesium niobate-lead titanate (pmn-pt) composite transducers for power and signal delivery to implanted hearing aids," in *Proceedings of Meetings on Acoustics ICA2013*, vol. 19, no. 1. ASA, 2013, p. 030029.

[111] X.-S. Zhang, M.-D. Han, R.-X. Wang, B. Meng, F.-Y. Zhu, X.-M. Sun, W. Hu, W. Wang, Z.-H. Li, and H.-X. Zhang, "High-performance triboelectric nanogenerator with enhanced energy density based on single-step fluorocarbon plasma treatment," *Nano Energy*, vol. 4, pp. 123–131, 2014.

[112] P. Narayana, J. Ophir, and N. Maklad, "The attenuation of ultrasound in biological fluids," *The Journal of the Acoustical Society of America*, vol. 76, no. 1, pp. 1–4, 1984.

[113] L. Crum, M. Bailey, P. Kaczkowski, I. Makin, P. Mourad, K. Beach, S. Cartery, U. Schmiedlq, W. Chandler, R. Martin *et al.*, "Therapeutic ultrasound: A promising future in clinical medicine," in *Proc. 16 Internat Congress on Acoust. & 135 Meet. of ASA*, 1998, pp. 719–720.

[114] S. Mo, C.-C. Coussios, L. Seymour, and R. Carlisle, "Ultrasound-enhanced drug delivery for cancer," *Expert opinion on drug delivery*, vol. 9, no. 12, pp. 1525–1538, 2012.

[115] Food, D. Administration *et al.*, "Guidance for industry and fda staff information for manufacturers seeking marketing clearance of diagnostic ultrasound systems and transducers," *Silver Spring, MD: Author*, 2008.

[116] T. L. Szabo, *Diagnostic ultrasound imaging: inside out*. Academic Press, 2004.

[117] F. Mazzilli, C. Lafon, and C. Dehollain, "A 10.5 cm ultrasound link for deep implanted medical devices," *IEEE transactions on biomedical circuits and systems*, vol. 8, no. 5, pp. 738–750, 2014.

[118] J.-Y. Tsai, K.-H. Huang, J.-R. Wang, S.-I. Liu, and P.-C. Li, "Ultrasonic wireless power and data communication for neural stimulation," in *2011 IEEE International Ultrasonics Symposium*. IEEE, 2011, pp. 1052–1055.

[119] M. Meng and M. Kiani, "Design and optimization of ultrasonic wireless power transmission links for millimeter-sized biomedical implants," *IEEE transactions on biomedical circuits and systems*, vol. 11, no. 1, pp. 98–107, 2017.

[120] E. Mehdizadeh and G. Piazza, "Aln on soi pmuts for ultrasonic power transfer," in *2017 IEEE International Ultrasonics Symposium (IUS)*. IEEE, 2017, pp. 1–4.

[121] W. H. Peake and E. G. Thurston, "The lowest resonant frequency of a water-loaded circular plate," *The Journal of the Acoustical Society of America*, vol. 26, no. 2, pp. 166–168, 1954.

[122] C. Xu, Y. Zi, A. C. Wang, H. Zou, Y. Dai, X. He, P. Wang, Y.-C. Wang, P. Feng, D. Li *et al.*, "On the electron-transfer mechanism in the contact-electrification effect," *Advanced Materials*, vol. 30, no. 15, p. 1706790, 2018.

[123] W. Ko, J. Suminto, G. Yeh *et al.*, "Bonding techniques for microsensors," *Micromachining and micropackaging of Transducers*, vol. 20, pp. 41–61, 1985.

[124] A. Hanneborg, "Silicon wafer bonding techniques for assembly of micromechanical elements," in *[1991] Proceedings. IEEE Micro Electro Mechanical Systems*. IEEE, 1991, pp. 92–98.

[125] M. Shimbo, K. Furukawa, K. Fukuda, and K. Tanzawa, "Silicon-to-silicon direct bonding method," *Journal of Applied Physics*, vol. 60, no. 8, pp. 2987–2989, 1986.

[126] K. Knowles and A. Van Helvoort, "Anodic bonding," *International materials reviews*, vol. 51, no. 5, pp. 273–311, 2006.

[127] J. Wei, H. Xie, M. Nai, C. Wong, and L. Lee, "Low temperature wafer anodic bonding," *Journal of Micromechanics and Microengineering*, vol. 13, no. 2, p. 217, 2003.

[128] H. Henmi, S. Shoji, Y. Shoji, K. Yoshimi, and M. Esashi, "Vacuum packaging for microsensors by glass-silicon anodic bonding," *Sensors and Actuators A: Physical*, vol. 43, no. 1-3, pp. 243–248, 1994.

[129] J.-M. Kim, D. H. Oh, J. Yoon, S. Cho, N. Kim, J. Cho, Y. Kwon, C. Cheon, and Y.-K. Kim, "Silicon mems probe using a simple adhesive bonding process for permittivity measurement," *Journal of Micromechanics and Microengineering*, vol. 15, no. 11, p. N11, 2005.

[130] Z. Li, L. L. Wong, A. I. Chen, S. Na, J. Sun, and J. T. Yeow, "Fabrication of capacitive micromachined ultrasonic transducers based on adhesive wafer bonding technique," *Journal of Micromechanics and Microengineering*, vol. 26, no. 11, p. 115019, 2016.

[131] W. Teh, G. Lihui, R. Kumar, and D.-L. Kwong, "200-mm wafer-scale transfer of 0.18-μm dual-damascene cu/sio 2 interconnection system to plastic substrates," *IEEE electron device letters*, vol. 26, no. 11, pp. 802–804, 2005.

[132] M. Agirregabiria, F. Blanco, J. Berganzo, M. Arroyo, A. Fullaondo, K. Mayora, and J. Ruano-Lopez, "Fabrication of su-8 multilayer microstructures based on successive cmos compatible adhesive bonding and releasing steps," *Lab on a Chip*, vol. 5, no. 5, pp. 545–552, 2005.

[133] M. Despont, U. Drechsler, R. Yu, H. Pogge, and P. Vettiger, "Wafer-scale microdevice transfer/interconnect: Its application in an afm-based data-storage system," *Journal of Microelectromechanical Systems*, vol. 13, no. 6, pp. 895–901, 2004.

[134] F. Niklaus, P. Enoksson, E. Kälvesten, and G. Stemme, "Low-temperature full wafer adhesive bonding," *Journal of Micromechanics and Microengineering*, vol. 11, no. 2, p. 100, 2001.

[135] N. Miki, X. Zhang, R. Khanna, A. Ayon, D. Ward, and S. Spearing, "Multi-stack silicon-direct wafer bonding for 3d mems manufacturing," *Sensors and Actuators A: Physical*, vol. 103, no. 1-2, pp. 194–201, 2003.

[136] A. S. Logan, L. L. Wong, and J. T. Yeow, "2-d cmut wafer bonded imaging arrays with a row-column addressing scheme," in *2009 IEEE International Ultrasonics Symposium*. IEEE, 2009, pp. 984–987.

[137] A. S. Logan and J. T. Yeow, "1-d cmut arrays fabricated using a novel wafer bonding process," in *2008 IEEE Ultrasonics Symposium*. IEEE, 2008, pp. 1226–1229.

[138] J. Lasky, S. Stiffler, F. White, and J. Abernathey, "Silicon-on-insulator (soi) by bonding and etch-back," in *1985 International Electron Devices Meeting*. IEEE, 1985, pp. 684–687.

[139] J. Lasky, "Wafer bonding for silicon-on-insulator technologies," *Applied Physics Letters*, vol. 48, no. 1, pp. 78–80, 1986.

[140] J. Haisma, G. Spierings, U. Biermann, and J. Pals, "Silicon-on-insulator wafer bonding-wafer thinning technological evaluations," *Japanese Journal of Applied Physics*, vol. 28, no. 8R, p. 1426, 1989.

[141] L. S. McCarty and G. M. Whitesides, "Electrostatic charging due to separation of ions at interfaces: contact electrification of ionic electrets," *Angewandte Chemie International Edition*, vol. 47, no. 12, pp. 2188–2207, 2008.

[142] S. Lin, L. Xu, C. Xu, X. Chen, A. Wang, B. Zhang, P. Lin, Y. Yang, H. Zhao, and Z. Wang, "Electron transfer in nanoscale contact electrification: Effect of temperature in the metal-dielectric case." *Advanced materials (Deerfield Beach, Fla.)*, pp. e1 808 197–e1 808 197, 2019.

[143] W. Melitz, J. Shen, A. C. Kummel, and S. Lee, "Kelvin probe force microscopy and its application," *Surface science reports*, vol. 66, no. 1, pp. 1–27, 2011.

[144] Y. S. Zhou, S. Wang, Y. Yang, G. Zhu, S. Niu, Z.-H. Lin, Y. Liu, and Z. L. Wang, "Manipulating nanoscale contact electrification by an applied electric field," *Nano letters*, vol. 14, no. 3, pp. 1567–1572, 2014.

[145] S. Wang, Y. Zi, Y. S. Zhou, S. Li, F. Fan, L. Lin, and Z. L. Wang, "Molecular surface functionalization to enhance the power output of triboelectric nanogenerators," *Journal of Materials Chemistry A*, vol. 4, no. 10, pp. 3728–3734, 2016.

[146] H.-J. Kim, E.-C. Yim, J.-H. Kim, S.-J. Kim, J.-Y. Park, and I.-K. Oh, "Bacterial nanocellulose triboelectric nanogenerator," *Nano Energy*, vol. 33, pp. 130–137, 2017.

[147] S. Ozeri, D. Shmilovitz, S. Singer, and C.-C. Wang, "Ultrasonic transcutaneous energy transfer using a continuous wave 650 khz gaussian shaded transmitter," *Ultrasonics*, vol. 50, no. 7, pp. 666–674, 2010.

[148] H. Vihvelin, J. R. Leadbetter, M. Bance, J. A. Brown, and R. B. Adamson, "Compensating for tissue changes in an ultrasonic power link for implanted medical devices," *IEEE transactions on biomedical circuits and systems*, vol. 10, no. 2, pp. 404–411, 2016.

[149] Q. Shi, T. Wang, and C. Lee, "Mems based broadband piezoelectric ultrasonic energy harvester (pueh) for enabling self-powered implantable biomedical devices," *Scientific reports*, vol. 6, p. 24946, 2016.

[150] A. S. Logan, L. L. Wong, A. I. Chen, and J. T. Yeow, "A 32 x 32 element row-column addressed capacitive micromachined ultrasonic transducer," *IEEE transactions on ultrasonics, ferroelectrics, and frequency control*, vol. 58, no. 6, pp. 1266–1271, 2011.

[151] Z. Zheng, S. Na, I. Albert, H. Chen, Z. Li, L. L. Wong, Z. Sun, Y. Yao, P. Liu, and J. T. Yeow, "Development of a novel cmut-based concentric dual-element ultrasonic transducer: Design, fabrication, and characterization," *Journal of Microelectromechanical Systems*, vol. 27, no. 3, pp. 538–546, 2018.

[152] F. Naghmouchi, M. Ghorbel, A. Hamida, and M. Samet, "Cmos ask system modulation dedicated to cochlear prosthesis," in *First International Symposium on Control, Communications and Signal Processing, 2004.* IEEE, 2004, pp. 267–270.

[153] A. G. Fowler, S. Moheimani, and S. Behrens, "An omnidirectional mems ultrasonic energy harvester for implanted devices," *Journal of Microelectromechanical Systems*, vol. 23, no. 6, pp. 1454–1462, 2014.

[154] S. B. Horowitz, M. Sheplak, L. N. Cattafesta III, and T. Nishida, "A mems acoustic energy harvester," *Journal of Micromechanics and Microengineering*, vol. 16, no. 9, p. S174, 2006.

[155] H. Kawanabe, T. Katane, H. Saotome, O. Saito, and K. Kobayashi, "Power and information transmission to implanted medical device using ultrasonic," *Japanese journal of applied physics*, vol. 40, no. 5S, p. 3865, 2001.

[156] K. Bazaka and M. Jacob, "Implantable devices: issues and challenges," *Electronics*, vol. 2, no. 1, pp. 1–34, 2013.

[157] M. A. Hannan, S. M. Abbas, S. A. Samad, and A. Hussain, "Modulation techniques for biomedical implanted devices and their challenges," *Sensors*, vol. 12, no. 1, pp. 297–319, 2012.

[158] Y. Xi, J. Wang, Y. Zi, X. Li, C. Han, X. Cao, C. Hu, and Z. Wang, "High efficient harvesting of underwater ultrasonic wave energy by triboelectric nanogenerator," *Nano Energy*, vol. 38, pp. 101–108, 2017.

[159] Y. Zi, S. Niu, J. Wang, Z. Wen, W. Tang, and Z. L. Wang, "Standards and figure-of-merits for quantifying the performance of triboelectric nanogenerators," *Nature communications*, vol. 6, p. 8376, 2015.

[160] J. Shao, M. Willatzen, T. Jiang, W. Tang, X. Chen, J. Wang, and Z. L. Wang, "Quantifying the power output and structural figure-of-merits of triboelectric nanogenerators in a charging system starting from the maxwell's displacement current," *Nano Energy*, 2019.

[161] P. Bai, G. Zhu, Q. Jing, J. Yang, J. Chen, Y. Su, J. Ma, G. Zhang, and Z. L. Wang, "Membrane-based self-powered triboelectric sensors for pressure change detection and its uses in security surveillance and healthcare monitoring," *Advanced Functional Materials*, vol. 24, no. 37, pp. 5807–5813, 2014.

[162] J. Yang, J. Chen, Y. Su, Q. Jing, Z. Li, F. Yi, X. Wen, Z. Wang, and Z. L. Wang, "Eardrum-inspired active sensors for self-powered cardiovascular system characterization and throat-attached anti-interference voice recognition," *Advanced Materials*, vol. 27, no. 8, pp. 1316–1326, 2015.

[163] A. Yu, M. Song, Y. Zhang, Y. Zhang, L. Chen, J. Zhai, and Z. L. Wang, "Self-powered acoustic source locator in underwater environment based on organic film triboelectric nanogenerator," *Nano Research*, vol. 8, no. 3, pp. 765–773, 2015.

[164] Z. Li, S. Na, A. I. Chen, L. L. Wong, Z. Sun, P. Liu, and J. T. Yeow, "Optimization on benzocyclobutene-based cmut fabrication with an inverse structure," *Sensors and Actuators A: Physical*, vol. 281, pp. 1–8, 2018.

[165] Z.-H. Lin, G. Cheng, L. Lin, S. Lee, and Z. L. Wang, "Water–solid surface contact electrification and its use for harvesting liquid-wave energy," *Angewandte Chemie International Edition*, vol. 52, no. 48, pp. 12 545–12 549, 2013.

[166] Z.-H. Lin, G. Cheng, S. Lee, K. C. Pradel, and Z. L. Wang, "Harvesting water drop energy by a sequential contact-electrification and electrostatic-induction process," *Advanced Materials*, vol. 26, no. 27, pp. 4690–4696, 2014.

Appendix A

Electrode structures of the rotator

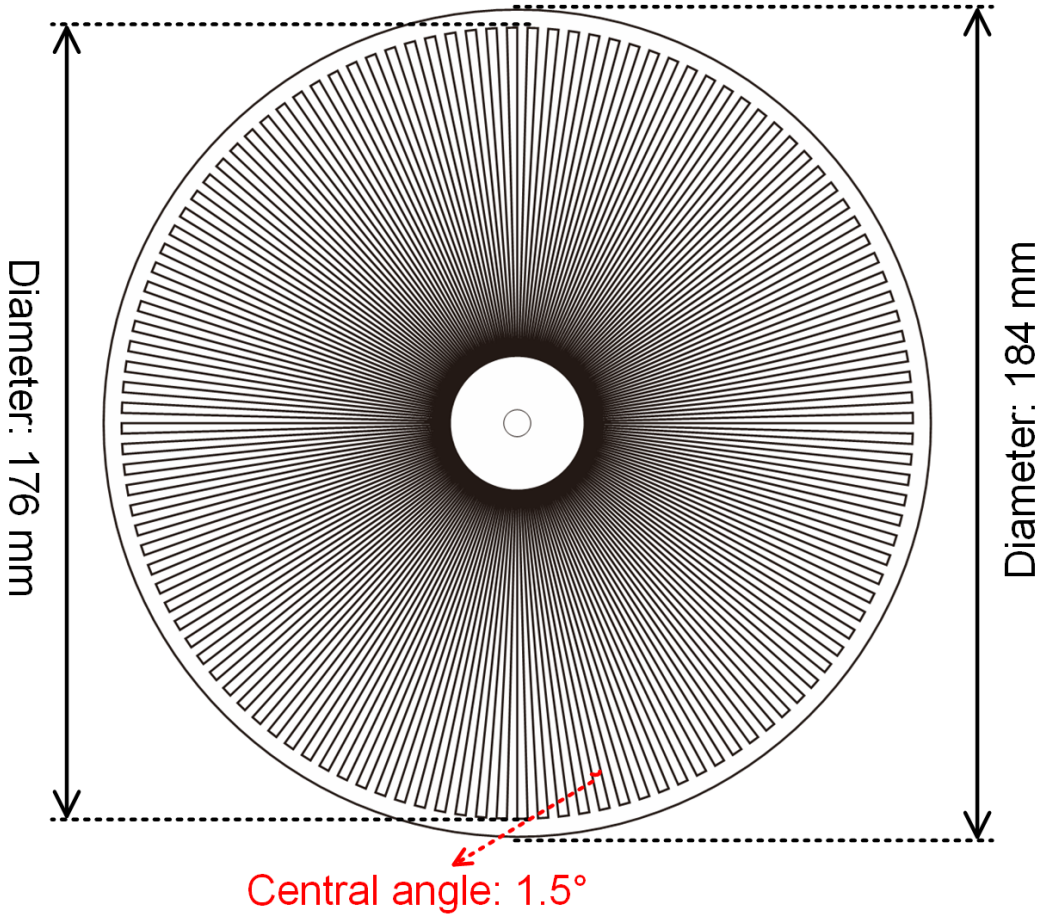

Appendix B

Electrode structures of the stator

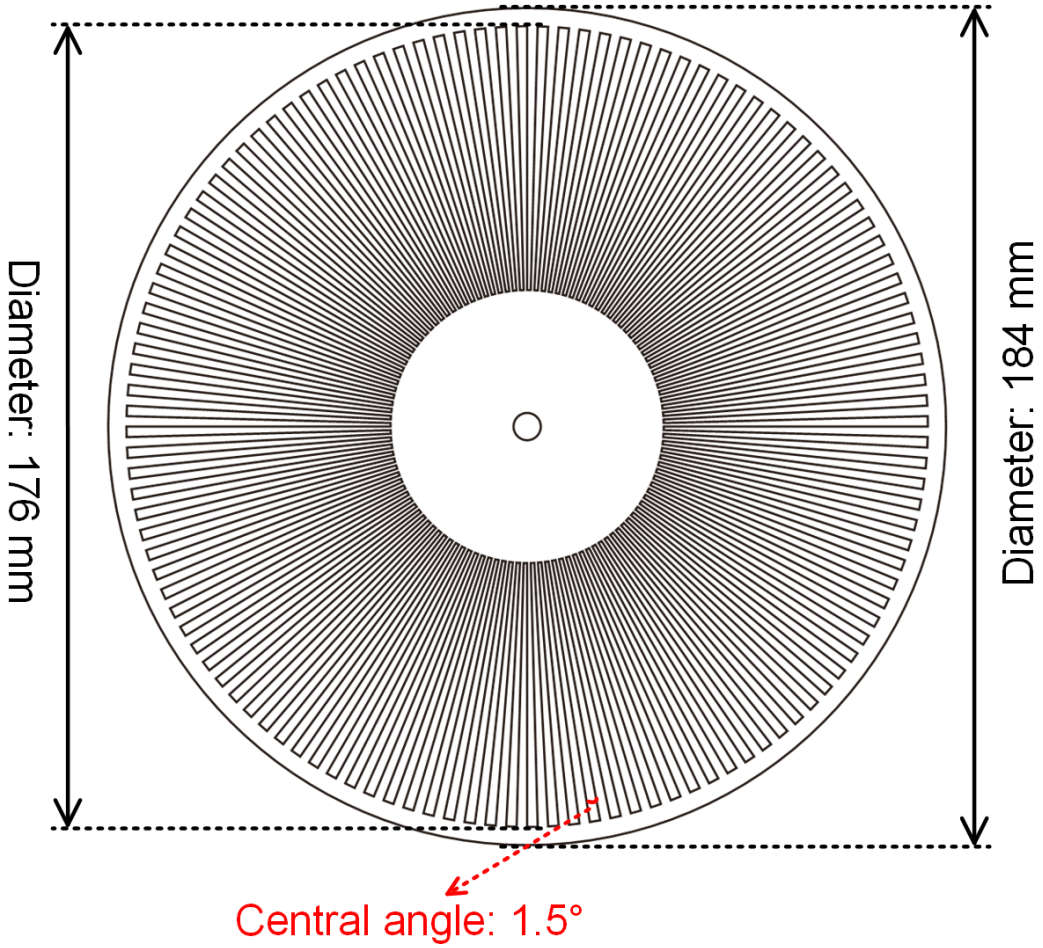

Appendix C

Acoustic properties of tissues/materials

Table C.1: Acoustic properties of tissues/materials.

Tissue/material	Sound speed (m/s)	Density (g/cm^3)	Acoustic Impedance (MRayls)
Water	1480	1	1.48
Vegetable oil	~1500 (measured)	1.070	1.60
Blood	1575	1.055	1.66
Fat	1450	0.95	1.38
Muscle	1575	1.065	1.68
Skin	1730	1.15	1.99

B. Zeqiri, "Reference liquid for ultrasonic attenuation," Ultrasonics, vol. 27, no. 5, pp. 314–315, 1989.
F. A. Duck, Physical properties of tissues: a comprehensive reference book. Academic press, 2013.

Appendix D

Fabrication process of CMUT

The pre-fabricated CMUT is a row-column-structured 2D array. (step 1) Firstly, 500-nm-thick wet thermal silicon oxide was grown on the surface of SOI wafer (2 μm of P-doped 0.001 ohm·cm device layer, 1 μm of boxing layer, 500 μm of handling layer). (step 2) Next, photolithography and RIE process were performed to etch trenches down to the boxing layer, forming row structures. (step 3) Another photolithography and RIE process was done to build cavities on the wet thermal oxide layer (50 μm radius and 250 nm depth). Then, a standard clean process was conducted for the patterned SOI wafer and an unpatterned SOI wafer (2 μm of P-doped 0.001 ohm·cm device layer, 1 μm of boxing layer, 500 μm of handling layer) before fusion bonding. (step 4) Fusion bonding was performed under the pressure of 3 kg/cm^2 and the temperature of 480°C in vacuum, followed by 1100°C annealing. After this step, vacuum cavities of 10^{-3} Pa were formed. (step 5) A combination of RIE and TMAH etching was used to release the handling layer of the top SOI wafer. The boxing layer was then removed by 5:1 BOE solution. (step 6) Photolithography and RIE process were conducted to etch column structures. (step 7) In next step, the bottom electrodes were exposed by another photolithography and RIE process. (step 8) Lastly, an electron-beam deposition, followed by lift-off process, was done to create Ni (5 nm)/Au (150 nm) contact pads for wire-bonding.

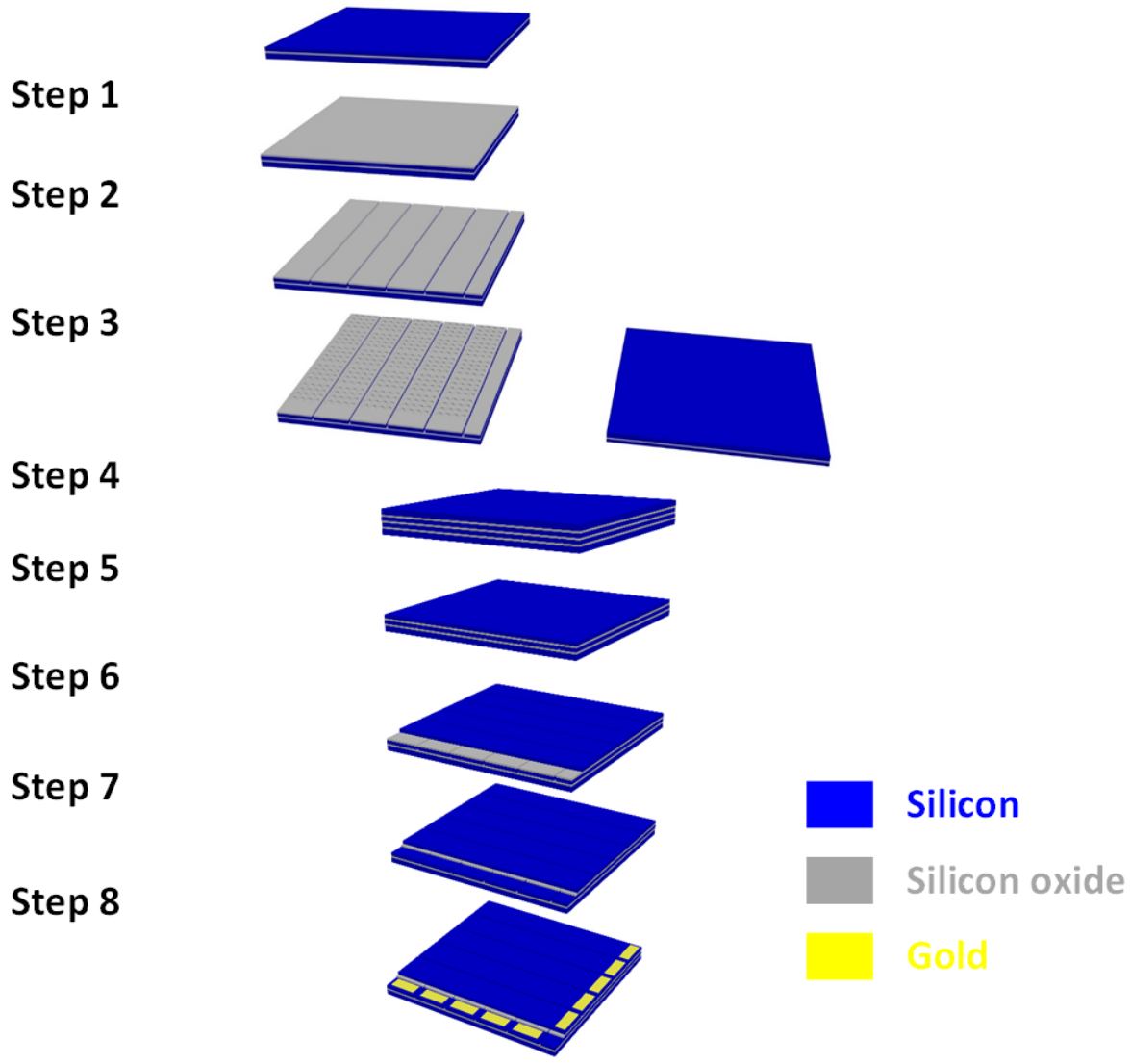

Figure D.1: The fabrication flow of the CMUT.